UNIVERSITY OF OKLAHOMA
GRADUATE COLLEGE

COMPUTATIONAL INVESTIGATIONS OF A SHAPE-MEMORY POLYMER FOAM EMBOLIZATION DEVICE FOR INTRACRANIAL ANEURYSMS

A THESIS
SUBMITTED TO THE GRADUATE FACULTY
in partial fulfillment of the requirements for the
Degree of
MASTER OF SCIENCE

By
RYAN ALEXANDER BODLAK
Norman, Oklahoma
2021

COMPUTATIONAL INVESTIGATIONS OF A SHAPE-MEMORY POLYMER FOAM EMBOLIZATION DEVICE FOR INTRACRANIAL ANEURYSMS

A THESIS APPROVED FOR THE
SCHOOL OF AEROSPACE AND MECHANICAL ENGINEERING

BY THE COMMITTEE CONSISTING OF

Dr. Chung-Hao Lee, Chair
Dr. Kuang-Hua Chang
Dr. Chenkai Dai

ACKNOWLEDGMENTS

First and foremost, I'd like to thank Dr. Chung-Hao Lee for his tireless support throughout my undergraduate and graduate career. He introduced me to two of the most important topics I was exposed to in my higher education, numerical methods and biomechanics, which laid the basis for this thesis. He has devoted countless hours mentoring me and guiding me through my work, and I am grateful to have had him as my advisor.

Dr. Kuang-Hua Chang deserves recognition for his wonderful teaching and modeling advice throughout my schooling, his patience and understanding when I made my decision to switch my thesis work to Dr. Lee's lab, and his willingness to serve on my committee. I'd also like to thank Dr. Chenkai Dai, the other member of my committee, and Dr. Gerald Miller, who was a great help in understanding porous media fluid flow. My gratitude is owed and gladly extended to all the other faculty and staff at the University of Oklahoma who have helped me throughout my academic career.

I'm indebted to all my friends in the BBDL who helped me throughout the process and made my time in the lab fruitful and enjoyable, among them Luke Whitney, Colton Ross, Sergio Pineda-Castillo, Devin Laurence, Rob Kunkel, and others.

And, of course, to my wonderful family: I couldn't have done it without you.

Thank you all.

ABSTRACT

The objective of this research is to determine the efficacy of an intracranial aneurysm treatment option. An open-source computational fluid dynamics software is used to simulate blood flow through 6 patient-specific intracranial aneurysm geometries for 42 different cases. Virtual shape memory polymer foam embolization devices are created and implanted into the geometries. Different porous media parameters are considered for the embolic devices, and it is found that devices with a permeability of $\sim 5\times10^{-9}$ m^2 can reduce aneurysmal inflow by 90% for various geometries of the treated aneurysm and its surrounding parent arterial vessel. For a wide-necked aneurysm, devices with a permeability of $<5\times10^{-8}$ m^2 reduce the average flow velocity within the aneurysm space by >60%, indicating that they may be able to provide that level of performance for most aneurysm morphologies. As such, a permeability range of 5×10^{-9}–5×10^{-8} m^2 is recommended for the device. Furthermore, material removal from the center of the device is found to be feasible for larger aneurysm devices if compressibility is deemed a concern. For a high-inflow case, the average aneurysmal velocity reduction is within 2% of the uncored device for all cored devices with a material thickness of at least 1.5 mm occluding the inlet area. Convective heat transfer is also modeled to determine the safety of the thermally stimulated shape memory polymer device. Steady-state simulations identify the worst-case geometry, a deep aneurysm with little opportunity for convection. Transient heat transfer during the device deployment process for 2 stimulus temperatures is modeled with this aneurysm, demonstrating that the vessel walls can reach the stimulus temperature of 40 °C and 45 °C within seconds and take over a minute to cool back to near body temperature. The threshold for brain tissue damage is not reached, but nonetheless, it is suggested that the temperature and heating time be kept as low as possible. Full model validation is not available, but general verification of the flow fields in untreated aneurysms is achieved by comparing simulation results to those obtained by other research groups in a modeling competition.

KEYWORDS computational fluid dynamics (CFD); endovascular embolization; intracranial aneurysms; medical device design; shape memory polymer foam

CONTENTS

LIST OF FIGURES

LIST OF TABLES

LIST OF SYMBOLS

LIST OF ABBREVIATIONS

3DRA	3D rotational angiography	18
AComA	anterior communicating artery	4
AR	aspect ratio	7
CAD	computer-aided design	17
CEM_{43}	cumulative equivalent minutes at 43 °C	55
CFD	computational fluid dynamics	2
DICOM	Digital Imaging and Communications in Medicine	18
FSI	fluid-structure interaction	59
FVM	finite volume method	20
IA	intracranial aneurysm	1
ICA	internal carotid artery	4
ISAT	International Subarachnoid Aneurysm Trial	9
MAE	mean absolute error	30
MATCH	Multiple Aneurysms AnaTomy CHallenge 2018	18
MCA	middle cerebral artery	4
PComA	posterior communicating artery	4
PDE	partial differential equation	17
PIV	particle image velocimetry	23
RANS	Reynolds-averaged Navier–Stokes	29
SAH	subarachnoid hemorrhage	5
SMP	shape memory polymer	1
SMP*f*	shape memory polymer foam	1
SR	size ratio	7
VFR	volumetric flow rate	21
VRR	velocity reduction ratio	41
WSS	wall shear stress	6

1 INTRODUCTION

1.1 Motivation

An intracranial aneurysm (IA) is a local ballooning of an artery in the brain, often appearing to be a saclike protrusion from a parent vessel. Aneurysms are generally harmless unless they burst; their rupture causes bleeding and stroke. The mechanisms of IA growth and rupture are not fully understood, but hemodynamics, or the mechanics of blood flow, is known to play a crucial role by inducing stresses on the aneurysm wall. Most clinical aneurysm treatments therefore attempt to reduce blood flow into the aneurysm from the parent vessel. Microsurgical clipping, the oldest aneurysm treatment, uses a clamp placed via craniotomy (open-skull surgery) to externally pinch off the aneurysm entrance from the vessel. Meanwhile, endovascular coiling inserts a mass of coiled wire into the aneurysm space from within the parent vessel. The coil is delivered via catheter. Similarly, mesh stents are also used to divert blood flow internally.

A previously proposed treatment option seeks to improve on these devices, which struggle to treat large or complex geometries, using shape memory polymer (SMP) foam to achieve a complete and lasting occlusion of the treated aneurysm. SMPs are a special class of plastics that can hold a deformed geometry for an arbitrary amount of time, free from any external force, and yet return to their original configuration in response to a stimulus. For this reason, they could be a powerful tool for treating aneurysms. A shape memory polymer foam (SMP*f*) produced in a geometry identical to a patient's aneurysm could be deformed to hold a smaller profile while being delivered to the aneurysm via catheter, before being triggered and returning to its original form. Because its geometry would match the aneurysm's, it could theoretically block more flow into the aneurysm space than randomly packed coils, and indeed, *in vivo* experiments have offered promising results.

1.2 Objective and Scope

The objective of this research is thus to evaluate the effectiveness of a shape memory polymer foam embolization device. It consists of 42 simulations comprising the following 3 major studies carried out in OpenFOAM-v2012, an open-source computational fluid dynamics (CFD) software:

1. Steady-state blood flow through untreated saccular aneurysms.
2. Steady-state blood flow through saccular aneurysms treated with shape memory polymer foam.
3. Steady-state and transient heat transfer through blood flowing around the embolization device.

The remainder of this thesis delves into these studies. Chapter 2 gives an overview of the anatomy, pathology, and treatment of aneurysms, before shifting focus to computational techniques for modeling fluid flow. Chapter 3 outlines the process used to digitally recreate patient-specific aneurysm geometries, apply boundary conditions, and simulate flow through the vessels and aneurysm. The simulation results are discussed. In Chapter 4, a similar set of simulations are run, with the addition of an SMP*f* treatment option in the aneurysm space. Recommendations for device design are given. Heat transfer from the device is examined in Chapter 5 to ensure that tissue damage does not occur. Finally, conclusions from the body of thesis are made in Chapter 6.

2 LITERATURE REVIEW

2.1 Anatomical Overview of Intracranial Aneurysms

A cerebral, brain, or intracranial aneurysm (IA) is a local, weakened dilation of a cerebral artery wall that has the potential to rupture under the pressure of blood flow, often causing disability or death. A wide variance in aneurysm shapes and sizes exists. Saccular and fusiform aneurysm morphologies (Fig 2.1) predominate; other, rarer IAs include micro, blister, and giant serpentine aneurysms.

Saccular IAs, also called “berry” aneurysms due to their resemblance to a berry hanging from a stem (Fig 2.1a), consist of a narrow neck region that expands into a well-defined sac, or dome, protruding from the parent artery. They are the most common type of intracranial aneurysm, accounting for upwards of 65% of all IAs.[1] They often develop at

vessel bifurcations where arteries of similar size branch from one another, e.g. at the basilar apex; this subtype is known as a bifurcation aneurysm. Saccular aneurysms located along non-branching vessel sections are called sidewall IAs. Roughly 80–90% of saccular IAs have a diameter of 2–12 mm.[2,3] Those with diameters larger than 25 mm are classified as giant.

Meanwhile, fusiform IAs are dilations of the entire vessel wall and resemble a bulge in a hose. There is no discernible neck region in a fusiform IA. Rather, the vessel's circumference deforms outward. Because far fewer IAs are fusiform than saccular, they are less well-studied. They are also more difficult to treat since restoring a proper vessel canal often blocks flow to perforator arteries within the segment.[4] This research focuses on saccular aneurysms, which are more common and for which clinical treatments are most readily available.

(a) (b)

FIG 2.1 Illustration of the two basic aneurysm morphologies[5]: (a) the saccular aneurysm, and (b) the fusiform aneurysm.

Intracranial aneurysms occur almost entirely within the Circle of Willis, an intricate, ringlike joining area of several arteries at the base of the brain (Fig 2.2). The arteries in the Circle of Willis supply the brain with blood at a typical rate of 770 mL min^{-1} in healthy, young adults; reduction in brain volume with aging sees a corresponding decrease to 660 mL min^{-1} in the healthy elderly.[6] Around two-thirds of this cerebral blood flow is distributed between two primary arteries on each side of the brain: the internal carotid artery (ICA), 36%, and middle cerebral artery (MCA), 27%.[6] These percentages seem to align with the distribution of IAs reported by the International Study of Unruptured Intracranial Aneurysms, which looked at 6621 unruptured saccular aneurysms in 4060 patients to assess their natural history and treatment risks. An IA was present in the ICA for 38% of patients, while 29% suffered one in the MCA. The posterior circulation—which includes the basilar artery, vertebral arteries, and posterior communicating artery (PComA)—and anterior communicating artery (AComA) harbored an aneurysm in 20% and 12% of cases, respectively.[2]

The prevalence of unruptured IAs in a general population of adults is estimated to be 3–5% worldwide,[3,8] suggesting that around 6 million Americans harbor an unruptured IA at

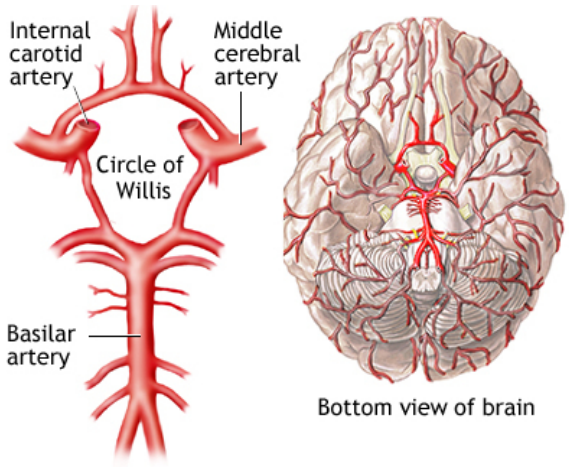

FIG 2.2 Illustration of the Circle of Willis.[7]

any time. In this unburst state, aneurysms occasionally cause visual impairment or cranial nerve palsies, but are largely innocuous and asymptomatic. The danger lies in their growth and eventual rupture (Fig 2.3), which releases blood into the subarachnoid space—the region between the brain and surrounding membranes—in a life-threatening event known as subarachnoid hemorrhage (SAH). As a type of hemorrhagic stroke, SAH has a 24-hour mortality rate of roughly 25%, killing 10–15% of victims before they reach the hospital and another 10% within the first day of hospital stay.[9] Despite medical advances, overall case fatality has only marginally decreased from 50% in the 1960s; more recent estimates place the figure at 33–45%.[10] A quarter of survivors have permanent disabilities.[11] Unfortunately, aneurysm rupture is not uncommon. It is responsible for 85% of non-traumatic SAH and 5–10% of all strokes,[12] affecting around 8 people per 100 000 every year[13] or roughly 26 000 Americans annually.

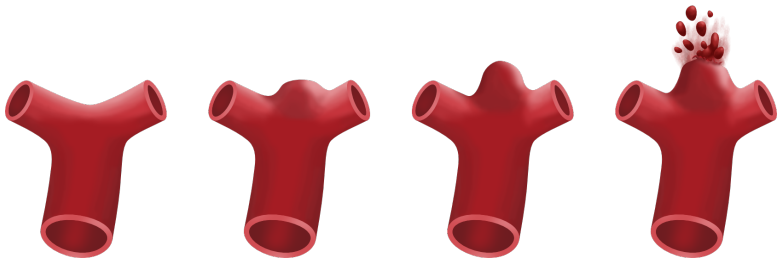

FIG 2.3 Aneurysm growth and rupture.

The formation of intracranial aneurysms is incompletely understood, though it is known that certain people are more susceptible to developing an IA than others. For instance, women are about 60% more likely to harbor an IA than men.[3] IAs are not congenital and rarely form before 30 years of age; children account for fewer than 5% of patients with IAs,[14] and the majority of those cases are caused by trauma or infections.

Genetic and environmental factors both appear to play a role in aneurysm formation. Compared to the general population, people with two parents or siblings diagnosed with IAs are four times more likely to develop their own.[15] Aneurysm formation is seven times more likely in patients with autosomal dominant polycystic kidney disease, a rare genetic disorder.[3] Smoking, arteriosclerosis, and hypertension also increase the risk of aneurysm formation and rupture.[16] Around 20–30% of patients with an unruptured IA have at least one more.[17]

Aneurysms often form at bifurcations, providing a clue that hemodynamics is a primary driver in aneurysm formation and growth. Abnormal blood flow provides mechanical stimuli, namely pressure and shear stress, that trigger remodeling in the vessel wall. This remodeling alters the flow, inciting further remodeling and further changes to the flow.[18] On the structural level, intracranial arteries are thought to be more vulnerable to this process than extracranial arteries due to their lower proportions of elastin (a protein that allows tissues to return to their original state after deformation) and their immersion in cerebrospinal fluid instead of connective tissue.[15] Although a strong collagen band has been found at the apex of cerebral artery bifurcations, the tissue discontinuity at the edge of this band may leave the adjacent wall open to aneurysm formation.[19]

The hemodynamic stimulus believed to impel aneurysm growth is wall shear stress (WSS), which is generated by the tangential frictional force exerted on the vessel wall by flowing blood. However, both low and high values of WSS have been linked to aneurysm development.[18] Meng *et al.* have worked to resolve this apparent contradiction by suggesting that differing hemodynamics can drive two separate pathways. Researchers have observed that local internal elastic lamina loss, bulge formation, media thinning, and a loss of smooth muscle cells result when the WSS and spatial WSS gradient (change in stress over a distance) exceed a limit.[18,20] Fluid acceleration in the regions around bifurcations or curves causes a high WSS environment, leading to the initial formation of the aneurysm sac. After this stage, two things may occur.

The developing bulge's geometry may allow for impinging flow and its associated high WSS to persist in the aneurysm sac. In this case, the degradation that was previously mentioned for aneurysm genesis will continue to occur.[18] On the other hand, the aneurysm may bulge in such a way that the sac is exposed to low WSS, which is known to promote an inflammatory response in the endothelium.[18] This response causes wall degradation via enzymes that digest arterial wall extracellular matrix called matrix metalloproteinases.[21] In turn, smooth muscle cells migrate to a different region of the vessel wall and undergo a change that impairs their ability to synthesize collagen, resulting in aneurysm growth and further wall breakdown.[21] The IAs generated in the first case are hypothesized to be small and thin-walled, while the second are thought to be large, thick-walled, and infil-

trated with inflammatory cells. Both types have been observed clinically,[18] and these flow patterns have been observed in subsequent computational studies.[22]

Whatever the cause of its development, an aneurysm may eventually rupture following a growth period. The annual rupture risk is around 0.95–1.9% for the general class of IAs.[23–25] The likelihood of a particular aneurysm rupturing depends on many factors, including history, location, shape, and size. The rupture rate for actively growing IAs is an order of magnitude higher than for those that are stable.[26] Aneurysms in the AComA and PComA, as well as IAs with irregular wall protrusions known as daughter sacs, have elevated rupture risks.[23] Asymmetries in the Circle of Willis, particularly in the anterior segment, also increase the risk of rupture, likely by altering the hemodynamics in the region[27] (researchers have noted that the flow of blood directly into the aneurysm inlet, rather than along a curved trajectory, is associated with rupture[28]). Even the surrounding tissues, bone in particular, can affect an aneurysm's rupture risk by causing deformation.[29]

A large-scale study of IAs in Japan found that aneurysms smaller than 5 mm have an annual rupture rate of 0.36%, compared to 33.4% for giant aneurysms (larger than 25 mm).[23] Another recent study of over 12 000 ruptured IAs found the mean size to be 7.0 mm.[30] As the study's authors noted, however, there was significant heterogeneity in ruptured IAs sizes that depended on location. Smaller or more distal vessels such as the AComA harbored smaller ruptured aneurysms than those on larger vessels like the ICA,[30] suggesting that the size ratio (SR), defined as the ratio between the maximum aneurysm depth and mean parent artery diameter (see Fig 2.4), is a better predictor than size alone. Indeed, previous studies have shown that ruptured IAs have much larger SRs,[31] with an SR > 3 considered a risk.[15] The aspect ratio (AR), defined as the ratio of the dome's depth to the neck's average width, has also been identified as an important factor in saccular aneurysm rupture, with increased rupture risk for ARs larger than 1.6.[15]

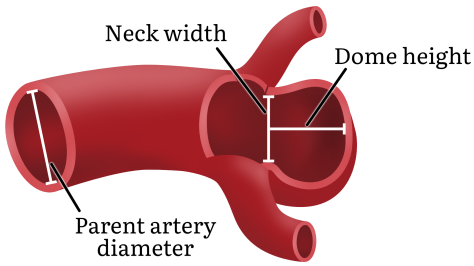

FIG 2.4 Illustration of the dimensional metrics used to describe the typical geometry and anatomy of an IA.

With a basic knowledge of IAs and their dangers established, the discussion now turns to the techniques developed to treat them.

2.2 Clinical Aneurysm Treatments

Because hemodynamic loading on the vessel wall is known to play a significant role[32] in aneurysm growth and rupture, the goal of most clinical treatments for ruptured and unruptured aneurysms is to divert blood flow from the aneurysm back into the artery. This allows a blood clot, or thrombus, to form within the aneurysm body, reducing the risk of rupture and/or recurrence. Treatments can be categorized as surgical (exterior to the vasculature) or endovascular (within the vessel lumen). The number of aneurysms being treated has risen steadily in recent years, probably because the wider adoption of medical imaging has led to more frequent incidental identification of IAs before rupture.[33] A brief overview of selected treatment options is given here.

2.2.1 Microsurgical Clipping

In 1937, Dandy performed what could be described as the first modern aneurysm surgery when he placed a silver clamp around the neck of an aneurysm harbored in a patient's right internal carotid artery to isolate the aneurysm from the vessel.[34] The device Dandy used was first described 26 years earlier, in 1911, by Cushing, who developed the device for instances when a ligature could not be used to encircle the vessel upstream of the aneurysm, the previous treatment method for IAs. As it would turn out, this new technique, which was the first to focus on occluding the aneurysm itself and not the vessel, was far more effective. In fact, it is still widely used today, albeit with refined clip designs.

The treatment, called surgical clip ligation or microsurgical clipping, works by externally sealing off the neck of a saccular aneurysm with a mechanical clamping device placed via craniotomy (open-skull surgery). If properly situated, the clip keeps blood from flowing into the IA (Fig 2.5), eliminating the rupture risk or providing a life-saving intervention if the IA has already ruptured.

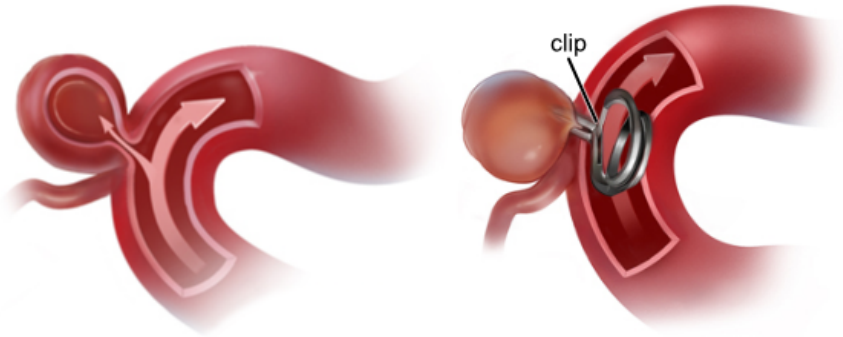

FIG 2.5 Illustration of microsurgical clipping used for treating IAs by completing blocking any inflow.[35]

The International Subarachnoid Aneurysm Trial (ISAT), an influential, large-scale, randomized study published in 2002, found clipping to have a 69.4% success rate. That is, 550 of the patients who received clipping treatment for a ruptured IA had no or minor lifestyle restrictions after one year, while 10.1% (80) were dead.[36] Although these numbers are discouraging, it is important to remember that SAH kills around 25% of victims within the first day,[9] so the one-year death rate after clipping is somewhat remarkable. Thankfully, clipping outcomes are even better when applied to unruptured aneurysms. Wiebers *et al.* found an 87.4% success rate after one year for 1591 open surgeries. Only 3.0% of patients had died.[2]

Clipping offers a high complete occlusion rate; one neurosurgical practice achieved aneurysm obliteration in 98.3% (620) of the MCA aneurysms treated there over 13 years.[37] Unfortunately, it is also invasive and requires a distinct aneurysm neck to work.

2.2.2 Endovascular Coil Embolization

Numerous treatment advances were made throughout the mid-twentieth century, including improved clip designs, the integration of microscopes into surgery (microsurgery), and early forays into endovascular treatments. In 1964, Lussenhop and Velasquez performed the first ICA catheterization. Ten years later, Serbinenko occluded three IAs using detachable, balloon-tipped catheters.[38] Nonetheless, these treatments were dangerous, and clipping remained the dominant option until the introduction of the Guglielmi detachable coil in 1991,[39] which improved on previous stiff, non-retrievable coil designs. The Guglielmi detachable coil is a soft platinum wire that gently conforms to the aneurysm's shape while being implanted via catheter.[39] The packed coil remains in the aneurysm, diverting blood flow from the sac and inducing thrombosis within it (Fig 2.6).

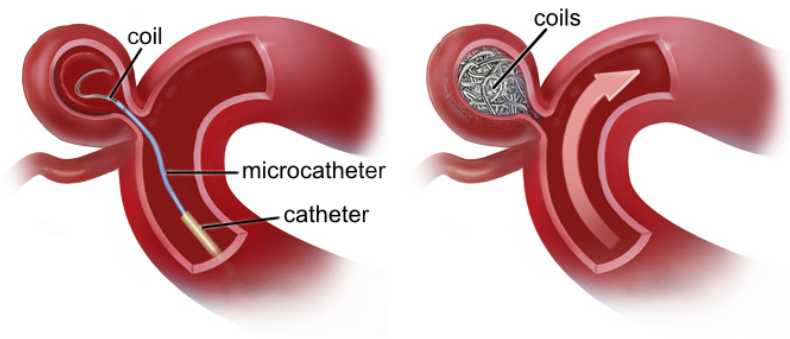

FIG 2.6 Illustration of IA treatment by means of endovascular coil embolization.[40]

Endovascular coil embolization is less invasive than surgical clipping. First, an incision is made on the patient's inner thigh, providing access to the femoral artery. A catheter is

then inserted into the incision and guided through the vasculature to the affected vessel in the brain. Fluoroscopy enables real-time visualization of the process by introducing radiopaque dye into the vessel, making the catheter's location visible to X-rays. A guidewire in the catheter allows the surgeon to fine-tune the coil's positioning at the aneurysm inlet before electrically releasing the coil. Occlusion occurs when the coils have forced most of the dye from the aneurysm and occupy most of its volume.[39] A coil packing density of 20–25% is required for good outcomes, though this may be insufficient for large IA, which can have high absolute residual volumes, leading to coil compaction and less clotting.[41] Stent-assisted coiling (placing a stent over the aneurysm inlet to trap the coils) can improve results for many cases, including large or wide-necked IAs.[42]

Endovascular coiling revolutionized the care of intracranial aneurysms. The technique's use grew rapidly during the 2000s, and coiling is now used to treat around one-third of all IAs.[33] That percentage is higher for some patient subgroups. One neurosurgical practice reported that the percentage of basilar artery bifurcation aneurysms treated endovascularly by their surgeons rose from 22% in 1998 to 88% in 2009 (with similar numbers of total aneurysms treated), and from 6% to 38% for AComA IAs.[33]

Some of this increase can be traced back to the ISAT, which demonstrated successful outcomes in 76.3% of endovascular coiling cases, compared to 69.4% for clipping.[36] According to Wiebers *et al.*, the difference was more modest for unruptured aneurysms (89.8% versus 87.6%).[2] A recent large-scale retroactive study examining 4899 unruptured IA patients found in-hospital mortality to be similar between clipping and coiling (0.7% versus 0.5%), but coiling resulted in fewer hemorrhagic complications and a much lower rate of discharge to long-term care (17% against 3.7%).[43]

On the other hand, clipping appears to be superior in some instances. A recent meta-analysis on treatment options for unruptured MCA IAs found that postoperative surgical complications occurred in 2.4% (13 of 537) of clipping cases, compared to 9.8% (12 of 123) of coiling cases.[44] Complete occlusion was achieved more often with clipping, and retreatment and rebleed rates were lower.[44] Clipping is also recommended for young patients with small, anterior circulation IAs, since clipping is an order of magnitude more durable than coiling and the risk of intraprocedural complications is similar between the two treatment options.[45]

Endovascular coiling, while a remarkable advancement to the field, is not a perfect treatment option. Coiling has been known to fail due to coil migration, coil compaction, and incomplete aneurysm filling, particularly for larger aneurysms.[46] It is estimated that recurrence occurs in one-third of aneurysms following coil embolization and is almost twice as likely for aneurysms larger than 10 mm in diameter.[47] Recurrence also appears to vary with the particular type of coil used; for instance, one study found that retreatment

was necessary for 9 of the 41 aneurysms treated with a polymer-coated coil, compared to 4 of 33 for bare platinum coils.[48] For these reasons, other treatments have been developed.

2.2.3 Flow Diversion

Flow diverters constitute another class of endovascular treatments. They were introduced in 2006.[38] The Pipeline Embolization Device (eV3, Irvine, CA), one popular flow diverter, is a woven wire mesh tube made from platinum and a cobalt–nickel alloy with 0.02–0.05 mm^2 pores that provides 30–35% vessel coverage.[38] The stent is placed within the parent artery and extends across the aneurysm inlet, reducing aneurysm inflow through its tightly packed pores and aiding in vessel wall reconstruction (Fig 2.7). The high metal-on-vessel contact area necessitates the use of thrombus-inhibiting antiplatelets to avoid thromboembolism, wherein a blood clot forms and plugs the vessel rather than the aneurysm. Intraprocedural complication rates and postprocedural thromboembolism rates seem to be similar between stent-assisted coiling and flow diversion, at roughly 4%.[49] Large meta-analyses have reported a 6-month complete occlusion rate of 76–78%,[26,50] with around a 75% success rate for large and giant aneurysms.[51] Flow diversion also results in better sight outcomes for patients with visual impairments due to paraclinoid aneurysms than other methods.[52] Overall, diverters are a promising new treatment option.

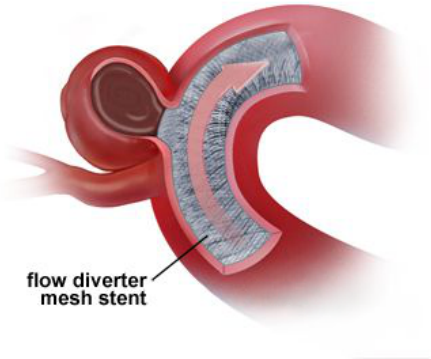

FIG 2.7 Illustration of flow diversion with a mesh stent.[53]

2.2.4 Shape Memory Polymer Embolization

To address the shortcomings of other treatments, endovascular shape memory polymer (SMP) embolization devices were proposed in 2002.[54] These devices use smart materials to occlude the aneurysm space by leveraging the shape memory effect, in which the device receives a triggering external stimulus and recovers its original form after an indefinite period of deformation. Like endovascular coiling devices and flow diverters, they are delivered via catheter.

Chemically, SMPs are copolymers consisting of hard and soft segments composed of two or more crosslinked monomers or polymers. The hard segment determines the original "frozen" state of the SMP, while the soft segment is responsible for its reversible properties. Shape memory polymers can be either thermosets or thermoplastics, and varying SMP classes can respond to different external stimuli, including pH, chemicals, light, and temperature.[55]

For concreteness, the shape memory effect is described here for a thermally induced SMP like the one detailed in this study, though the process remains essentially the same for all types. First, the polymer is produced in the desired primary configuration (the fixed shape to which it will return upon being stimulated), which can often be accomplished using simple molds. In this form, the polymer is crystallized, glassy, and crosslinked. The polymer is then heated past the transition temperature, which is either a glass transition or melting point of the hard component. At this point, the polymer becomes soft and pliable. An external force is applied to the polymer to deform it into a secondary configuration. With the force still applied, the polymer is allowed to cool below the transition temperature. It is now locked into the secondary configuration and will remain in this shape until the stimulus is applied again. To recover the original shape, the polymer's temperature is raised above the transition temperature. Free from external forces, it returns to its primary configuration, completing the cycle (Fig 2.8).

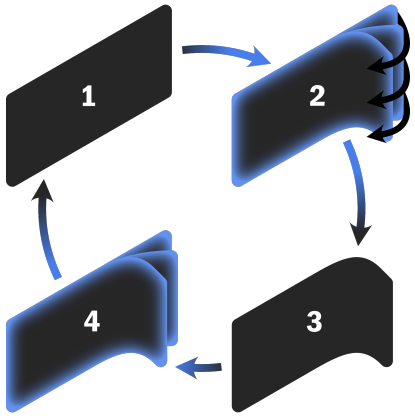

FIG 2.8 Shape memory cycle for thermal SMP. (1) Home configuration. (2) Heated past transition temperature and deformed under load. (3) Cooled below transition temperature, holding deformed configuration indefinitely. (4) Heated past transition temperature, triggering return to home configuration (1).

Because an the shape memory property and transition temperature of an SMP material are inherent to its chemical composition and not its macroscopic structure, i.e. they are shape-independent, shape memory polymer foam (SMP*f*) can often be produced with the same abilities as its solid counterpart. This dramatically broadens the capabilities of SMP devices. Rather than simply bending into a new shape, they can be locked into

a compressed configuration that reduces their cross-sectional area. One particular heat-triggered, open-cell, biocompatible polyurethane SMP*f*, variations of which have been widely reproduced for aneurysm embolization research,[56–58] has a maximum volume compression of up to 70 times.[59] For aneurysm devices, this facilitates endovascular deployment and treatment fit, as demonstrated in Fig 2.9. An SMP*f* device can be tailored to a patient's specific aneurysm geometry, delivered to the site with a microcatheter, and released from its compressed configuration upon stimulation. The device will then expand into the aneurysm space and fully, precisely occlude it. Unlike coils, the device can be made to even reconstruct the vessel shape at a bifurcation, allowing for complete healing at the ostium (the surface that defines the base of the aneurysm neck).

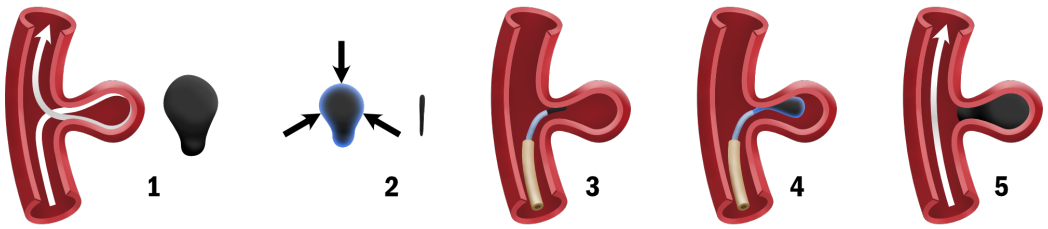

FIG 2.9 SMP*f* embolization device deployment process. (1) Geometry. (2) Triggered, compressed, and released from stimulus to hold compressed configuration. (3) Delivered to site via microcatheter. (4) Retriggered, causing expansion to original form. (5) Aneurysm occlusion.

Experiments suggest that aneurysms treated with such SMP*f* devices may have improved outcomes versus those treated with other methods. Boyle *et al.* established the viability of a hybrid device composed of polyurethane SMP–coated nitinol coils, achieving an occluded volume exceeding that of bare metal coils and HydroCoils (platinum coils coated in a hydrogel that expands in water).[60] Horn *et al.* implanted a hybrid device (Fig 2.10), composed of a low-density SMP*f* core surrounded by a high-density SMP*f* ring, into *in vivo* porcine sidewall aneurysm models in the animals' carotid arteries, and monitored them for 180 days. The foam-treated aneurysms saw a cross-sectional area reduction of 89–93% over the period, compared to 18–34% for the aneurysms treated with bare coils.[57] Rodriguez *et al.*'s similar study demonstrated complete aneurysm endothelialization after 90 days and a minimal inflammatory response (Fig 2.11).[56] Moreover, an extensive experimental, simulation, and analytical study by Hwang *et al.* suggests that these devices can safely be oversized without approaching the aneurysm wall breaking stresses,[61] allowing them to even better fill the IA cavity.

The development of these devices is ongoing, and various questions regarding their optimal design remain. For example, how porous should the foam be? Is using different foam densities in separate regions of the device, like Horn *et al.*'s approach, beneficial? Is the use of a thermal stimulus acceptable? This research seeks to offer some direction, focusing on the effects a thermally triggered SMP*f* device has on the velocity, pressure, and

temperature fields within the aneurysm. These effects are examined using computational fluid dynamics (CFD), which can be a powerful tool for studying hemodynamics and assessing patient-specific rupture risk for IAs, when used correctly. A working knowledge of continuum mechanics, the physics underpinning CFD, is therefore required.

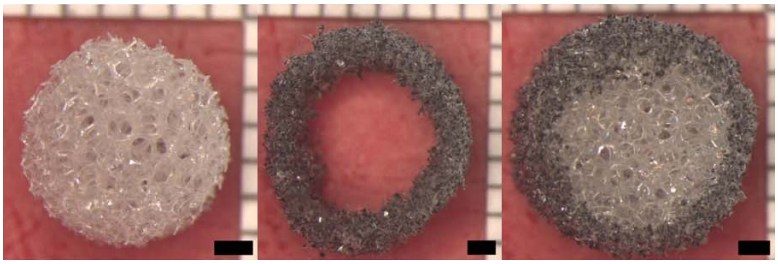

FIG 2.10 Hybrid SMP*f* device developed by Horn *et al.* that is composed of two foam types, a low-density inner core and a high-density outer ring. Scale bars = 1 mm.[57]

FIG 2.11 *In vivo* porcine healing response to an SMP*f* device developed by Rodriguez *et al.* Images taken at 0, 30, and 90 days after implantation. Note intact surface at 90 days, with no exposed polymer.[56]

2.3 Continuum Fluid Mechanics Framework

The simulation-based studies performed in this thesis draw on the theoretical framework of continuum mechanics—more specifically, fluid mechanics (in this case, hemodynamics), poroelasticity, and thermodynamics—to describe describe fluid flow and heat transfer within an intracranial aneurysm. Hemodynamics, a branch in the broader field of fluid mechanics, seeks to understand blood flow through the body. Like other fluid dynamics disciplines, it must consider the fluid properties, flow regime, and control volume through which the blood is flowing to characterize the blood's velocity and pressure. An understanding of fluid flow through porous media is also required for this research, since the SMP device being considered is composed of a highly porous open-cell foam. Lastly, fluid mechanics can be coupled with thermodynamics to describe heat transfer from the thermally triggered SMP*f* device to the blood and vessels. The equations representing these phenomena are incorporated into computational models to find approximate their solutions.

2.3.1 Fluid Flow Principles

The Navier–Stokes equations form the foundation of modern fluid mechanics theory. Formulated in the nineteenth century, they were introduced as a generalization of Euler's inviscid fluid equations by Navier and were later improved by Stokes. The equations describe the motion of viscous fluids, representing the conservation of momentum for the fluid. For an incompressible, Newtonian fluid, they reduce from a more generalized set of momentum conservation equations to

$$\underbrace{\frac{\partial \mathbf{u}}{\partial t} + \mathbf{u} \cdot \nabla \mathbf{u}}_{(1)} = \underbrace{-\frac{1}{\rho}\nabla p}_{(2)} + \underbrace{\nu \nabla^2 \mathbf{u}}_{(3)} + \underbrace{\mathbf{g}}_{(4)} \tag{2.1}$$

where $\mathbf{u}$ is the fluid velocity vector field, t is time, ∇ is the gradient operator, ∇^2 is the Laplace operator, ν is the fluid's kinematic viscosity, p is the fluid pressure field, ρ is the fluid density, and $\mathbf{g}$ represents the body forces (gravitational, electrostatic, etc.) per unit mass acting on the fluid. The different terms correspond to the acceleration field (1), pressure forces (2), viscous forces (3), and external, or body, forces (4). Each numbered term has the units of acceleration ($\mathrm{m\,s^{-2}}$).

The Navier–Stokes equations are always solved in conjunction with the continuity equation, which represents the conservation of mass for the fluid.

$$\nabla \cdot \mathbf{u} = 0 \tag{2.2}$$

Here, $\nabla\cdot$ is the divergence operator.

The above system of equations is incomplete without prescribing boundary and initial conditions particular to the problem. Hemodynamics simulations are performed over a selected section of the blood vessel that contains the region of interest and is enclosed by at least one inlet, outlet, and vessel wall. The boundary conditions are prescribed according to available data or the first principles of fluid mechanics. A velocity waveform is typically prescribed at the inlet(s); flow rate data can be gathered using various imaging techniques. A pressure or flux is specified at the outlet(s). Lastly, the no-slip condition is applied along the vessel wall for physical validity. Initial conditions specify the velocity field (which must satisfy the continuity equation) and pressure field at the time point when the simulation is begun.

2.3.2 Fluid Flow through a Porous Medium

Macroscopic descriptions of slow porous flow behavior depend on two primary material characteristics, porosity and permeability. The porosity ϕ (%) measures the amount of

empty space in a body and is the ratio of the volume of empty space created by the pores, V_{void}, to the body's total, or bulk, volume (V_{bulk}):

$$\phi = \frac{V_{\text{void}}}{V_{\text{bulk}}} \tag{2.3}$$

Permeability is a measure of a porous medium's ability to allow fluid flow. It is related to the material's porosity and the interconnectedness and shape of its pores; materials such as clay are porous but impermeable due to small pore throats (the open regions connecting adjacent pores). The ability to allow flow is intrinsic to a material's solid skeleton and microstructure, so it is often called absolute or intrinsic permeability to avoid confusion with relative permeability, a metric pertinent in multiphase flow. (Throughout this thesis, the permeability being discussed is always intrinsic permeability.) Intuitively, a fluid may flow more easily through a material in one direction than another, so permeability can be characterized as isotropic or anisotropic. It is denoted as k in the isotropic case and as a 3×3 tensor when anisotropic. Permeability has units of area (m^2).

For slower flows, the most basic equation describing fluid flow through a porous medium is Darcy's law, derived in the nineteenth century by Darcy from his experimental observations of water flowing through sand. It depends only on porosity and permeability and is properly written in 1D differential form[62] as

$$-\frac{\partial p}{\partial x} = -\frac{\mu}{k} q \tag{2.4}$$

where $\partial p/\partial x$, also written as ∇p, is the pressure gradient across the sample (Pa m^{-1}) and q is the flux or Darcy velocity with units $(\text{m}^3\,\text{s}^{-1})\,\text{m}^{-2}$. It can also be thought of as a volume-averaged velocity field, accounting for the fact that fluid flows only through the pores.

Darcy's law is well suited to describing groundwater flow through aquifers but is of little value for many other applications, able only to describe creeping laminar flow dominated by viscous drag forces. Forchheimer recognized this and proposed adding a quadratic term to predict the behavior for higher-velocity flows, when inertial effects become significant:

$$-\frac{\partial p}{\partial x} = \frac{\mu}{k} q + \rho C q^2 \tag{2.5}$$

The parameter C in the extra Forchheimer term on the right-hand side of the equation has a unit of m^{-1} and is sometimes called the form factor. It is proportional to the projected cross-sectional area of the matrix perpendicular to the flow,[63] so like permeability, it can be either isotropic or anisotropic.

2.3.3 Heat Transfer in Fluid Flow

The transfer of particles, energy, or other physical quantities within a moving fluid is governed by a pair of processes known as advection and diffusion. Advection results from the bulk movement of the fluid carrying the relevant quantity with it, while diffusion is the tendency for physical quantities to move from a region of high concentration to one of low concentration in an otherwise stationary fluid. A mathematical model capturing the behavior of these two phenomena is known as an advection–diffusion equation; one such equation, the energy equation, models heat transfer. It is solved in conjunction with the momentum and mass conservation equations and, for an incompressible fluid, is given by

$$\frac{\partial T}{\partial t} = \underbrace{-\mathbf{u}\cdot(\nabla T)}_{(1)} + \underbrace{\alpha\nabla^2 T}_{(2)} + \underbrace{s}_{(3)} \tag{2.6}$$

where T is the temperature, α is a measure of the rate at which heat can be transferred within the fluid called the thermal diffusivity, and s is a heat source or sink (often absent). The equation contains terms describing diffusion (1), convection/advection (2), and the entrance or exit of heat from the fluid (3). The boundary and initial conditions required to close the system are prescribed temperatures and/or heat fluxes.

2.4 Computational Aneurysm Modeling Techniques

The governing partial differential equations (PDEs) given above cannot be solved analytically and so must be approximated numerically using computational fluid dynamics (CFD). One of the earliest applications of CFD to aneurysm research was demonstrated in Gonzalez *et al.*'s 1992 paper,[64] which utilized pulsatile flow and a non-Newtonian fluid model to simulate blood flow through an aneurysm in the MCA. By 2004, only 11 more articles had been written on the topic, but research has rapidly increased with growing access to computing power. Around 200 articles on the subject were available by 2012,[65] and hundreds more have been written since. A 2020 study[66] found 795 published papers on IA hemodynamics that used CFD as the primary research technique. The researchers all followed a similar set of steps to obtain their results, the same set of steps necessary to run any CFD analysis:

1. Producing a digital aneurysm geometry, either by performing image segmentation on patient-specific image data or by creating an idealized model in computer-aided design (CAD) software.

2. Discretizing the geometry into a mesh; numerical solution schemes require the continuous governing functions to be transformed into a finite system of algebraic equations solved at discrete points.

3. Choosing appropriate simulation parameters, such as time dependency, blood properties, and boundary conditions.

4. Running the simulations.

5. Interpreting the results.

6. Validating the results (if possible).

Each of these procedures must be performed thoughtfully to increase the likelihood of valid results.

2.4.1 Data Collection & Image Segmentation

The first stage in creating an accurate model begins well before the simulation is run. For patient-specific geometries, the model can only be as good as the data driving it, so proper angiography imaging methods must be used to create an accurate 3D representation. Angiography involves introducing a radiopaque contrast agent into the blood via catheter and then imaging it with an X-ray–based technique such as fluoroscopy to visualize the vasculature (more specifically, the vessel lumen). This produces an image or series of images known as an angiogram. The current gold standard in angiography is 3D rotational angiography (3DRA), which offers better spatial resolution than other imaging techniques.[67] Like computed tomography, 3DRA acquires 3D volumes that can be used in digital reconstructions. These 3D angiograms are composed of three sets, or stacks, of images; each stack contains images that are spaced evenly through the thickness of the vasculature and are mutually perpendicular to images in the other two stacks.

A digital reconstruction can be poor regardless of image quality if the data is processed incorrectly. For most Digital Imaging and Communications in Medicine (DICOM) data including angiograms, image segmentation is the main data processing step. It can be performed manually or automatically and consists of separating a digital image dataset into multiple regions by labeling each pixel. For a 3D angiogram, this means assigning one label to each voxel (a volumetric pixel, visualized as a cube instead of a square) within the vessel lumen and another label to all others.

The 2015 International Aneurysm CFD Challenge[68] and Multiple Aneurysms AnaTomy CHallenge 2018 (MATCH)[69–72] were designed, in part, to quantify the impact of image segmentation variability on the CFD results produced by different research groups. The challenges' curators provided each team with the same DICOM datasets and asked them to seg-

ment the images before simulating flow through the resultant reconstruction using whatever parameters they felt appropriate. The results from each step were then compared.

Twenty-six groups participated in MATCH. While their reconstructions were qualitatively similar, the segmented IA volumes differed by up to 20%, surface quality varied, and the 3D surfaces, particularly the aneurysm necks, tended to overrepresent the actual geometry when compared to the highly resolved 2D reference image.[69] In some cases, moreover, the teams' differing treatment of the vessel branches redefined the aneurysm neck region; one group removed a side vessel included by another, for example (Fig 2.12). Best practice is to compare the 3D surfaces to the corresponding 2D references image to determine if the geometry is being accurately represented.[67]

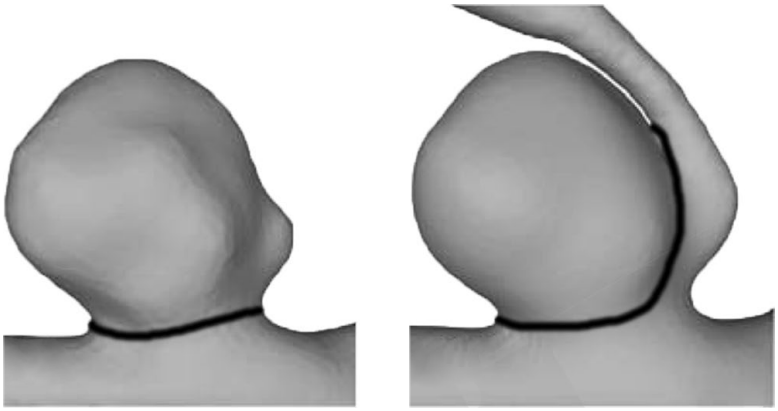

FIG 2.12 Differing aneurysm definitions due to the exclusion of branching vessels during image segmentation. The same aneurysm is modeled as a sidewall aneurysm (left) and a bifurcation aneurysm (right).[72]

Vessel truncation is another important consideration. Necessarily, any inlet or outlet selection is artificial, and studies have demonstrated that clipping the upstream parent artery too close to the IA results in calculated WSS errors and visual differences in flow parameters.[68,73,74] The 2015 International Aneurysm CFD Challenge found that two-thirds of the 26 teams undertruncated the vessel along the MCA; tellingly, all five "highly experienced" groups (having simulated more than 100 IAs) clipped it farther upstream along the ICA.[68] An inlet length of at least 10 artery diameters has been suggested to allow the vessel's tortuosity to establish a realistic flow profile,[73] though Hua *et al.* found that an inlet length of 20 times the inlet diameter was necessary for truncation independence.[75] The same group reported less dependence on the outlet length, with an outlet a mere two times the diameter giving similar flows.

Lastly, in addition to accurate geometries, realistic blood flow rates are vital for proper modeling. Patient-specific flow waveforms can be gathered reliably using phase-contrast magnetic resonance imaging or Doppler ultrasonography,[67] but this data is rarely collected, so values from literature are used instead (see Section 2.4.3).

2.4.2 Spatial Discretization

Once the geometry has been reconstructed *in silico*, the model must be discretized for numerical analysis. The finite volume method (FVM), finite element method, and finite difference method are the three classical discretization techniques implemented in CFD programs, with the former two being the most common. Each method decomposes the geometry into a finite set of spatial points or regions at which the PDEs are solved for a series of points in time. FVM is the formulation employed by OpenFOAM, the CFD software used in this research.

Intuitively, a highly discretized model will more accurately depict the true flow field than a model with a coarser mesh, since smaller flow features can be captured. In fact, as the cell size is decreased for a particular problem, the CFD results will begin to asymptotically converge to a single solution. This is known as mesh independence, and it is crucial for valid results. The threshold cell side length needed to achieve mesh independence within the dome has been identified as around 0.08 mm by various studies.[76–78] Meanwhile, Valen-Sendstad *et al.* suggest that convergence (especially for maximum WSS) is difficult to justify for meshes around even a million cells throughout the fluid domain.[79] Notably, the average cell size used in the MATCH study was 0.17 mm, and some meshes had only $5{\times}10^5$ cells.[71]

2.4.3 Physiological Simulation Parameters

The material properties and boundary conditions of the model are next considered, and certain parameters are widely agreed upon by the research community. The no-slip condition is imposed along the vessel wall as is standard practice for fluid dynamics modeling in the subsonic regime. A blood density of $1.06\,\mathrm{g\,cm^{-3}}$ is easily measured and universally used. The vast majority of current studies also assume rigid walls since vessel wall data is rarely available.[67] Real arterial walls are compliant, allowing them to accommodate more blood per cardiac cycle and smoothing the pulsatile waveform of the blood ejected from the heart. Incorporating this elasticity into simulations would be desirable, but such simulations are no more meaningful unless precise vessel wall information is available.[67] However, it should also be noted that aneurysm walls are relatively indistensible compared to intracranial arteries,[80] so the rigid-wall assumption for the aneurysms themselves is reasonable.[81] Debates have arisen over practically every modeling parameter besides those just listed, including the time dependency, rheological properties, and inlet and outlet conditions.

Valen-Sendstad *et al.* have suggested that tens of thousands of time steps per cardiac cycle may be needed to resolve the most complex IA flow patterns for pulsatile flow,[79] leading to simulation times of days or even weeks. In light of this computational expense,

many groups use steady-state simulations (69% percent of the 795 papers included in Saqr *et al.*'s review did so). Depending on the target diagnostic, this may be reasonable. Geers *et al.* found that WSS values produced by steady-state simulations with time-averaged flow rates reasonably approximated the time-averaged WSS values for the corresponding pulsatile case, to within 5%. However, steady simulations with systolic flow rates consistently overestimated the aneurysmal flow rate and WSS versus pulsatile simulations, while those with diastolic flow rates underestimated them.[82]

Around 90% of researchers use a Newtonian viscosity of 3.5×10^{-3}–4.0×10^{-3} Pa s to describe the blood in their models.[66] In reality, blood is a non-Newtonian fluid that exhibits shear-thinning behavior due to red blood cell aggregation at low shear rates.[83] However, many groups rely on the assumption that blood behaves like a Newtonian fluid in the cerebrovasculature since shear rates are "high enough" to justify using a Newtonian model (though tracing that assumption has proven difficult[66]) because it is less computationally intensive. Numerous studies have been performed to determine the assumption's effect with inconclusive results. Some groups have found that Newtonian models tend to overestimate WSS,[83,84] producing inaccurate rupture estimates, while others argue that the effects are negligible when compared to other modeling parameters and do not appreciably alter flow patterns.[85,86] Berg *et al.* and Saqr *et al.* come to different conclusions in their recent review papers on the state of CFD modeling for IAs,[66,67] with the former suggesting that a Newtonian model is sufficient and the latter suggesting it may not be.

Whatever the other considerations, it is clear that the velocity and pressure boundary conditions largely determine flow patterns. If the inlet velocity is unphysiologically slow, the model will likewise be certainly incorrect. Typically, velocity or volumetric flow rate (VFR) is prescribed at the inlet and pressure is prescribed at the outlet. Patient-specific flow rates are rarely available, so generalized waveforms for the appropriate age group, calculated by averaging the waveforms of many participants in a study, are typically taken from literature and set as the CFD inlet conditions.[67] These averaged volumetric flow rates are often assumed to scale according to a power law based on the artery's cross-sectional area A (and therefore diameter d) and are given by[87]

$$Q_{\text{in}} = Q_{\text{coh}} \frac{d_{\text{in}}^n}{d_{\text{coh}}^n} \tag{2.7}$$

where Q_{in} is the desired inlet VFR for the patient-specific geometry, Q_{coh} is the average inlet VFR from the cohort, d_{in} is the patient-specific vessel diameter at the inlet, d_{coh} is the average inlet vessel diameter of the cohort, and n is a power chosen based on physiological properties. Square ($n = 2$) or cube laws ($n = 3$) are often used. Research has suggested that a square law is most physiologically accurate for at least the ICA.[87] Although this scaling formulation assumes circular vessel cross-sections, which is not strictly cor-

rect, the difference between using anatomical and idealized cross-sections is minor.[88] A much greater source of error is the scaling idealization itself. A comparison of flow rates derived from the power law for patient-specific geometries to the measured flow rates for those same patients revealed individual deviations of up to 120%—though the square law, while exhibiting large maximum errors for individual cases, had the smallest errors and no consistent bias, unlike the flow rates calculated with $n = 0$ and $n = 3$.[89]

Different velocity profiles can produce the same instantaneous VFR across an inlet, so yet another inflow choice must be made. Plug (uniform), parabolic (fully developed), and Womersley (pulsatile) profiles, in order of increasing complexity, are the most common. Plug flow assumes no boundary layer—the velocity is the same over the entire cross-section. A parabolic profile supposes that the flow within the vessel is laminar and fully developed. Lastly, a Womersley profile models pulsatile flow driven by an oscillatory pressure gradient, and the complex shape of the profile at any time is found using a Fourier decomposition. All three are used; for example, 59% of the MATCH teams used plug flow, compared to 12% for parabolic and 24% for Womersley.[71] Various groups have suggested that, provided "long enough" inlet domains, the inflow choice has little effect on hemodynamic factors[75,78,90,91] and that other considerations such as vessel reconstruction and choice of velocity waveform are more important.[91]

Meanwhile, a typical outflow strategy is to prescribe zero pressure, but this technique has been widely criticized[88,92,93] since it is physiologically akin to bleeding, with the cut vessel releasing blood into the atmosphere—decidedly different from the true dynamics in the vessel. It can also be interpreted as the merging of outflow branches downstream, which is seldom the case. The strategy is falling out of favor for more advanced splitting techniques that incorporate Murray's law or 0D models, both of which aim to control the outflow VFR through each outlet.[88,93,94] Chnafa *et al.*'s splitting method, used in this thesis, applies a power law identical in form to Eqn 2.7 to determine the percentage of flow that is diverted to each branch at a bifurcation.[93]

$$\frac{Q_1}{Q_2} = \left(\frac{d_1}{d_2}\right)^n \tag{2.8}$$

Here, the subscripts denote either vessel. No special attention is required regarding choice; that is, d_1 need not be larger than d_2.

The above constitutes a brief discussion of the most important aspects for simulating untreated aneurysms. Other considerations arise for modeling treatments.

2.4.4 Validation Techniques

Experimentally validating computational models against their physical counterparts ensures that current and future simulated results are useful. For fluid flow, validation typically includes visualizing the flow fields with an experimental setup through methods such as laser Doppler velocimetry or particle image velocimetry (PIV). The latter approach is well established in the field of IA hemodynamics and has been used to study, for example, the flow progression in a growing IA,[95] flow disturbances produced by bifurcation stents,[96] and the effect of wall compliance on CFD modeling.[97]

A schematic diagram of a typical PIV system is shown in Fig 2.13. PIV uses a pulsed planar light sheet, generated by passing laser or LED light through a series of lenses, to illuminate the path taken by fluorescent particles through a transparent model, or phantom. The tracer particles are small glass spheres on the order of 10–100 μm with a similar density to the working fluid and so are assumed to faithfully follow the flow.

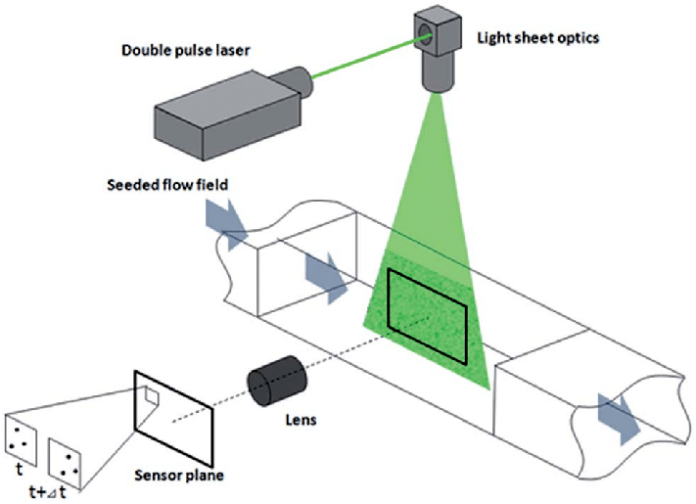

FIG 2.13 Shematic of a typical PIV setup.[98]

Refractive index matching between the fluid and phantom material is often used to avoid the optical distortion caused by refraction at the solid–fluid boundary. This facilitates data collection. Typical transparent solids used in research, such as silicone elastomers like SYLGARD 184 (Dow Inc, Midland, MI), have refractive indices of 1.33–1.51 and are commonly paired with aqueous sodium iodide solutions.[99]

The particle motion is captured by a digital camera and analyzed with software to find the instantaneous 2D velocity throughout the fluid domain. By synchronizing the camera with each laser pulse, the particle displacement between frames can be recorded; this, when combined with the known physical size of each pixel and the known time between laser pulses, yields a simple velocity calculation. (Of course, tracking the particles within a region is not this straightforward, but the general idea holds.) Particle motion toward

or away from the camera, i.e. normal to the plane, cannot be resolved, which can lead to interference. Stereoscopic PIV solves this issue by introducing a second camera at a different viewing angle to capture all three velocity components.

Additional experimental validation should be performed to ensure that the simulated velocity and pressure within the SMP*f* are reasonable, since an optical PIV system cannot probe the foam's interior. A permeameter (commonly used in geotechnical engineering) or flow loop like the one shown in Fig 2.14 can be used to determine the foam's permeability and form factor. A continuous flow of water is forced through the sample, and the flow rate is measured via a stopwatch and graduated cylinder or some other means. Pressure ports upstream and downstream of the sample chamber allow the pressure gradient across the sample to be calculated as

$$\nabla p = \frac{\Delta p}{l} = \frac{p_2 - p_1}{l} \tag{2.9}$$

where p_2 and p_1 are the upstream and downstream pressure measurements and l is the length of the sample. The Darcy velocity is then plotted against the pressure gradient for different VFRs. Recalling the form of the Darcy–Forchheimer equation (Eqn 2.5), a quadratic fit is applied to the data, and k and C are easily calculated.

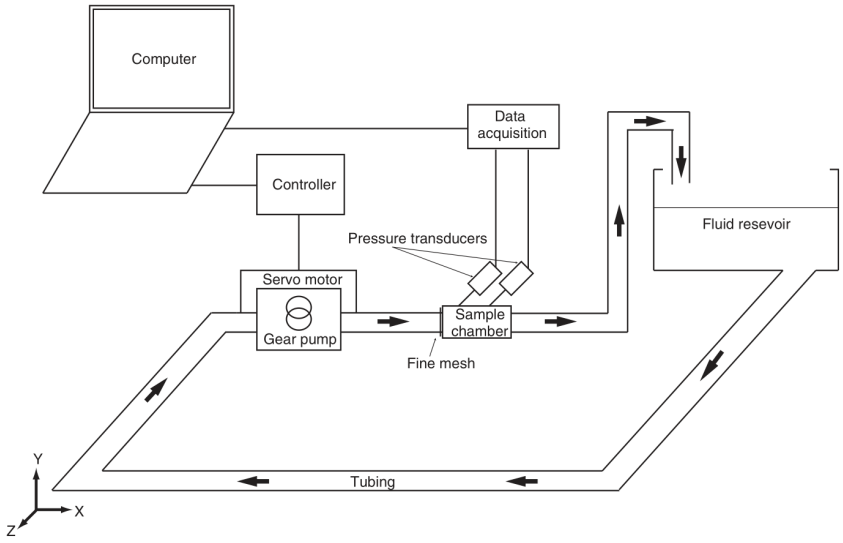

FIG 2.14 Schematic of a flow system for the measurement of porous medium parameters.[63]

3 COMPUTATIONAL MODELING OF UNTREATED ANEURYSMS

3.1 Introduction

The discussion now moves to the first of three numerical (or *in silico*) studies: simulating blood flow through different geometries to serve as both a control and a benchmark for the treatment simulations. As the previous chapter indicates, hundreds of studies have been performed to evaluate IA hemodynamics for a variety of purposes, and best practice standards have been proposed for most modeling decisions.[67] This study seeks to apply those best practices to provide a reasonable set of flow fields against which the treatments can be evaluated.

An overview of the model preparation and parameter selection processes is given in Section 3.2 and Section 3.3, whereas Appendix A provides a more comprehensive look. Section 3.4 includes a mesh independence study performed on a patient-specific geometry. A previously studied geometry[68] was chosen to allow for a comparison between the techniques used in this study and those used by other groups. Finally, simulation results for the untreated, patient-specific geometries are discussed in Section 3.5. All simulations in this study were run in the open-source CFD toolbox OpenFOAM-v2012, a fork of the OpenFOAM project developed by ESI Group (Paris, France).

3.2 Geometry Preparation

The saccular aneurysm geometries used in this thesis were derived from 11 anonymized, patient-specific 3DRA datasets gathered at the University of Oklahoma's Health Science Center in 2018 and 2019 (IRB #7932). The image resolution of 9 of 11 sets was adequate for image segmentation. Five unique geometries, 3 bifurcation and 2 sidewall, were chosen for modeling; the other available aneurysm geometries were similar to those selected. These 5 aneurysms were supplemented by 1 geometry taken from the literature[68] to make a comparison possible between the simulation techniques used in this thesis and those used by other research groups.

Image segmentation was performed in Amira (Thermo Fisher Scientific, Waltham, MA). The full extent of the vasculature within the imaging region was segmented, and a smaller region of interest was then identified near the aneurysm containing all upstream bifurcations and any major vessels downstream. Each voxel was a rectangular prism with dimensions 0.108×0.108×0.5 mm. Following segmentation of a dataset, the resultant surface, representing the geometry of the blood within the vasculature, was exported to an STL file.

The surface smoothing capabilities of Meshmixer (Autodesk, San Rafael, CA) were used to produce geometries free from the step-like surfaces typical of voxel-based data. The vessels were manually cut perpendicular to their cross sections to form inlets and outlets. For IAs in the anterior circulation, the ICA was included and clipped along the cavernous segment or farther upstream. As much of the vasculature as was available in the DICOM dataset was included to reduce the effects of the inlet boundary conditions.[78] Each outlet was truncated at around 2 times the vessel diameter, d, once its direction had been established.[75] The shortest geometry had an inlet length of $7d$, shorter than the suggestions from both Hodis *et al.* and Hua *et al.* It is common for researchers to include straight, cylindrical flow extensions. Doing so allows flow to develop further, but it is not obvious how this differs from simply prescribing a fully developed profile at the entrance, which does not describe the true, skewed profile in the cerebral arteries anyway.[100] One study investigated inlets for the common carotid artery and found curved inlet extensions to produce more consistent flow patterns, but noted that "without further information regarding the true CCA curvature and geometry there is insufficient justification for the use of a curved inlet section."[101] That stance was taken for all extensions in this thesis.

The full extent of the modeled vasculature for each geometry and closer views of the IAs are shown in Fig 3.1. Some key geometry characteristics are given in Table 3.1. Note that "B" and "S" signify "bifurcation" and "sidewall," respectively. Aneurysm B1 was taken from the 2015 International Aneurysm CFD Challenge. All others are anonymized patient-specific geometries gathered at the University of Oklahoma.

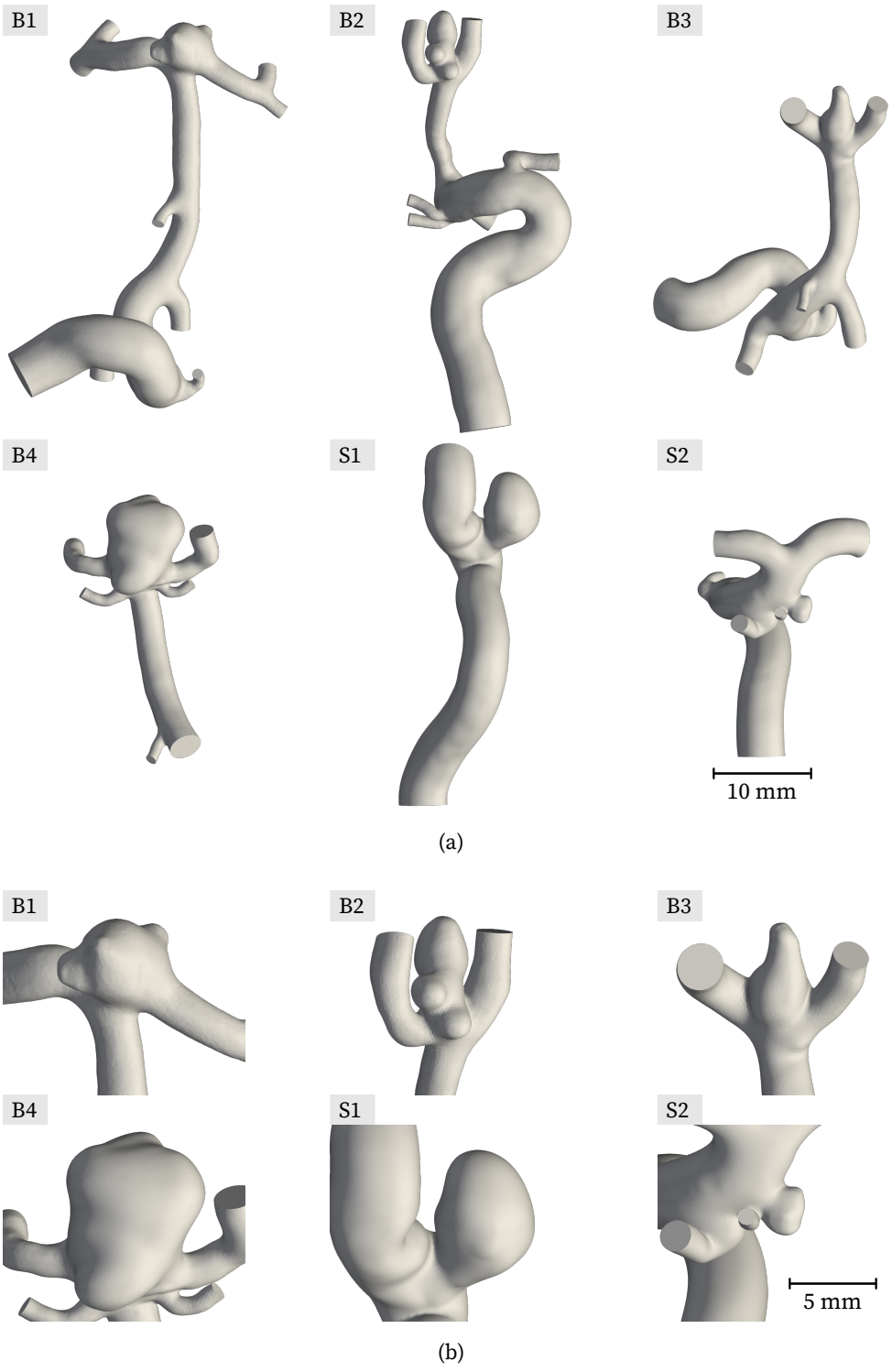

FIG 3.1 Patient-specific vasculatures and aneurysms. Sizes are true relative to one another. (a) Segmented vasculature for each geometry. (b) Close view of patient-specific aneurysms.

For more details regarding geometry preparation, see Appendix A. The discussion now turns to the choice of simulation parameters.

TABLE 3.1 Patient-specific aneurysm characteristics.

ID	Location	l_{max} (mm)	AR	SR	V (mm^3)	A_{ostium} (mm^2)
B1	MCA bifurc.	7.7	1.0	1.8	76	28.2
B2	MCA bifurc.	7.8	1.5	2.1	50	12.4
B3	MCA bifurc.	5.6	1.6	1.9	41	21.0
B4	Basilar apex	11.1	1.3	2.5	313	36.1
S1	Sup. hypophyseal	9.0	2.3	2.0	167	24.4
S2	Ant. choroidal	2.9	0.8	0.4	10	6.6

3.3 Simulation Parameters

Steady-state simulations were used in this body of work. The goal of this thesis is to guide the design of SMP*f* devices, and it is obvious that the greatest foam penetration occurs at systole. Since the velocity within the aneurysm space was the primary metric being considered, the study focused on that particular moment in the flow cycle. Moreover, because steady-state simulations at systolic flow tend to overestimate velocities,[82] this provided an upper bound on the worst-case flow that the foam device would experience. Accordingly, steady-state solutions were achieved using the SIMPLEC algorithm, and the residuals were monitored to ensure convergence. Simulations were run in parallel on 6 processors. Other solver settings are included in Appendix B.

The blood was modeled as an incompressible, Newtonian fluid with a dynamic viscosity μ of $3.65{\times}10^{-3}$ Pa s, a density ρ of 1050 kg m^{-3}, and a kinematic viscosity $\nu = \mu/\rho$ of $3.5{\times}10^{-6}$ m^2 s^{-1}.[102] The vessel walls were not assigned a material, but rather were treated as rigid following convention.[67] Although some literature[103,104] exists regarding constitutive modeling of the cerebrovasculature, the imaging technique used to gather the data for this study, 3DRA, cannot capture vessel wall thickness, so even with an accurate constitutive model, the walls would not be properly represented. A no-slip boundary condition was used along the wall.

The inlet boundary conditions were defined using peak systolic VFR values estimated from population-averaged flow waveforms for the ICA and basilar artery given in the literature for a normal, young cohort (9.26 mL s^{-1} and 5.63 mL s^{-1}, respectively).[105] Generalized flow waveforms for older adults were avoided because the age range of the present cohort was unknown, though either dataset likely would have produced similar flow patterns and WSS values.[106] The averaged waveforms were scaled using Eqn 2.7 according to a square law, which most accurately represents scaling for the ICA.[87] Gwilliam *et al.* do not report the mean vessel diameters for the cohort from which the average waveforms were derived, so an average value of $d = 4.9$ mm for the ICA[107] and $d = 3.4$ mm for the basilar

artery[108] were taken from the literature. The inlet diameter of each patient-specific geometry was calculated by averaging 6 different diameter measurements from the inlet to a point around 2 times the vessel diameter farther downstream to ensure that the diameter was not biased by only a single measurement.

Volumetric flow rates were assigned to all but one of the outlets according to the splitting method outlined by Chnafa *et al.*[93] Researchers have shown that a square law more closely models the junction exponent at the ICA terminal bifurcation,[109,110] while something closer to a cube law takes effect at the MCA bifurcation.[111] However, an exponent of $n = 3$ magnifies differences in diameter to the extent that it may lead to unphysiological flow rates when scaling,[87] so to be conservative, a square law was applied to all bifurcations regardless of location. This allowed Eqn 2.8 to be simplified, resulting in the following expression for flow splitting at each bifurcation.

$$Q_1 = \frac{Q_0 (d_1/d_2)^2}{1 + (d_1/d_2)^2} \tag{3.1}$$

Here, Q_1 is the desired VFR for either vessel in the bifurcation, Q_0 is the upstream flow rate, and d_1 and d_2 are the vessel diameters at the location. Diameter values were again calculated by averaging 6 different diameter measurements, beginning at the point of the bifurcation to a point around 2 times the vessel diameter farther downstream.

One outlet, typically the smallest, was left as a zero-pressure condition to allow the solver some flexibility with the fields, which was found to behave better than prescribing a VFR at each outlet. All other outlets had a zero-gradient pressure boundary applied.

Lastly, increasing evidence demonstrates that transitional or turbulent flow occurs in physiologic blood flow,[112] and turbulent flow has been observed in the aneurysm space after systole.[113] Accordingly, the $k-\omega$ shear stress transport turbulence model,[114] one of a class of Reynolds-averaged Navier–Stokes (RANS) models found to perform better for arterial flows than the standard $k-\epsilon$ model,[115] was used to predict turbulence in the model. It introduces two quantities, the turbulent kinetic energy k_t and the turbulent dissipation rate ω (of k_t into internal thermal energy), which are solved in two additional PDEs. (Note that it is not standard to write the turbulent kinetic energy k as k_t, but it is done in this thesis to avoid confusion with the permeability, also denoted k.) For the free-stream boundary conditions, i.e. the inlets, the quantities can be computed as

$$k_t = \frac{3}{2} u I^2 \tag{3.2}$$

$$\omega = \frac{\sqrt{k_t}}{l_t} \tag{3.3}$$

where u is the mean flow velocity, I is the turbulence intensity, and l_t is the turbulent length scale. For the purposes of providing boundary conditions for the vessel, laminar flow was assumed at the inlet, for which the intensity and length scale values are approximated as

$$I \approx 0.16\mathrm{Re}^{-1/8} \tag{3.4}$$

$$l_t \approx 0.038 d_h \tag{3.5}$$

Here, $\mathrm{Re} = ud_h/\nu$ is the Reynolds number and d_h is the hydraulic (vessel) diameter.

The only remaining simulation parameter is the mesh size for discretizing the fluid analysis domain, which is examined in the next section.

3.4 Mesh Independence Study

As discussed in Chapter 2, FVM results depend on the (temporo)spatial discretization of the model. To determine an appropriate spatial discretization, a mesh independence study was performed on a representative bifurcation geometry from the 2015 International Aneurysm CFD Challenge (identified as Aneurysm B1 throughout this thesis). This was done to allow for comparison to previously published results.

The geometry was first meshed with a base cell edge length s of 0.16 mm, just below the average cell size reported in the MATCH competition.[71] The number of cells in the mesh was approximately doubled each iteration by dividing s by $2^{1/3}$ (a reduction of about 21%) until reaching the final cell size of 0.05 mm. The mesh was hexahedron-dominated, with a few tens of thousands prismatic and tetrahedral cells incorporated along the boundaries, and was refined near the vessel wall with 6 inflation layers. Simulations were run with the parameters laid out in Section 3.3.

Following simulation completion, the maximum and average velocities for the entire aneurysm domain were calculated for each cell size. Moreover, the velocity magnitude was monitored at 1000 grid points within the aneurysm space, and the global mean absolute error (MAE) compared to the most refined mesh was computed. To prevent insignificant errors from inflating the global error, the slowest 1% of the sampled points, corresponding to a velocity of 0.03 m s^{-1}, was removed from the dataset. These results, as well as the mesh sizes, are shown in Table 3.2.

The average velocity is nearly identical for all cases, while the maximum velocity increases slightly with mesh refinement. The global mean absolute error of the sampled points is <5% for s = 0.08 mm and <2% for s = 0.06 mm. Indeed, the velocity contours for these two cell sizes are visually nearly indistinguishable from the most refined mesh (Fig 3.2). This aligns with previous studies[76–78] that have indicated a cell density of around 1700–1800 cells mm^{-3}, i.e. side lengths of roughly 0.08 mm, are sufficient to achieve mesh

TABLE 3.2 Mesh refinement results. Velocity values are in m s^{-1} and are calculated over the aneurysm domain.

s (mm)	Cells ($\times 10^3$)	IA cells ($\times 10^3$)	u_{max}	u_{avg}	MAE
0.05	12 450	938	1.106	0.494	–
0.06	7780	612	1.103	0.494	1.5 %
0.08	4160	329	1.097	0.494	4.4 %
0.10	2230	194	1.086	0.494	9.0 %
0.13	1150	106	1.061	0.490	15.9 %
0.16	687	67	1.054	0.490	18.3 %

independence within the dome. Thus, although there are minor flow variations, it seems reasonable to conclude that a cell size of 0.08 mm is an acceptable choice for the studies in this thesis, given the reduced computational cost (a speedup of around 6 times).

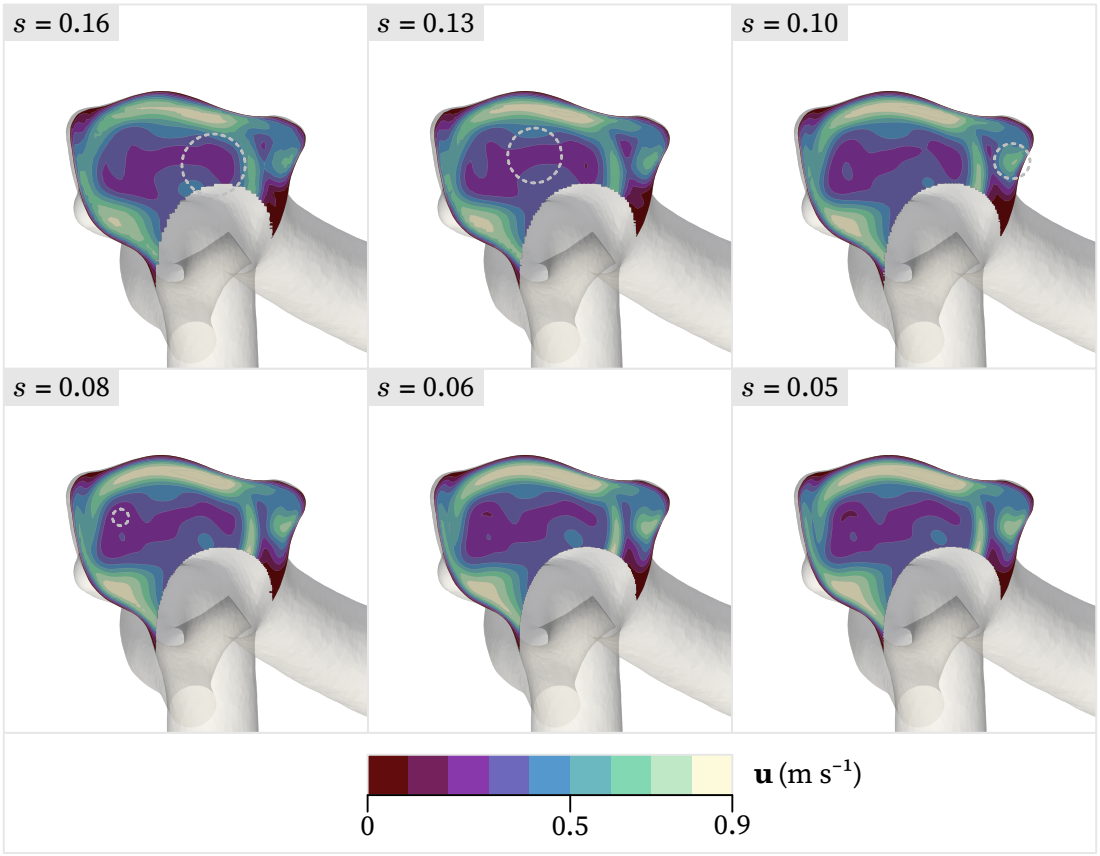

FIG 3.2 Demonstration of mesh independence within aneurysm space through visualization of velocity contours. Dashed circles indicate regions of dissimilarity with most refined mesh. Plane bisects aneurysm.

As an additional check on the simulation parameters, the mean ICA flow rate[105] of 5.11 mL s^{-1} was scaled and applied to the 0.08-mm mesh. This allowed the WSS values to be compared to the time-averaged WSS results for the six highly experienced teams in the 2015 International Aneurysm CFD Challenge,[68] since research has shown that the WSS for steady-state simulations closely matches the time-averaged WSS of pulsatile ones.[82] The purpose of that modeling challenge had been to identify and quantify the sources of inter-group variability in modeling, and the presented WSS values indicate why. Despite their experience, there was no clear consensus regarding the WSS magnitude between the teams. Three teams produced similar values, with a fourth in the same ballpark; the other two reported drastically different values.

Qualitatively, the simulation performed for this thesis is reasonably close to the three most similar WSS distributions from the challenge (Fig 3.3), although the values are higher in certain regions, particularly around one of the localized bulges in the aneurysm wall known as a "bleb." The spatially averaged WSS for the entire dome was calculated to be 5.48 Pa, slightly outside the reported interquartile range for the experienced groups of 1.83–5.40 Pa. Moreover, the WSS values almost appear to be smoothed out, which may be a result of the steady-state simulation. Nonetheless, it is obvious that this simulation depicts the same flow, and moreover, is in reasonable agreement with the most consistent cases presented by the other groups.

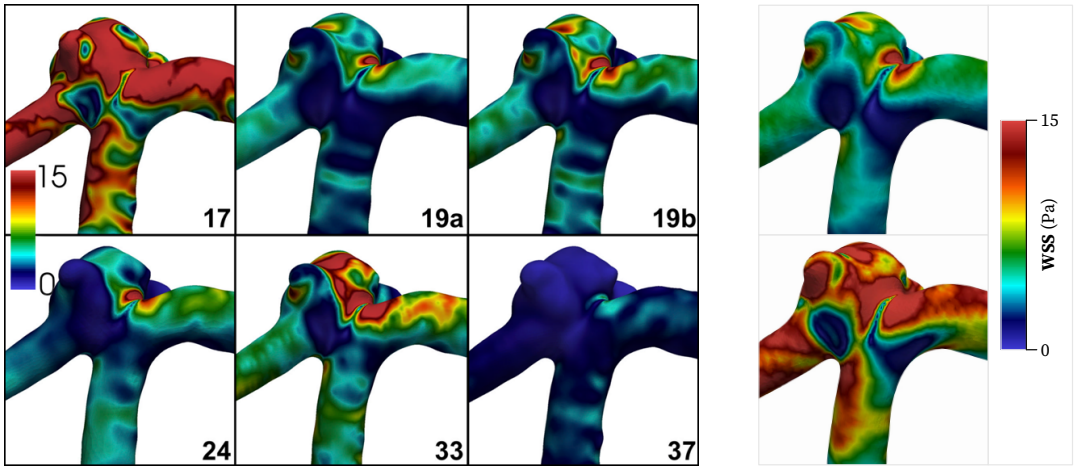

(a) (b)

FIG 3.3 Comparison of WSS values to select results from the 2015 International Aneurysm CFD Challenge. (a) WSS distributions for the six highly experienced teams in the 2015 Challenge.[68] Units are Pa. Layout reordered. (b) WSS distribution calculated for mean flow rate (top) and systolic flow rate (bottom).

3.5 Untreated Aneurysm Simulations

The results from the previous section provided a mesh-independent cell size and confirmed the general modeling approach. Each patient-specific case was prepared accordingly. The meshes ranged in size from 4.04×10^6–7.99×10^6 cells and consisted of a core hexahedral mesh with a base cell edge length of $s = 0.08$ mm surrounded by 12–20 inflation prism layers with a growth factor of 1.2. Inflows were defined using the peak systolic VFRs from the data by Gwilliam *et al.* All cases except for B4, located at the basilar artery apex and so requiring an inflow value scaled from the basilar artery waveform, utilized a scaled systolic value for the pre-siphon ICA. The scaled inlet values were found to fall within the physiological range.[105] Outflows were defined according to the flow splitting approach previously discussed, and turbulence was modeled using the $k-\omega$ shear stress transport RANS model.

Velocity was identified as the most important hemodynamic factor for this study. Accordingly, the maximum and average intra-aneurysmal velocities were calculated. They are given in Table 3.3. A plot of the velocity distribution throughout the entire aneurysm space for each case is shown in Fig 3.4. In Fig 3.5, the velocities are shown plotted on a plane running down the center of the parent artery and oriented through the aneurysm's maximum height. Highly complex flow is present in the parent artery for 3 of the IAs, particularly downstream of the aneurysm sac. Four of the 6 have a well-defined inflow jet surging through the center of the vessel that smoothly enters the aneurysm and stays tightly adhered to the wall, traveling over the top of the aneurysm and dropping back around to the neck. The situation for the other two, namely Case B2 and S1, is more complex. Based on these plots, it would almost appear that the blood loses all momentum upon entering the aneurysm space. In fact, the flow dramatically changes direction upon entrance, thus leaving the observed plane, as demonstrated by Fig 3.6.

TABLE 3.3 Intra-aneurysmal velocities ($\mathrm{m\,s^{-1}}$) for each patient-specific geometry.

ID	$u_{\max}$	u_{avg}
B1	1.107	0.494
B2	0.746	0.172
B3	0.775	0.328
B4	1.180	0.333
S1	0.997	0.219
S2	0.825	0.403
Avg	0.938	0.325
Std Dev	0.167	0.107

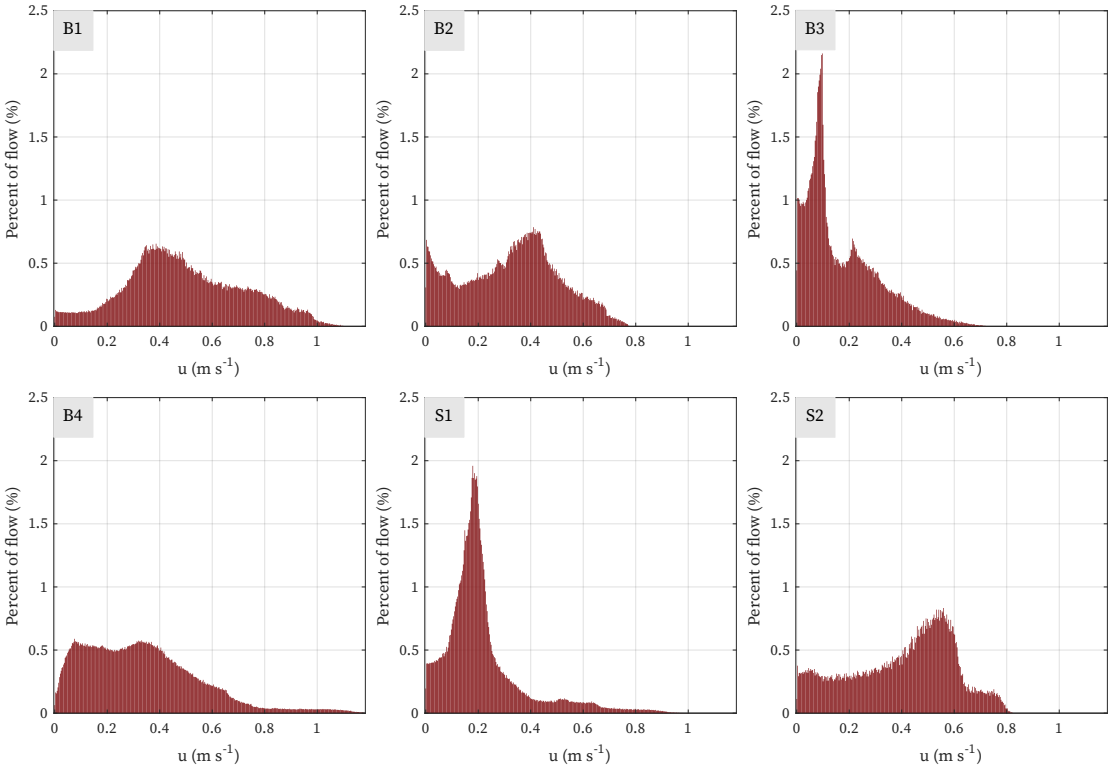

FIG 3.4 Velocity distributions in untreated aneurysms. Bin number is set as the square root of the number of samples in the smallest dataset. Bin width is approximately 3 mm s^{-1}.

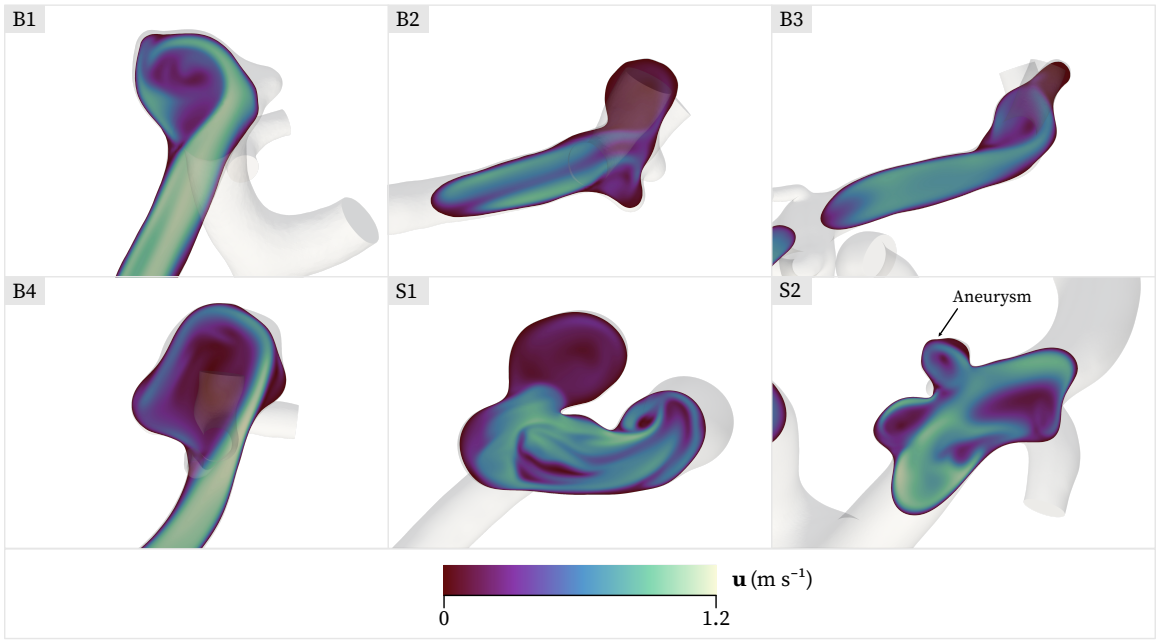

FIG 3.5 Visualization of velocity on the central aneurysm plane.

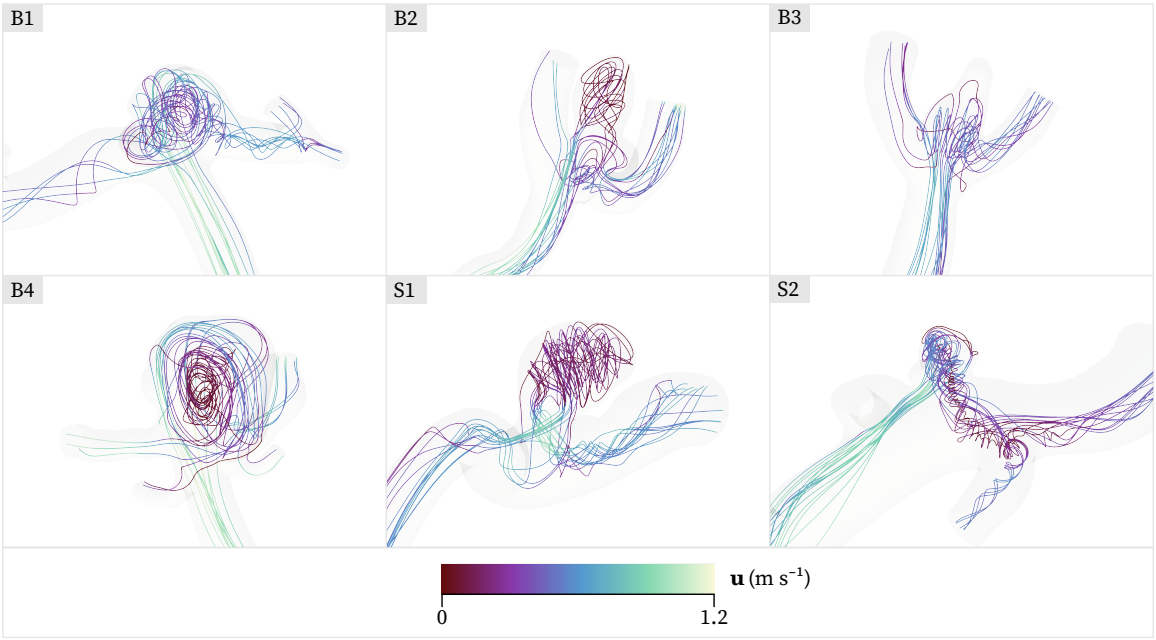

FIG 3.6 Streamline representation of flow through throughout the domain. Streamline seeds were placed within the aneurysm volume. Note the complex inflow pattern of Case S1 and the helical flow downstream of the aneurysms.

3.6 Discussion & Limitations

In this chapter, appropriate modeling techniques were determined for modeling the intra-aneurysmal hemodynamic environment within a set of IAs. A mesh independence study was carried out to determine a reasonable cell size for simulations. A case previously documented in the literature was investigated, and it was demonstrated that the modeling techniques used in this study produced results that are comparable to those achieved by other CFD studies. The baseline flow for 6 different patient-specific geometries was then well characterized. The average maximum velocity within the aneurysm space across the dataset was found to be $0.94\pm0.18\,\mathrm{m\,s^{-1}}$, while the overall average velocity was $0.32\pm0.12\,\mathrm{m\,s^{-1}}$. Additionally, various visualizations were produced for future comparison to treated aneurysms.

There are a few limitations to this study. First and foremost, without experimental validation, the accuracy of the results presented here cannot be known. Another known limitation is the use of population-averaged flow waveforms, which may lead to significant error in flow rates;[89] unfortunately, little can be done about this issue in the absence of patient-specific waveforms. Ultimately, the geometries were modeled using today's best practices for IA simulations.

Future extensions of this work are addressed in Chapter 6.

4 COMPUTATIONAL MODELING OF TREATMENT DEVICE

4.1 Introduction

With an idea of the native flow fields within these aneurysm geometries now in place, a comparison can be carried out to provide recommendations for the device design. Post-treatment IA hemodynamics are of great interest to the medical community, and over the years CFD researchers have identified two primary options for modeling these cases. First, modelers can handle the treatment material as a solid, e.g. by individually meshing the stent's wires. Second, the treatment can be modeled as a porous medium filling the aneurysm space. Both approaches have been used and compared for stents,[116] endovascular coils,[117] and (most pertinently) SMP*f* devices.[118]

Ortega *et al.* performed the first computational study of SMP*f* embolization devices in 2007, investigating heat transfer and flow dynamics within the aneurysm space during the virtual deployment of an idealized device.[81] The no-slip foam surface was treated as rigid and non-porous, and due to software limitations, the device was examined at three discrete stages of expansion rather than as a continuously growing mesh.

The group followed this with a more advanced effort in 2013, simulating the SMP*f* treatment of basilar aneurysms with two foam modeling methods that accounted for the foam's

porous properties, which the previous study lacked.[118] The first method employed micro–computed tomography imaging to obtain the 3D geometry of an SMP*f* sample. An intensity threshold was applied to the images to remove the faces between individual pores, generating an open-cell structure. This structure was directly meshed as a network of solid elements within the fluid domain, resulting in truly enormous meshes containing 30×10^6–300×10^6 elements since an exceptionally high resolution was necessary to simulate flow between the foam struts. For the second method, meanwhile, the foam was modeled using a continuum porous medium approach. In both cases, the foam was treated as rigid based on previous *in vitro* studies, which showed no significant foam deformation.[119]

Ultimately, the group has suggested that the continuum approach is adequate to represent an assessment of the SMP*f* treatment based on the overall similarity of flow trends between the two models, though they are careful to point out that fine-grained detail is lost with the porous approach that may be significant in individual cases.[118] Because the foam's structure is not directly modeled, the porous medium approach requires an understanding of its porosity and permeability. Section 2.4.4 explains how those parameters' values can be acquired.

The generation of patient-specific SMP*f* device models is discussed in Section 4.2, and Section 4.3 details a comparative study to experimental data (gathered by another group[63]) to verify OpenFOAM's porosity capabilities. Combining these results allows the devices to be used in a suite of simulations in Section 4.4.

4.2 Device Geometry Preparation

Treatment efficacy was evaluated by virtually implanting SMP*f* devices into the aneurysm geometries previously studied in Chapter 3. The device geometry for each case was generated by manually excising the digital aneurysm from the vessel mesh and reconstructing a smoothed, healthy vessel. The reconstructed vessel was then subtracted from the original mesh with a Boolean difference operation to leave only the geometry representing the blood within the aneurysm space (Fig 4.1). The devices for each geometry are shown in Fig 4.2. The devices are idealized, representing the maximum foam volume possible for the device, and do not account for manufacturing considerations.

4.3 Porous Media Modeling Verification

Due to the computational savings and this study's goal of offering general design suggestions rather than seeking to evaluate a patient-specific case in a clinical setting, for which a higher fidelity model may be necessary,[118] the decision was made to use a continuum

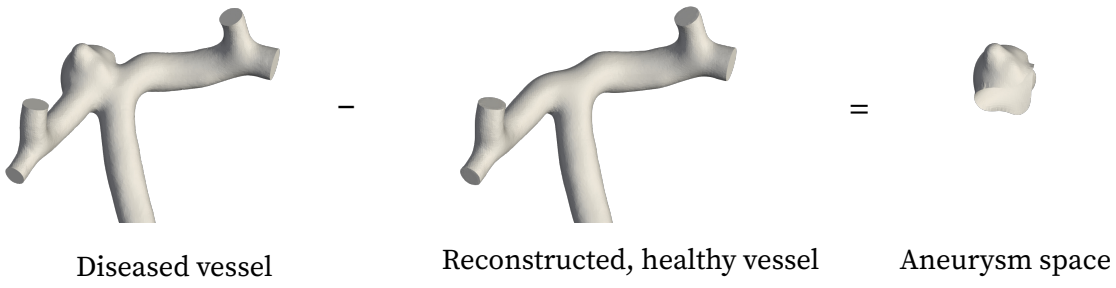

FIG 4.1 Creation of the SMP*f* device geometry with a Boolean operation.

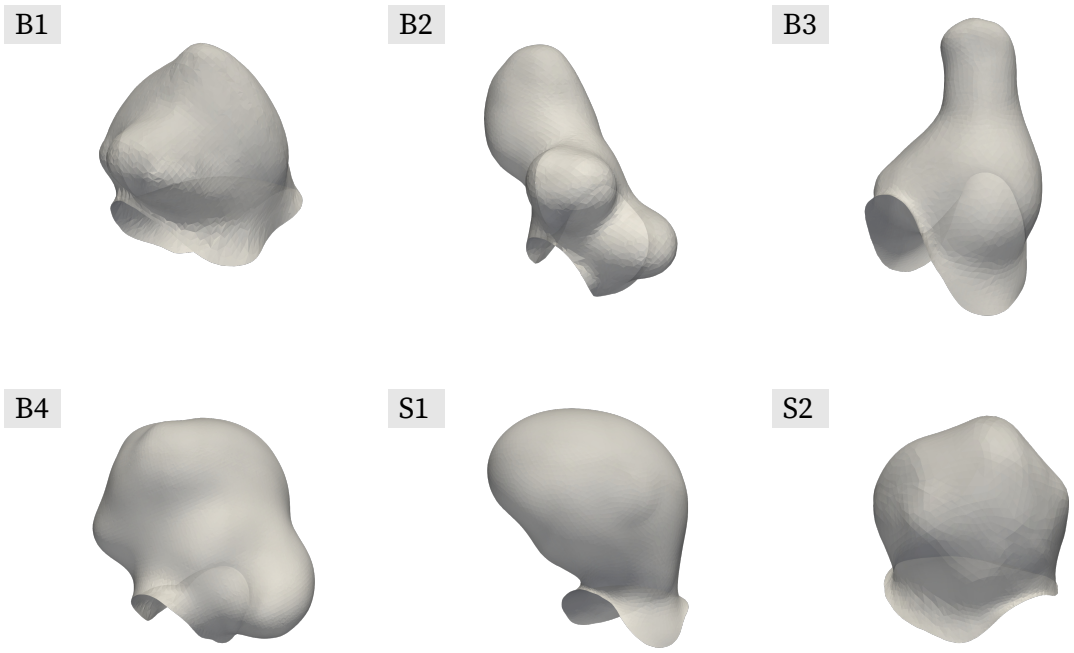

FIG 4.2 SMP*f* device geometry for each patient-specific case. Devices are shown with slight transparency so full neck region can be seen. Views are sized for clarity and are not to a consistent scale.

porous medium approach to model the foam. Accordingly, realistic porous media parameters were needed to properly assess flow.

The data used in this thesis was taken from Muschenborn *et al.*'s experimental investigation of the physical and mechanical properties of reticulated SMP*f* samples with a porosity value of $\phi = 98\%$, permeability values ranging from $k = 3.25\times10^{-9}$–1.24×10^{-8} m^2, and form factors ranging from $C = 2720$–7260 m^{-1}.[63] The permeability values for these foams are comparable to those examined in Rodriguez *et al.*'s[120] and Ortega *et al.*'s[118] similar studies, with form factors differing by orders of magnitude between the groups' investigations.

Mathematically, OpenFOAM models porosity as a sink term in the Navier–Stokes equations.[121] The Darcy–Forchheimer equation (from which Muschenborn *et al.*'s data is de-

rived) is one available model. However, it is necessary to manipulate the experimental permeability and form factor values for input into the software. The 1D Darcy–Forchheimer equation (given previously) and OpenFOAM's 3D implementation of it are shown here.

$$-\frac{\partial p}{\partial x} = \frac{\mu}{k} q + \rho C q^2 \tag{2.5}$$

$$\nabla p = -\mu \mathbf{D}\mathbf{u} - \frac{1}{2}\rho |\mathbf{u}| \mathbf{F}\mathbf{u} \tag{4.1}$$

Note that $\mathbf{D}$ is the permeability tensor and $\mathbf{F}$ is the form factor tensor. Both can be anisotropic, but they are assumed to be isotropic for now and so are reduced to the scalar values D and F. This suggests that the Darcy–Forchheimer parameters for OpenFOAM simulations can be calculated from empirical data as

$$D = \frac{1}{k}, \quad F = 2C \tag{4.2}$$

To confirm this, Muschenborn *et al.*'s experimental setup[63] was recreated *in silico*. The group performed permeability testing on cylindrical SMP*f* samples using an *in vitro* closed flow loop. Two SMP*f*s with different average cell sizes (0.7 mm and 1.1 mm) were produced and mechanically perforated the foams with a stainless steel acupuncture needle to achieve 4 hole densities ζ for each type. The samples had length l = 49 mm and diameter l = 16 mm and were placed in a tight-fitting sample holder with three pressure-port openings, located 15 mm apart from one another and equally spaced along the holder's length. The upstream and downstream pressure ports were used to gather data.

The steady inflow into the sample chamber was homogenized using a fine mesh. Data for each of the 8 samples was gathered at 4 different flow rates. The Darcy velocity was plotted against the pressure gradient for each test (Fig 4.3a), and a second-order least squares fit was applied to the data to determine the permeability and form factor values according to Eqn 2.5.

For this parameter verification study, the porous parameters were chosen from 2 of the 8 samples (Table 4.1), corresponding to the small–average cell size SMP*f* samples with the lowest and highest hole densities. To reduce the model's degrees of freedom, an axisymmetric cylindrical wedge with the aforementioned dimensions and comprising an angle of 5° was used rather than a full cylinder. The mesh was refined near the entrance and cylinder wall. Symmetry boundary conditions were applied on the axis and wedge sides to produce the correct behavior, and the entire domain was modeled as a porous medium.

To replicate Muschenborn *et al.*'s study, the corresponding flow velocity for each experimental flow rate was applied at the inlet. A zero-pressure condition was set at the outlet,

and the pressure gradient that developed across the sample was calculated from the OpenFOAM results according to Eqn 2.9. Simulations were run with turbulence modeling on to ensure proper porosity handling. As Fig 4.3 demonstrates, the OpenFOAM simulations were in good agreement with the experimental setup.

TABLE 4.1 Porous parameter selection from Muschenborn *et al.*'s data for porous media modeling verification.

Foam	ζ (holes m^{-2})	k (m^2)	D (m^{-2})	C (m^{-1})	F(m^{-1})
A	0.9×10^5	5.70×10^{-9}	1.75×10^8	7260	14 500
B	6.9×10^5	1.24×10^{-8}	8.06×10^7	2720	5440

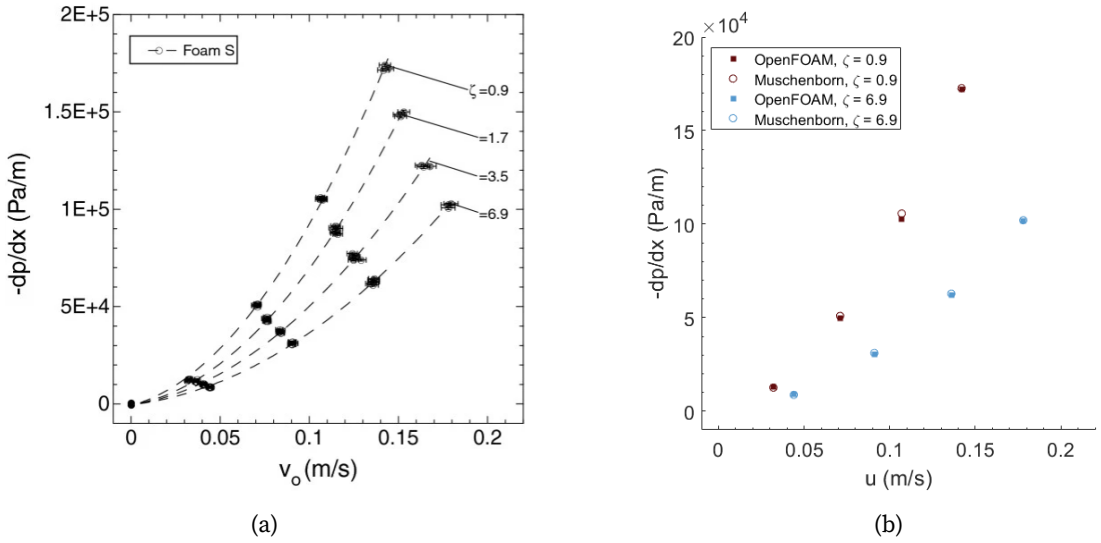

FIG 4.3 Verification of OpenFOAM porous parameter selection. (a) Pressure gradient versus Darcy velocity of Muschenborn *et al.*'s reticulated SMP*f*.[63] (b) Comparison of pressure gradient and Darcy velocity values between Muschenborn *et al.*'s experimental data and OpenFOAM simulations of identical setup.

4.4 Basic Device Investigation

An initial investigation was carried out on all 6 geometries with devices composed of the low-permeability, high–form factor foam (Foam A). An isotropic porous material was applied to the domain enclosed by each device. It was assumed that the foam did not deform due to flow impingement,[63,118] and hence, that the permeability and form factor values remained constant. The inlet and outlet boundary conditions, blood model, etc. were unchanged from the untreated cases.

A visual inspection shows that there is almost no blood penetration into the foam (Fig 4.4). High-velocity inflow jets are quickly dispersed within the foam or directed away altogether at the entrance. In fact, the location of the device's surface is obvious from the velocity visualization without even showing the foam; this is particularly clear for the sidewall aneurysms. In addition, the device appears to have stabilized downstream flow, as indicated by the smoother velocities in those areas.

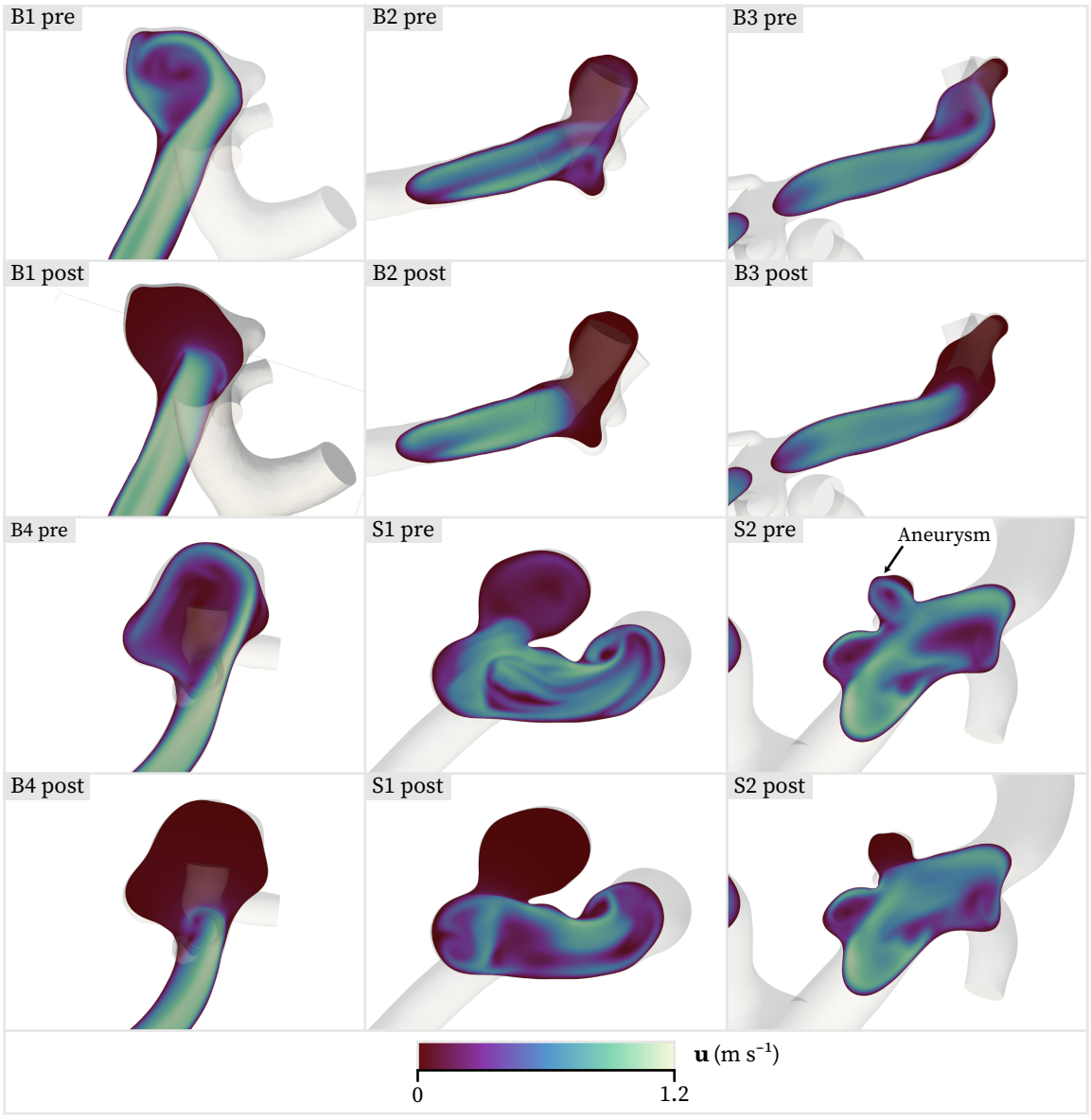

FIG 4.4 Comparison of pre- and post-treatment aneurysmal velocities on aneurysms' central plane.

The SMP*f*'s primary purpose is to lessen inflow into the aneurysm. One simple metric that can be used to evaluate its performance is the velocity reduction ratio (VRR), which

was calculated for all cases as

$$\mathrm{VRR}_m = \frac{u_{m,\mathrm{pre}} - u_{m,\mathrm{post}}}{u_{m,\mathrm{pre}}} \tag{4.3}$$

where the subscript m denotes the velocity metric of interest, e.g. the average velocity within the aneurysm space. A large velocity reduction was observed across the dataset: the maximum velocity within the aneurysm was reduced by over 40% for every case, and the average flow velocity by around 90%. Table 4.2 and Fig 4.5 demonstrate this flow reduction.

TABLE 4.2 Simulation results for the low-permeability SMPf, Foam A. All velocity values are in m s^{-1}.

ID	$u_{\mathrm{max,pre}}$	$u_{\mathrm{max,post}}$	$\mathrm{VRR}_{\mathrm{max}}$	$u_{\mathrm{avg,pre}}$	$u_{\mathrm{avg,post}}$	$\mathrm{VRR}_{\mathrm{avg}}$
B1	1.107	0.456	58.8 %	0.494	0.054	89.0 %
B2	0.746	0.387	48.2 %	0.172	0.017	90.0 %
B3	0.775	0.333	57.1 %	0.328	0.033	90.1 %
B4	1.180	0.488	58.7 %	0.333	0.022	93.3 %
S1	0.997	0.428	57.1 %	0.219	0.011	95.0 %
S2	0.825	0.329	60.1 %	0.403	0.048	88.0 %

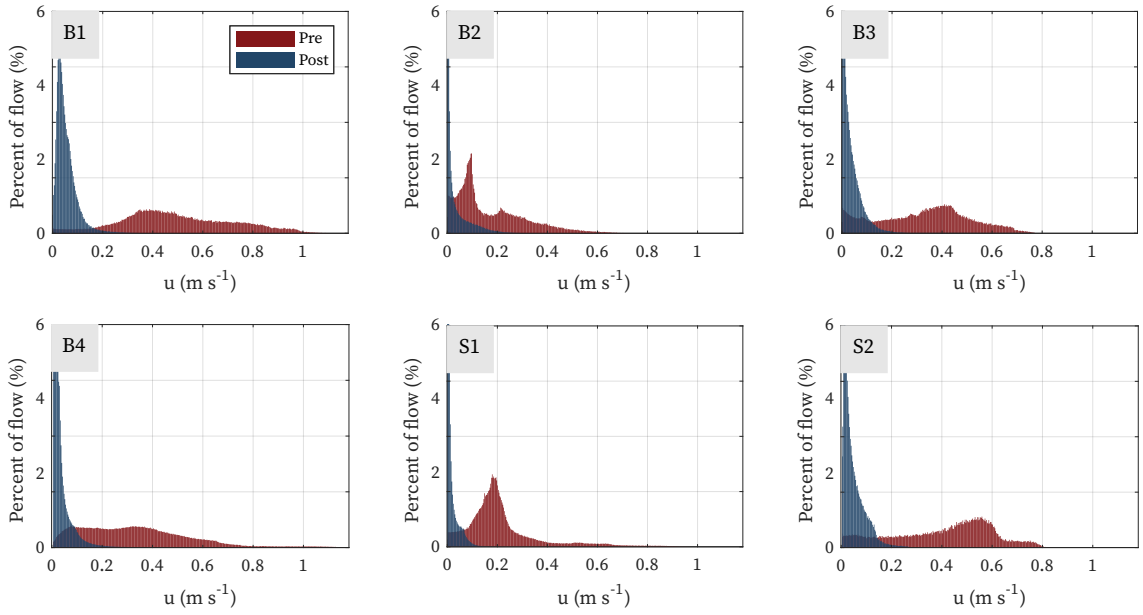

FIG 4.5 Velocity distribution comparison in pre- and post-treatment aneurysms. Legend applies to all subplots. Bin number is set as the square root of the number of samples in the smallest dataset, and bin width is approximately 3 mm s^{-1}.

4.5 Porous Media Parameter Study

The SMP*f* device can be designed with any range of properties. To determine its performance for other porous parameters, Case B1 was chosen as a comparison test case between 6 porous parameters derived from Muschenborn *et al.*'s data because it had the smallest VRR of the larger aneurysms. The parameters considered are given in Table 4.3 Foams A and B have been described previously. Muschenborn *et al.* also investigated the porous properties of embolic coils with different packing densities, testing them in the same manner as the SMP*f* samples. Foams D and F correspond to the effective permeability and form factor of embolic coils with a packing density of 28% and 11%.[63]

The parameters for Foams C and E were interpolated from the data using the geometric mean of the properties for the surrounding foams. For instance, the permeability for Foam C was found as

$$k_C = \sqrt{k_B k_D} \tag{4.4}$$

which evenly distributed the data points (the ratio $k_B/k_C = k_C/k_D$). Foam E was interpolated from embolic coil data and corresponds to a packing density of around 20%.[63]

As expected, a visual check indicates increasingly deeper blood penetration into the aneurysm (Fig 4.6), and the entire velocity distribution shifted toward higher speeds for each foam variety (Fig 4.7). Foams A–C provide an average VRR of 74% or greater (Table 4.4), dramatically slowing the inflow jet. Foam D only limits the maximum inlet velocity by 19% but still lessens the average aneurysmal velocity by 63%. Research has shown that a coil packing density of 20–25 % is necessary for good outcomes,[41] and this study comports with that idea: strong aneurysmal flow is visible for Foams E and F, the properties of which were based on coil packing densities of around 20% and 11%, while the clearly higher-performing Foam D was based on coils with a density of 28%.

TABLE 4.3 Porous medium parameters for each simulated material.

Foam	k (m^2)	D (m^{-2})	C (m^{-1})	F(m^{-1})
A	5.70×10^{-9}	1.75×10^{8}	7260	14 500
B	1.24×10^{-8}	8.06×10^{7}	2720	5440
C	2.24×10^{-8}	4.46×10^{7}	897	1800
D	4.05×10^{-8}	2.47×10^{7}	296	592
E	1.51×10^{-7}	6.63×10^{6}	110	220
F	5.61×10^{-7}	1.78×10^{6}	40.9	81.8

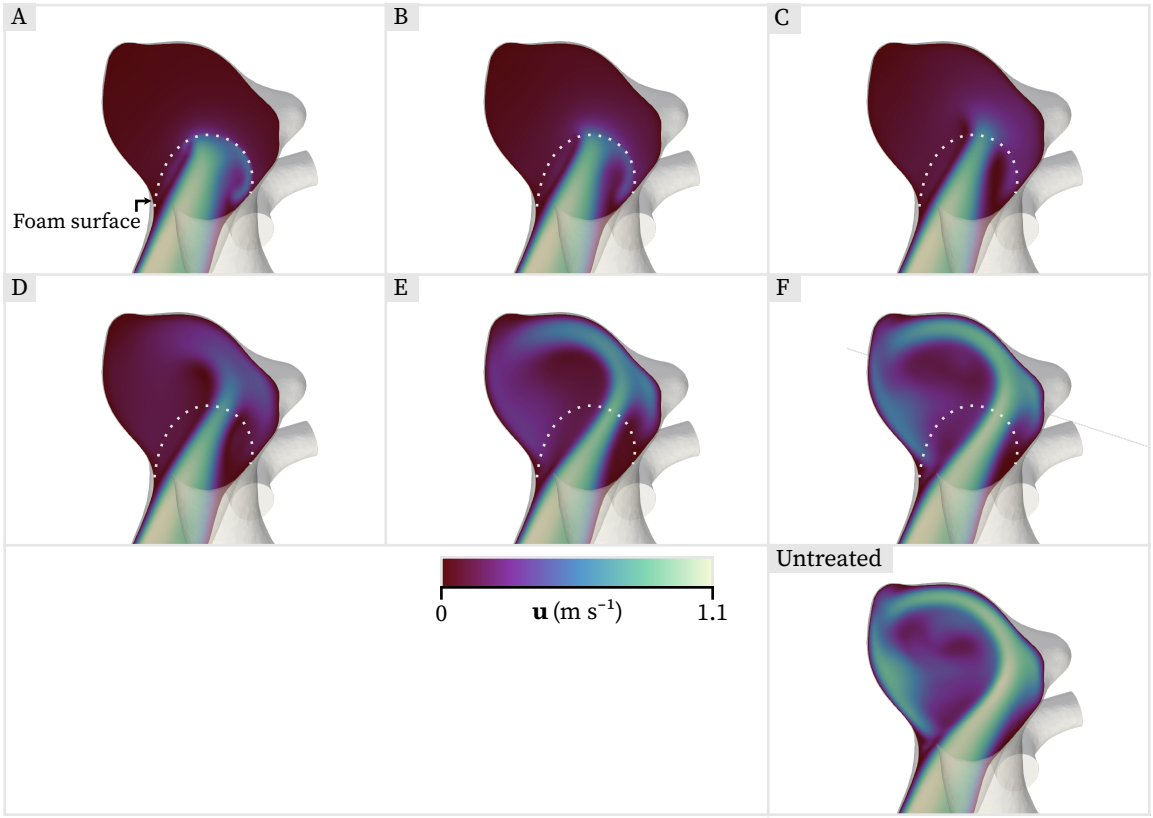

FIG 4.6 Velocity comparison between different SMP*f* types on the central aneurysmal plane for the same geometry.

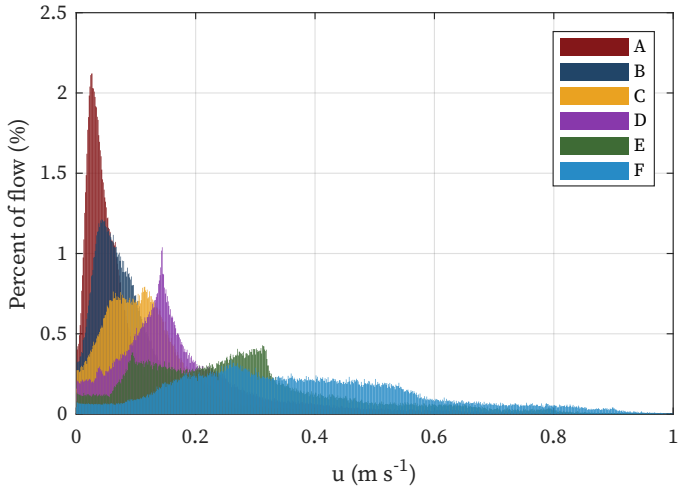

FIG 4.7 Velocity distribution comparison between different SMP*f* types for the same geometry.

4.6 Material Removal for Compressibility

One challenge facing SMP*f* devices is making them compact enough for catheterization. Horn *et al.* designed a hybrid SMP*f* device to address this issue consisting of two foam va-

TABLE 4.4 Intra-aneurysmal velocity comparison ($m\,s^{-1}$) for Case B1 treated with SMPf devices of differing porous parameters.

Foam	$u_{max,pre}$	$u_{max,post}$	VRR_{max}	$u_{avg,pre}$	$u_{avg,post}$	VRR_{avg}
A	1.107	0.456	58.8 %	0.494	0.054	89.0 %
B	1.107	0.582	47.4 %	0.494	0.087	82.3 %
C	1.107	0.788	28.8 %	0.494	0.128	74.0 %
D	1.107	0.899	18.8 %	0.494	0.184	62.8 %
E	1.107	0.972	12.1 %	0.494	0.277	43.9 %
F	1.107	1.043	5.8 %	0.494	0.381	22.9 %

rieties, a low-density, highly compressible inner core and a high-density outer ring visible to X-rays.[57] This study takes that approach a step further, examining how completely removing material from the device's core affects the flow field as a sort of bounding case for Horn *et al.*'s device.

Case B4, the largest IA in the dataset, was chosen both for its size and high untreated inflow velocities. Simulations were run with 2 SMPfs, Foam A and Foam D, and 3 different core sizes. The cored regions were cylindrical to approximate material removal with a drill or flat-end mill and were aligned concentrically with the parent artery, shown in Fig 4.8. The largest removed core (Core 4M) had a diameter of 4 mm. It was positioned such that the minimum distance to the device's surface was approximately 1 mm in any direction. Cores 3M and 2M had diameters of 3 mm and 2 mm and were evenly offset inward from 4M. The material removed for each device was approximately 25%, 10%, and 5% of the original volume.

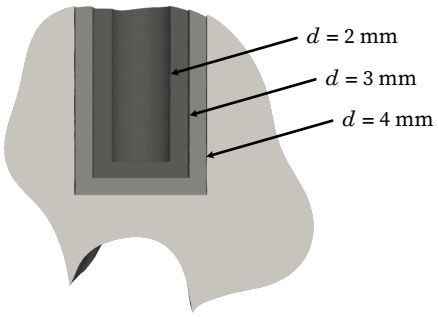

FIG 4.8 Cross-sectional view of cored SMPf devices for the same geometry.

Fig 4.9 demonstrates the effects of the material removal for both Foams A and D using an isosurface representation. Greater blood penetration and regions of somewhat faster flow become apparent as the core size increases, particularly for Foam D, which is 10 times more permeable than Foam A. However, although coring does allow these localized regions with increased velocity to develop, the maximum velocity and average velocity

throughout the dome are relatively unchanged—in fact, the only case for which the VRR_{avg} is not within 5% of the uncored case is for Device D4M (Table 4.5).

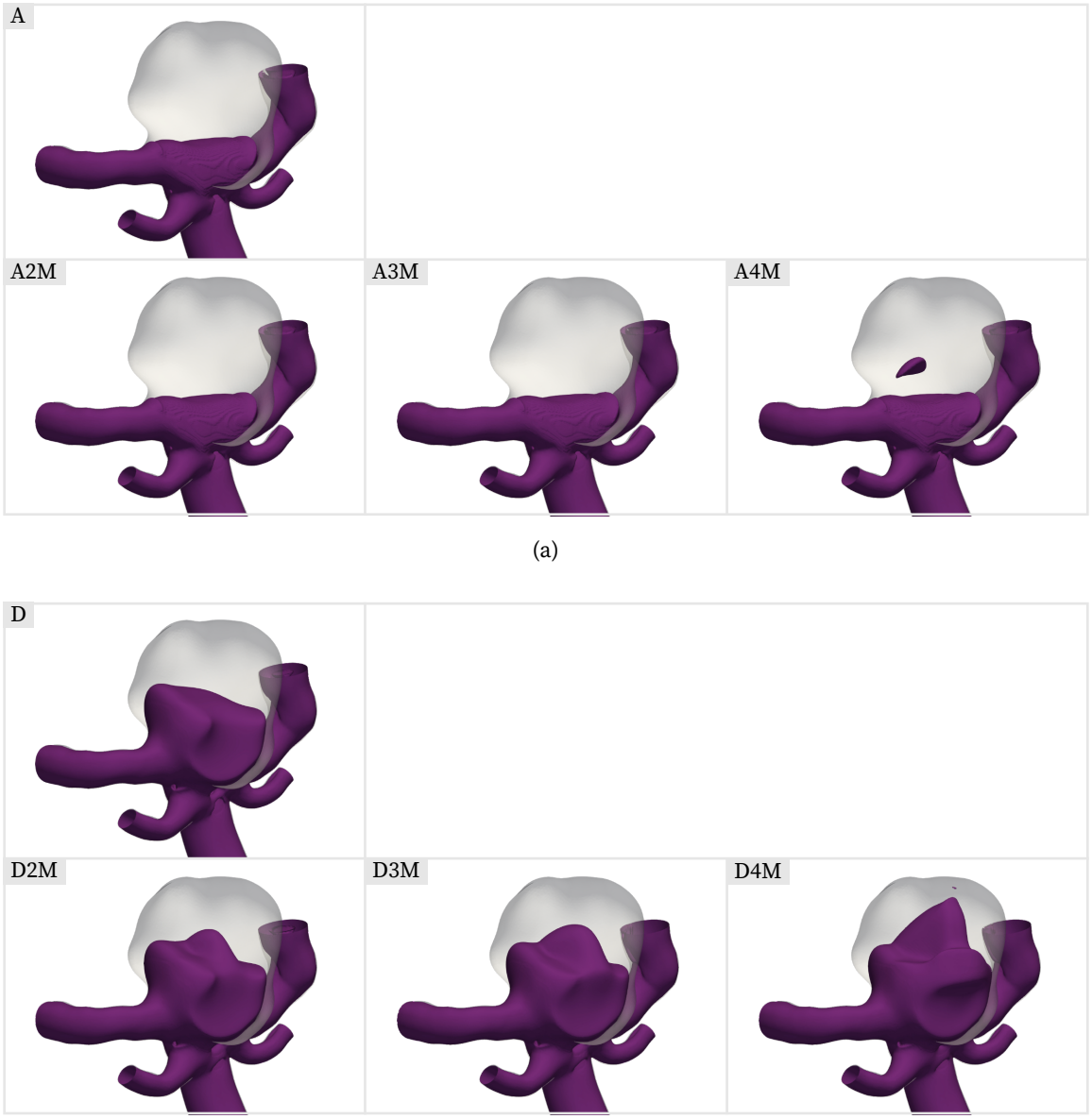

FIG 4.9 Velocity isosurface of 0.1 m s^{-1} for cored SMP*f* devices. (a) Foam A. (b) Foam D.

4.7 Discussion & Limitations

This study demonstrates that SMP*f* devices with a permeability on the order of 5×10^{-9}–5×10^{-8} m^2 are capable of greatly limiting blood flow into the aneurysm space, with average flow reductions of around 90% regardless of aneurysm type for Foam A, and an av-

TABLE 4.5 Effects of material removal from the device on the velocity distributions ($m\,s^{-1}$).

ID	$u_{max,pre}$	$u_{max,post}$	VRR_{max}	$u_{avg,pre}$	$u_{avg,post}$	VRR_{avg}
A	1.180	0.488	58.6 %	0.333	0.022	93.3 %
A2M	1.180	0.488	58.6 %	0.333	0.022	93.2 %
A3M	1.180	0.489	58.5 %	0.333	0.023	93.0 %
A4M	1.180	0.494	58.1 %	0.333	0.024	92.7 %
D	1.180	1.042	11.7 %	0.333	0.096	71.3 %
D2M	1.180	1.058	10.3 %	0.333	0.098	70.4 %
D3M	1.180	1.053	10.7 %	0.333	0.099	70.2 %
D4M	1.180	1.060	10.2 %	0.333	0.116	65.2 %

erage flow velocity of $0.03\pm0.01\,m\,s^{-1}$ across the dataset. Higher-permeability devices do not perform as well, allowing high-velocity inlet jets into the aneurysm space with speed reductions of less than 15%.

Importantly, the level of flow reduction for the lower-permeability devices matches or exceeds the reported values for achieving thrombosis with flow diverters. Ouared *et al.* found that a reduction of the average velocity by at least one-third the initial value was needed for successful long-term thrombosis in a group of 12 patients.[122] Meanwhile, the average systolic flow velocity for the 23 patients considered in Brina *et al.*'s study was reduced from $21.7\pm7.1\,cm\,s^{-1}$ to $7.2\pm2.9\,cm\,s^{-1}$ post-treatment, and 19 of those patients had a fully occluded aneurysm one year after stent placement.[123] Another similar study showed that patients with completely occluded aneurysms at 3 months had significantly slower mean intra-aneurysmal flow than patients with partial occlusion at 6 months ($1.13\,cm\,s^{-1}$ versus $3.11\,cm\,s^{-1}$).[124]

Research surrounding successful occlusion with endovascular coils tends to focus on the coil packing density rather than velocity reduction. Low packing densities, particularly those less than 20–25%, have been associated with failure in the literature,[41] though other studies have found that aneurysm geometry, size, and residual volume may play more important roles[41,125,126] Regardless, the low-permeability foams investigated in this chapter have permeability values much lower than the effective coil permeability, and because an SMP*f* device can be shaped precisely to a patient-specific geometry, residual volumes or necks are not a concern.

Of course, the mechanisms behind flow diverters, coils, and SMP*f* devices are different, and certainly flow reduction is not the only factor in play. For instance, endothelialization of the remnant aneurysm neck (regrowth of vessel wall tissue over the aneurysmal inlet) has been identified as crucial for complete occlusion,[127] and each treatment option has different materials and surfaces that affect this process (notably, the foam's surface serves as

a scaffold upon which blood can clot[128]). Nonetheless, the results of this study are promising, suggesting that SMP*f* devices with a permeability of 5×10^{-9}–5×10^{-8} m^2 should be further examined. Indeed, despite these other factors, one research group has concluded that although flow reduction does not guarantee aneurysm occlusion, it is the only hemodynamic parameter currently associated with treatment success for coils and diverters.[129]

Foam removal from the device's center for greater compressibility was found to be tenable (at least from a flow reduction standpoint) and should be considered for larger aneurysms. The size of the removed core will depend on the patient-specific geometry and the particular SMP*f*'s porous properties. In general, based on the results for a large aneurysm with a high inflow rate, it is recommended that the minimum thickness at any point within the expanded foam should be 1.5 mm after core removal. Devices at least that thick everywhere achieved maximum and average flow reductions that fell within 2% of those produced by an uncored device for both foam varieties.

There are some limitations to this study. As before, experimental validation is needed. Additionally, this study did not investigate anisotropic foams, which are common in practice due to the foam formation process.[118] The steady-state assumption also means certain possible foam benefits are simply absent from the analysis; for instance, prior research has shown that SMP*f* filters out high-frequency velocity fluctuations within the aneurysm space.[118] Lastly, these conclusions are being drawn from a small (albeit relatively diverse) dataset, so it is possible that the results cannot be as generalized as expected.

Future extensions of this work are addressed in Chapter 6.

5 COMPUTATIONAL MODELING OF DEVICE HEAT TRANSFER

5.1 Introduction

One concern regarding thermally triggered SMP*f* devices is the potential for thermal tissue damage. Proteins and lipids begin to denature at 45 °C,[130] and irreversible tissue damage has been found to occur in primate brains after an hour of exposure to a probe at 44 °C.[131] The SMP*f* being considered in this study has a glass transition temperature of T_g = 39 °C,[132] two degrees above body temperature. Preliminary heating experiments performed by other researchers at the University of Oklahoma that utilized a Joule-heating mechanism with the SMP*f* have suggested that it can heat from well below body temperature to its transition temperature in less than a minute, and can fully occlude a mock aneurysm space in that amount of time.[132] A short series of idealized heat transfer simulations was performed to determine the likelihood of damage and the conditions necessary for it to arise.

5.2 Initial Heating Investigation

An initial examination of device heat transfer was conducted for the beginning of the expansion process. The foam was modeled as a cylindrical, rigid-walled solid 1 mm in diameter, corresponding to the foam in its compressed state. The rigid-wall assumption

was considered justified since the pores are nearly entirely closed when the foam is compressed. The length varied between models due to the different geometries, but for all cases reached from the aneurysm neck to about 1 mm from the vessel wall. The device was centered within the aneurysm space such that the outward expansion (which was not modeled) would be approximately equal in the radial direction. The geometries are shown in Fig 5.1.

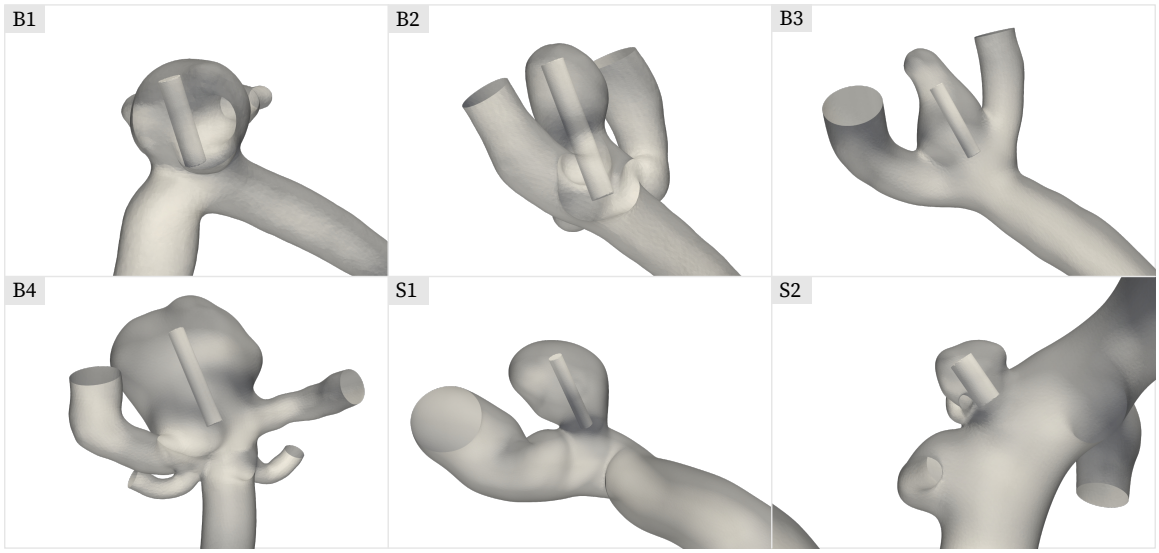

FIG 5.1 Heat source geometries representing the compressed foam before expansion. Views are sized for clarity and are not to a consistent scale.

It is desirable for the device to heat as little as possible, so a fixed temperature of 40 °C, just above the glass transition temperature of the SMP*f*, was first applied to the foam boundary to determine if a temperature increase could be detected at the vessel walls. A zero–heat flux (perfectly insulated) boundary condition was imposed on the vessel to model the worst-case temperature increase.[81] Flow through the inlet was set at body temperature, while flow through the outlets was calculated. A specific heat capacity c_p of 3600 J kg^{-1} °C^{-1} and thermal conductivity κ of 0.52 W m^{-1} °C^{-1} were assigned to the blood[102] through the dimensionless Prandtl number Pr = 25.4, calculated as

$$\mathrm{Pr} = \frac{c_p \mu}{\kappa} \tag{5.1}$$

Flow for this study was modeled at the diastolic VFR (2.98 mL s^{-1} for the average ICA and 1.77 mL s^{-1} for the average basilar artery)[105] to minimize convection from the region and maximize the temperature increase at the walls. Simulations were steady-state and incorporated RANS modeling, though the slow flow rates substantially reduced the instabilities seen for systolic flow.

Temperature isosurfaces for the heat transfer simulations are shown in Fig 5.2. Because this study was designed to examine if any heat was transferred to the walls, the chosen isosurface was modeled at only 0.5 °C warmer than body temperature. Heated blood generally does not make contact with any wall, whether in the aneurysm or the downstream vasculature. This makes sense for such a small temperature gradient and an unoccluded aneurysm space; even slow flow in the vasculature is fast enough to transport a liquid parcel many times the length of the aneurysm each second, so one would not expect much heat to be transferred to the walls via convection.

There are two exceptions. A thin stream of heated fluid impinges on the wall at a downstream bifurcation for Case B1, although the heat transfer from this is neglible. More concerning is Case B2. This is unsurprising given the results laid out in Chapter 3: Case B2 has the slowest maximum and average aneurysmal velocities in the dataset. Convection within the dome is so impeded that enough warmed fluid contacts the vessel wall at the aneurysm's apex to open up the isosurface, indicating the local wall temperature is above 37.5 °C. The presence of a closed isosurface at 39 °C signifies that the vessel is still below the foam's glass transition temperature.

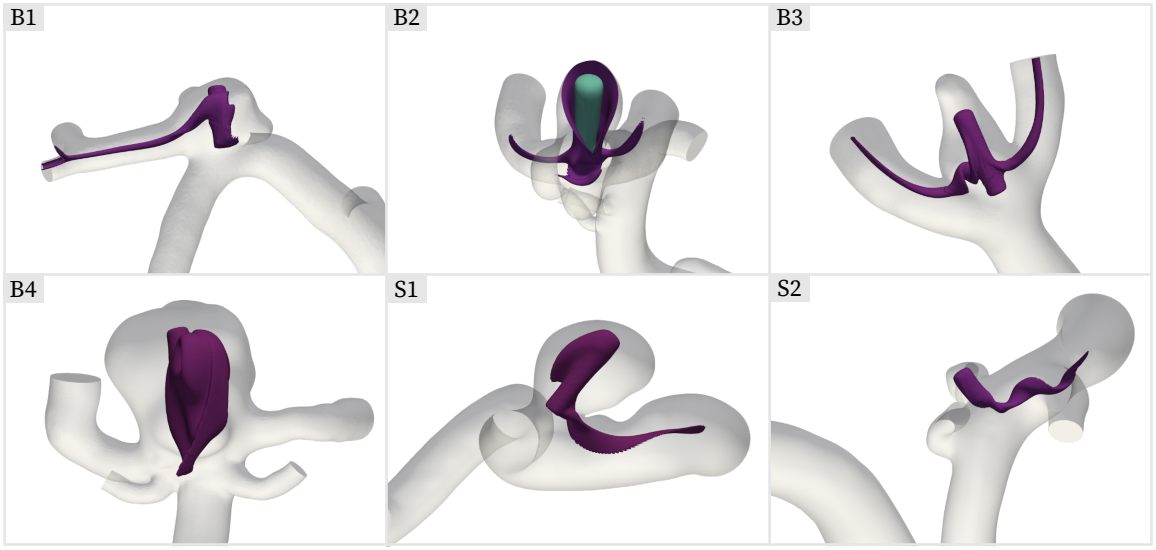

FIG 5.2 Temperature isosurface of 37.5 °C for steady-state heating in aneurysm geometries. Note the inclusion of a second isosurface (T = 39 °C) for Case B2.

5.3 Transient Heat Transfer During Device Deployment

Because Case B2 experienced the most significant wall temperature increase of any case, a short investigation of the transient heat transfer during device deployment was performed for this geometry. To limit the increased computational expense due to the larger number

of solution steps, the domain was shortened to roughly 3 parent artery diameters upstream of the IA and was remeshed with a base cell size of 0.20 mm to produce a mesh of 41 000 cells. It was demonstrated in Section 3.4 that cells around this size calculate the gross velocity field characteristics, such as the maximum and average velocity, to well within 5% of the most refined case, so this decision was justified.

To provide a more realistic flow condition than the previous diastolic study, outflow VFRs were calculated from the mean ICA velocity. All other boundary conditions were kept the same. Although the simulation was transient, the flow was still modeled as steady rather than pulsatile. The time step was chosen to be 1 ms, and a PIMPLE (combined PISO-SIMPLE) solution algorithm was used.

Two substudies were performed. First to be considered was heat transfer to the wall during the heating and expansion process. One geometry for the partially expanded SMP*f* device was used, and the heat transfer was evaluated at a low and high stimulus temperature. The foam was modeled as a porous region with the porous properties of Foam A. The device geometry was created by evenly offsetting the original geometry 0.5 mm inward from the wall (Fig 5.3), yielding a device that was approximately 40% expanded. Constant temperatures of 40 °C and 45 °C were applied to the entire porous region. The thermal properties of the region were assumed to be that of blood.

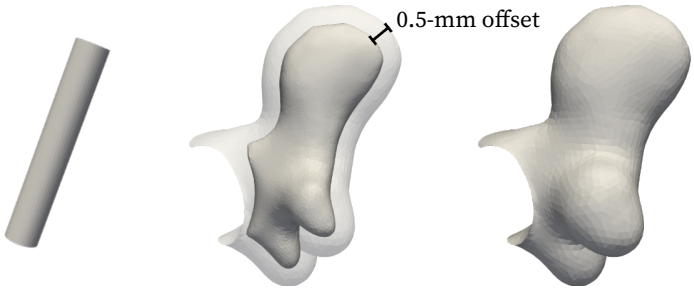

FIG 5.3 Selected geometry from the SMP*f* expansion process, shown with compressed and fully expanded states.

The second substudy examined the cooling process once the foam had fully expanded and the heating stimulus had been removed. The whole aneurysm space was modeled as a porous region with the properties of Foam A and was given an initial temperature of 40 °C or 45 °C as before. The temperature constraint was removed after 0.1 s, allowing convective cooling to occur.

The maximum wall temperature is observed to climb to 40 °C within 1 s for both stimulus temperatures due to the relatively slow flow within the dome and the small separation between the foam and wall (Fig 5.4). The blood flow pattern is such that only certain regions of the aneurysm reach elevated temperatures, while nearly all of the heated blood convected from those areas is driven into only one of the bifurcation vessels, dramatically

raising its wall temperature. Cooling, shown in Fig 5.5, is a much slower process, taking 62 s and 90 s for the cooler and warmer SMP*f* devices to fall to 37.5 °C. Fig 5.6 shows the time history of the maximum wall temperature for both processes.

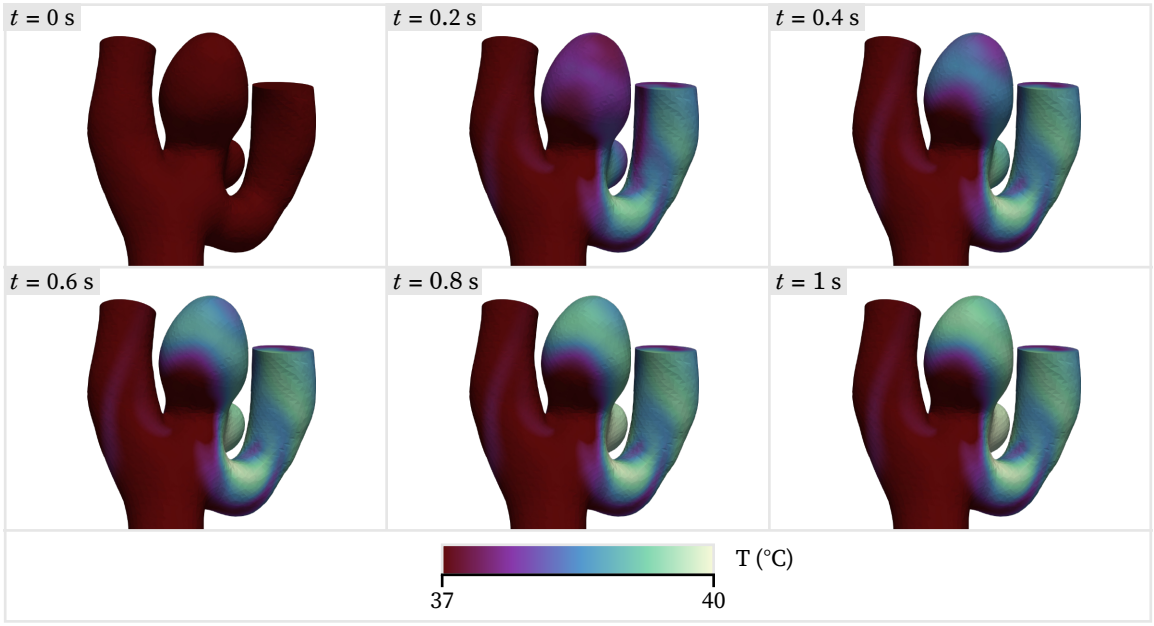

(a)

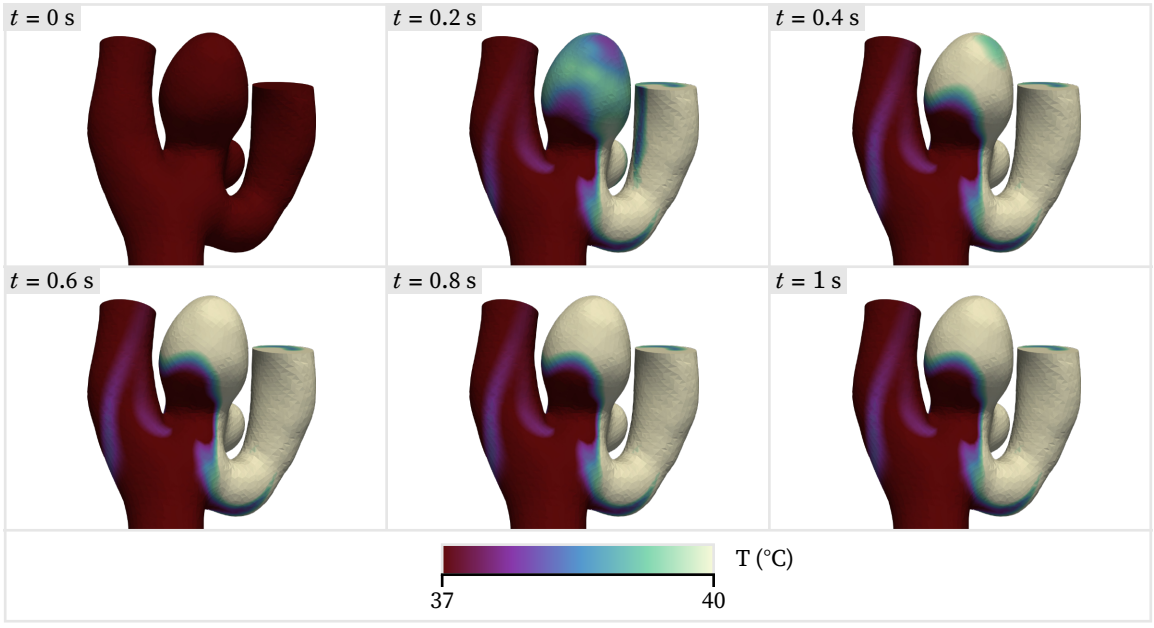

(b)

FIG 5.4 Temperature at wall over 1 s of the expansion and heating process, beginning with a 40% expanded foam. (a) 40 °C stimulus. (b) 45 °C stimulus.

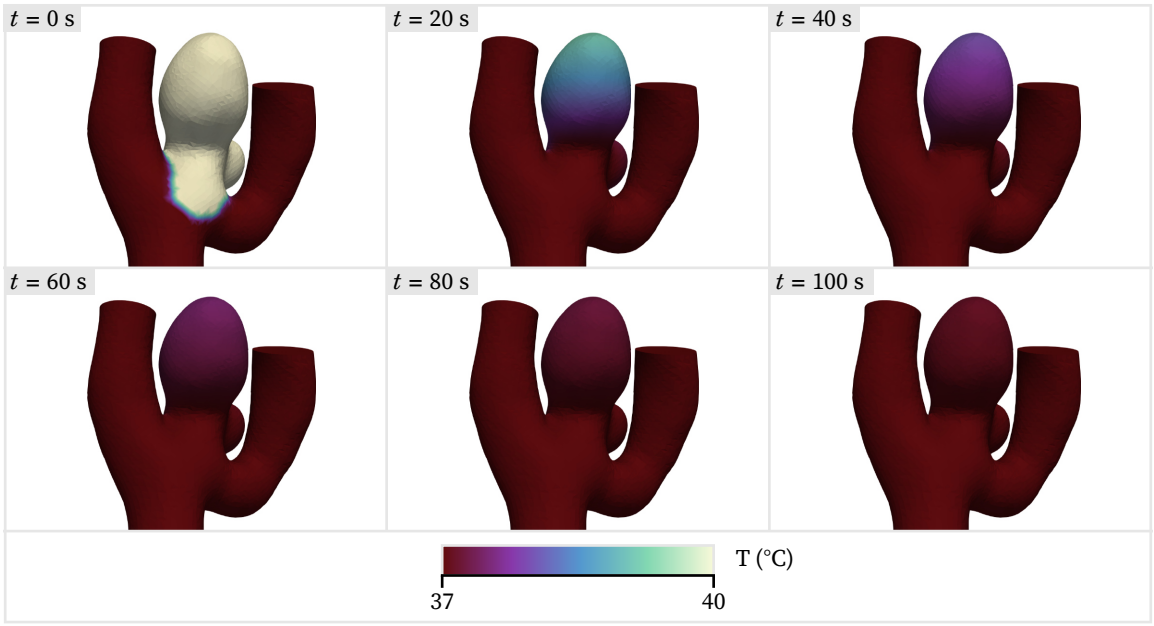

(a)

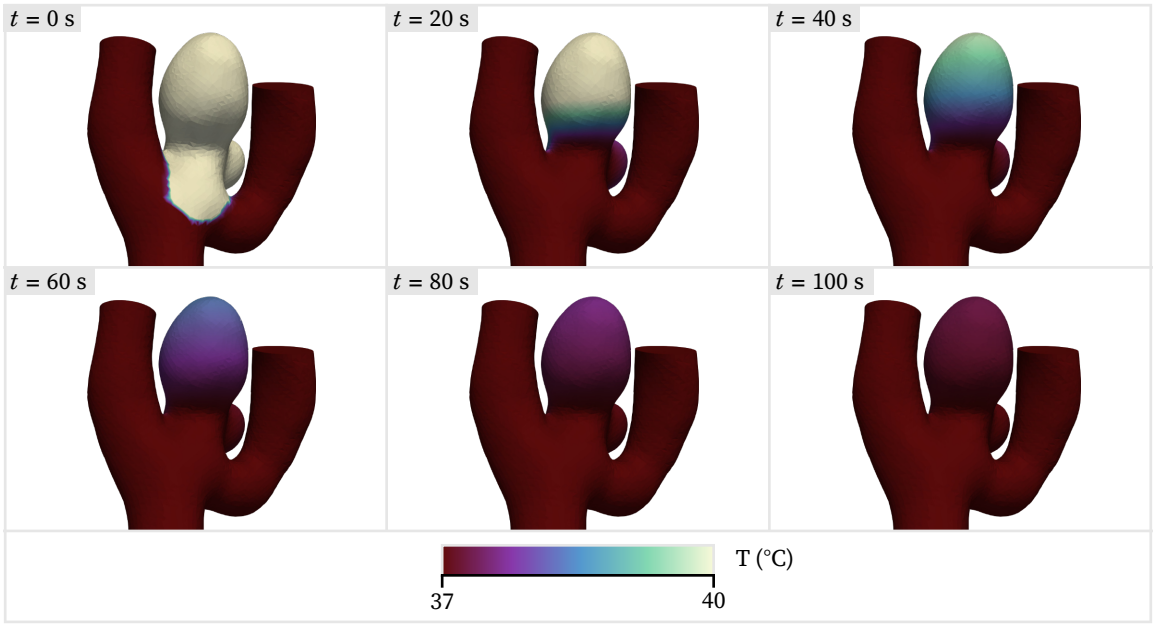

(b)

FIG 5.5 Temperature at wall during first 100 s of cooling after stimulus removal. (a) 40 °C stimulus. (b) 45 °C stimulus.

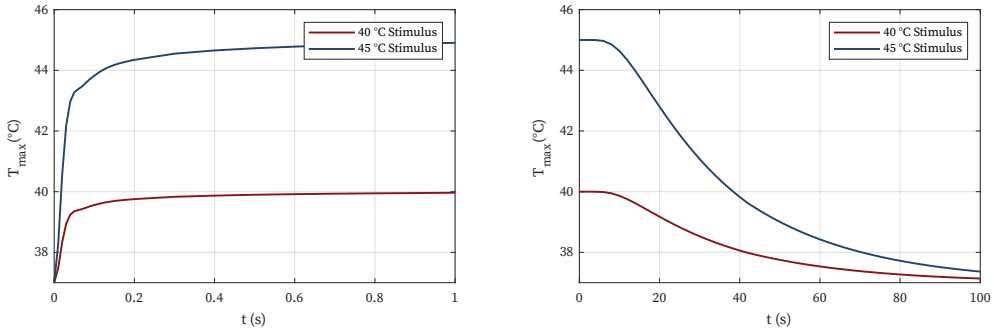

FIG 5.6 Time history of maximum wall temperature throughout the entire domain during the expansion and cooling processes. (a) Over the first second of heating for the partially expanded foam. (b) Over the first 100 s after stimulus removal.

5.4 Discussion & Limitations

Heat transfer from the device depends heavily on the particular aneurysm geometry and flow speed, as demonstrated by the fact that only one case had a wall region reach a steady-state temperature 0.5 °C above body temperature at the beginning of foam expansion. Furthermore, transient analysis of this case indicates that the wall temperature will approach that of the expanding SMP*f* within seconds. This likely generally holds true across cases; as the foam continues to expand, fluid is forced from the space and opportunities for convection are diminished. Of course, that may be perfectly safe if the device temperature is sufficiently low, but it is not immediately apparent what this temperature may be. One commonly used thermal dosage metric that can be helpful in determining the proper threshold is cumulative equivalent minutes at 43 °C (CEM_{43}), developed in the 1980s by Sapareto and Dewey[133] and defined as

$$\mathrm{CEM}_{43} = \int_0^t R^{43-T} dt \tag{5.2}$$

where t is the total exposure time, R is a constant chosen as $R = 0.5$ for $T > 43\,°\mathrm{C}$ and $R = 0.25$ for $T < 43\,°\mathrm{C}$, and T is the time-dependent temperature.

The previously found time histories for the heating and cooling process of the device can be combined to calculate the CEM_{43} dosage for Case B2. Assuming a total heating time of 1 minute,[132] the maximum vessel wall temperature curves throughout the entire deployment process become those shown in Fig 5.7. The areas under the curves are shaded as a reminder that integration is used in the formula.

Since the true temperature for the low-temperature stimulus is never above 40 °C, the CEM_{43} measure for the entire heating process is utterly negligible (0.02 min). Conversely,

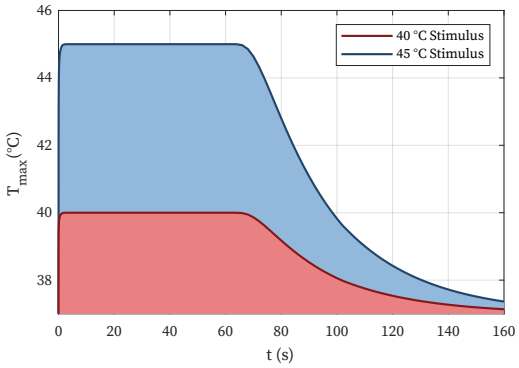

FIG 5.7 Maximum wall temperature time history throughout the entire deployment process.

the high-temperature stimulus experiences a worst-case CEM_{43} of roughly 4.9 min, where it is assumed that the foam is already largely expanded when heating begins. Various mammalian studies have found the threshold for brain tissue damage to be around CEM_{43} = 10 min,[134] though lower CEM_{43} values also affect the brain. For example, a temporary increase in brain cell death rate (lasting about 1 day) has been observed in rats treated to whole-body hyperthermia for a CEM_{43} of 5.9 min, and short-lived changes to metabolic rate and blood–brain barrier permeability have also been noted.[135] On the other hand, research on primate brains has found that brain tissue heated to a localized temperature of 44 °C shows no signs of irreversible damage.[131]

In light of these findings, the simulations in this study suggest that thermal tissue damage should not be a concern for thermally actuated SMP*f* embolization devices up to a stimulus temperature of 45 °C. However, it is still recommended that the temperature be kept as low as feasible, preferably below 43 °C. Shortening the heating process, if possible, is also desirable.

A number of limitations are recognized regarding this study. Any pulsatile effects, which could potentially drive warmer blood closer to the wall, were not modeled. Moreover, the study considered neither the foam's thermal properties nor the effect of conduction through the device, which may be the more important heat transfer process of the two. Tests with the carbon nanotube–infiltrated SMP*f* currently being investigated at the University of Oklahoma have demonstrated that the surfaces of 125-mm^3 samples (a reasonable aneurysm volume), can uniformly heat from 20 °C to over 30 °C in just 30 s.[132]

Future extensions of this work are addressed in Chapter 6.

6 CONCLUSIONS

6.1 Conclusions

In this thesis, the hemodynamic environment in a series of intracranial aneurysms was evaluated. The digital geometries were generated from patient-specific DICOM data, and standard practices in the field were implemented to best model the flow. After establishing the native steady-state flow fields within each aneurysm, a virtual SMP*f* device, modeled as a porous medium, was implanted into the aneurysm space. Devices with different porous parameters were tested in a wide-necked aneurysm to find the optimal permeability, and porous material was removed from a set of devices for a large IA to determine this approach's viability for aiding in device compression. Steady-state heat transfer from the thermally stimulated SMP*f* was investigated at the beginning of its expansion for all cases, and a more focused transient heat transfer study throughout the expansion process was performed for a complex aneurysm geometry with slow internal flow.

The results suggest that SMP*f* devices with a permeability on the order of $5{\times}10^{-9}$–$5{\times}10^{-8}$ m^2 can substantially reduce aneurysmal inflow, making this range the suggestion for device design. For one of the foam varieties investigated, the average flow velocity was reduced by around 90% for all cases, and devices with permeability values in the range given above reduced flow by at least 74% for a wide-necked aneurysm. The high untreated inflow velocity and large inlet surface area of this geometry implies that this outcome would hold for most cases. Additionally, the devices appeared to smooth out downstream flow profiles, particularly for sidewall aneurysms, which have chaotic outflow due to the angle with their parent artery.

From a flow reduction standpoint, material removal from the device's core has a negligible effect for the permeability range discussed above, and so should be a design consid-

eration for large aneurysms. It is recommended that the device has a thickness of at least 1.5 mm everywhere after core removal, although making it thinner would already likely be undesirable from a structural and manufacturing standpoint. Devices for both foam varieties considered had flow reductions within 2% of the uncored device's performance when that thickness was preserved.

This thesis also suggests that heat transfer from fluid convection within the aneurysm space should not be a cause of lasting tissue damage even if initial temperatures are at 45 °C, provided the heating time is kept to within a minute. It is unlikely that thermal tissue damage could be caused by the currently proposed heating temperature of 40 °C. Nonetheless, it is recommended that an abundance of caution is taken to keep temperatures and heating times as low as possible for the device.

6.2 Suggestions for Future Work

There are a few limitations of the work in this thesis that provide avenues for future research. Although every effort was made to simulate the IA hemodynamics using best practices, the flow results were not experimentally validated. Therefore, any results are ultimately a suggestion for a future line of inquiry. Moreover, the flow for all cases was modeled at steady-state, which means certain, possibly pertinent information, such as the effects of flow reversal on the foam or the effect of pulsatile flow on heat transfer, was lost. The thesis did not address the biochemically driven thrombosis process, choosing merely to examine hemodynamic factors. The scope of the thesis was also relatively narrow, focusing on foams within a tight range of porous properties and performing investigations on only a handful of geometries.

In light of these limitations, the most pressing extension of this work is the construction of an in-house flow loop for experimental validation of the three overarching studies (fluid flow, porous fluid flow, and heat transfer). It is recommended that this flow loop incorporates a PIV system to visualize the flow field within transparent aneurysm phantoms. It may be sensible to make the flow loop modular such that it can be used for permeability testing of the type performed by Muschenborn *et al.*, since the two applications are fundamentally similar.

There are many other possible extensions of this work. Performing pulsatile, time-dependent simulations may offer insight into flow behavior caused by inertial effects not foreseen by this work. Analysis of the device's deployment would also be useful in determining its overall viability. For example, examining the stresses induced on the vessel wall by the expanding foam (especially for an improperly oriented device), similar to the work by Hwang *et al.*,[61] would be beneficial in verifying device safety. Experimentally gathered

thermal properties of the SMP*f* could and should be used in heat transfer simulations to account for the effect of conduction through the foam during expansion.

Besides diverting flow, the foam also provides a scaffold upon which blood can clot. A study incorporating biochemical clotting processes has previously been performed for the 2D case by Horn *et al.*[128] Extending a similar study to three dimensions would give a more accurate representation of thrombosis in treated aneurysms than the simple flow diversion study detailed in this thesis, making it a candidate for future work.

A final possible extension is the incorporation of a fluid-structure interaction (FSI) approach to model blood flow–induced deformations in the aneurysm and foam. In such an approach, the surfaces are not rigid and can react to fluid motion. Accordingly, FSI modeling is more computationally intensive and requires more data, since both the fluid and solid domains are modeled. Gathering mechanical data on the foam would be relatively straightforward, but both local vessel wall thicknesses and a constitutive model for artery tissues derived from biomechanical data, such as that developed by Lu *et al.*,[136] would also be needed. The former, in particular, presents a challenge; current common imaging techniques cannot resolve the vessel wall, and FSI would offer no advantage without patient-specific measurements. Experimental validation could be performed using a compliant, thin-walled phantom in a PIV system as has been demonstrated by Geoghegan *et al.*[137] If properly performed, FSI modeling would offer a more accurate physiological representation of intracranial aneurysm blood flow patterns.

A OPENFOAM SIMULATION PIPELINE

This appendix outlines the digital model preparation, from segmenting the DICOM data to running the simulation, to aid future researchers in replicating the studies' results. Because the current process is not automated, precise replication cannot be accomplished. Nonetheless, such decisions can be guided, the purpose of this appendix. The workflow consists of the following steps:

1. Performing image segmentation on the patient-specific data in Amira to produce rough geometries.
2. Smoothing the geometries and creating the foam devices in Meshmixer.
3. Meshing the geometries; assigning boundary conditions, cell regions, etc.; and running simulations, all performed in OpenFOAM via an Ubuntu commandline.
4. Post-processing in OpenFOAM, Paraview, and MATLAB.

If more information about a particular software is needed, official documentation for Amira,[138] Meshmixer,[139], OpenFOAM[140], Paraview[141], and MATLAB[142] is readily available online.

A.1 Image Segmentation in Amira

Patient-specific DICOM data is opened in Amira (Thermo Fisher Scientific, Waltham, MA) by clicking **Open** and selecting the entire stack of images in the folder. Once loaded, switching to the Segmentation tab allows each voxel in the data to be assigned to a different region in a process known as image segmentation.

A variety of tools are available for segmentation; the efficacy of each is partly determined by tissue or material type being segmented. Recall that DICOM data of the cerebrovasculature is gathered by injecting a radiopaque contrast agent into the blood, which increases its reflectivity and therefore its brightness in the resulting images. As a result, the boundary between the vessels and surrounding tissue is distinct in high-quality data,

making it an ideal candidate for image thresholding. Thresholding is an image processing technique that selects all pixels (or voxels) possessing a brightness within a specified range. In Amira, this can be performed using the **Magic Wand** and **Brush** tools, as shown in Fig A.1. The geometry can be built quite rapidly using just these two tools.

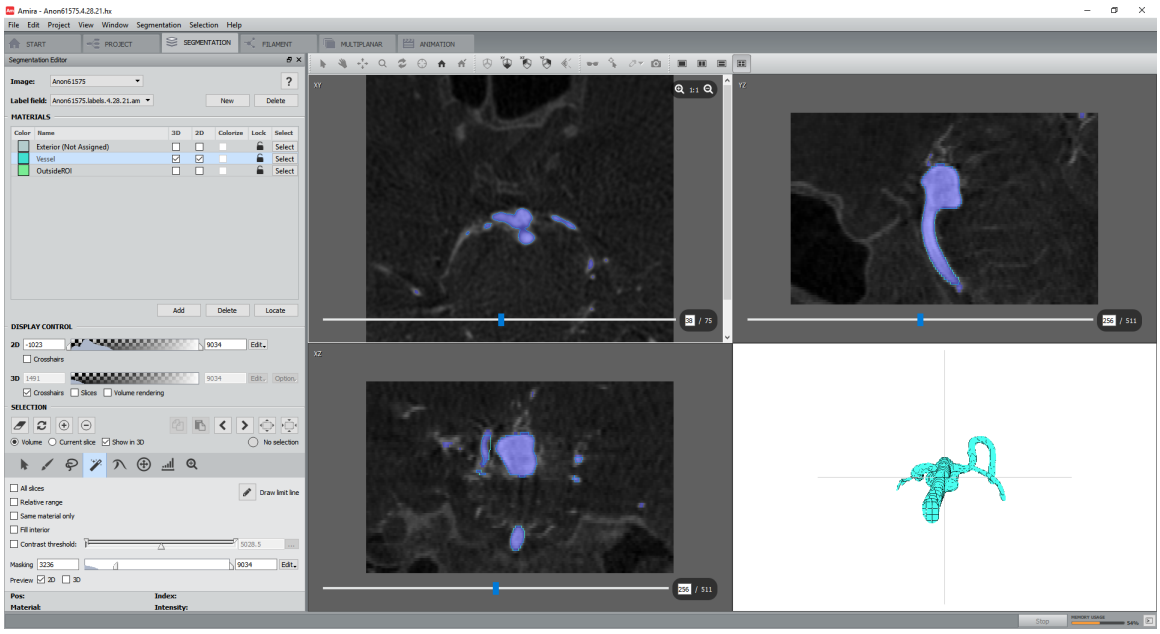

FIG A.1 Image thresholding view in Amira with the Magic Wand tool. Each of the three dark views is a stack of DICOM images mutually perpendicular to the others (called orthoslices). The dark blue regions displayed in the orthoslices indicate the voxels that are within the selected imaging threshold values and are available for segmentation. The bottom right view is the segmented surface.

Once the desired regions have been selected, all the voxels contained therein are added (+) to a material such as the Inside material created automatically by Amira. Tweaks to the geometry can be made by subtracting (–) material, which will move those voxels to the default exterior material.

The raw segmented object in Amira is a collection of voxels requiring further processing. Post-processing is performed in the Project tab:

1. Clicking the **.labels** data object opens a context menu near the top of the screen. **Generate Surface** is selected, creating a new data object.

2. The minimum edge length is set to some small, nonzero number to keep Amira from generating an excessive number of surfaces (0.05 is a reasonable choice). Although Amira has data smoothing capabilities, they are not as advanced as those in dedicated mesh-editing programs, so the smoothing step is omitted by selecting **None** instead of **Unconstrained Smoothing** in the dropdown. **Apply** generates the surface.

3. **Surface View** is selected within the new **.surf** object. It is automatically applied to create a **Surface View** object. A surface appears in the viewport. (If the exterior material is visible, the material is removed in the Buffer dropdown and the object is reapplied). This surface should be checked against the orthoslice in the window to verify that it accurately represents the data.

4. **Extract Surface** extracts the surface into a new object, **ExtractedSurface**, which is right-clicked. A button resembling a folder with an arrow is located at the top of the context menu; this is the **Export Data As** button. The surface is exported as an ASCII STL (.stl).

The final view in Amira's Project tab after surface generation looks something like Fig A.2.

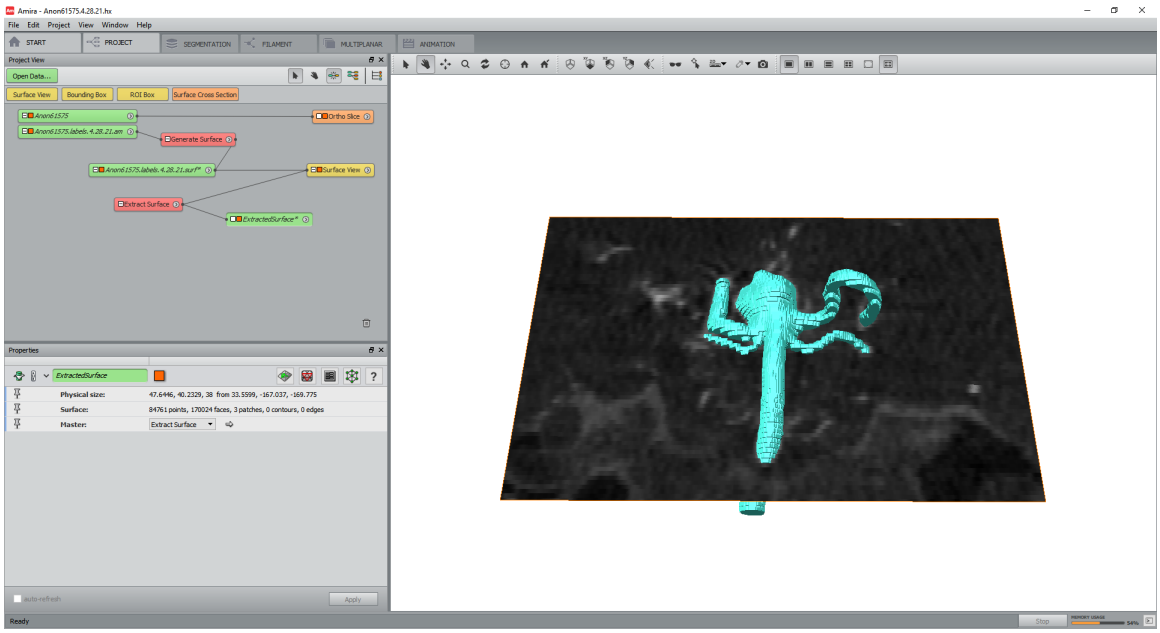

FIG A.2 Exporting a surface geometry in Amira. The different data objects used to create the surface are shown on the left, and the final geometry is displayed against an orthoslice on the right.

A.2 Geometric Manipulation in Meshmixer

The resultant STL file is opened in Meshmixer (Autodesk, San Rafael, CA) for smoothing using **Import** on the homepage (**Open** is reserved for Meshmixer files). Fig A.3 shows the imported geometry; it is a good idea to immediately copy this STL inside Meshmixer so a backup is always available in the project. The triangle mesh loads at its current location, which rarely coincides with the origin due to the coordinates used in Amira. The mesh can be translated to the desired position using the **Transform** (**T**) tool.

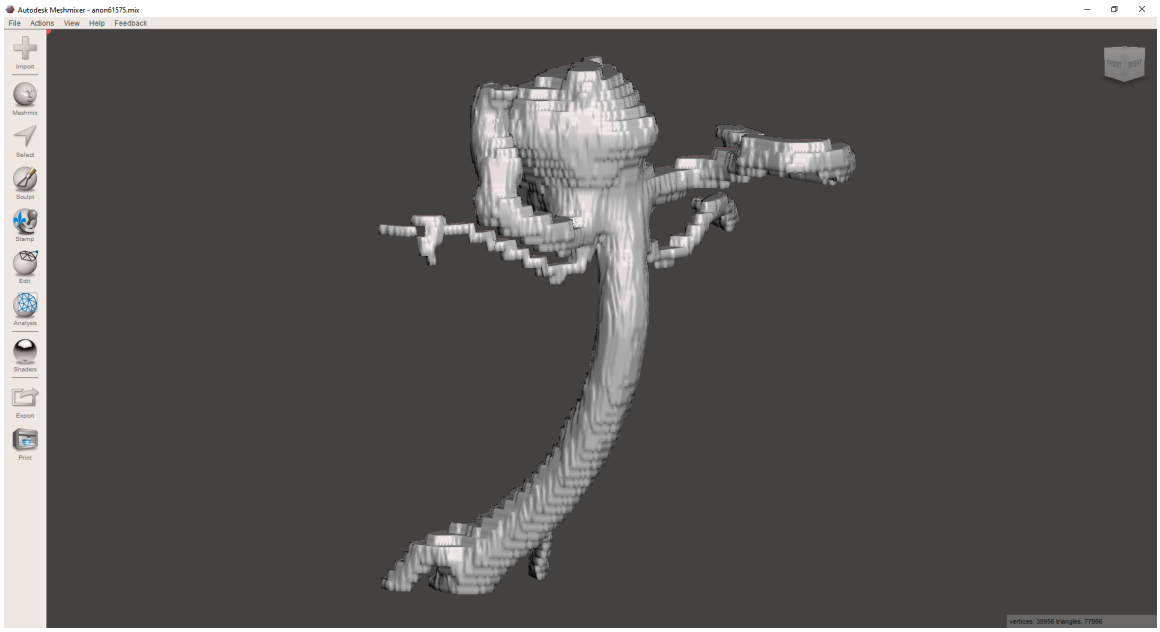

FIG A.3 An imported STL file in Meshmixer.

Meshmixer has robust smoothing controls accessed by selecting the entire geometry (**Ctrl + A**) and using the shortcut **Ctrl + F**. The default settings can be tweaked if necessary. Viewing both the original STL and the smoothed geometry at the same time is advisable to ensure the smoothed geometry is an accurate representation of the original, as simulations are sensitive to geometry variability and oversmoothing can lead to quantifiable differences in WSS values.[143] It is also helpful to remesh the geometry (**R**) to keep the triangulation uniform.

The smoothed geometry now cuts through the stair-like surfaces of the STL at the midpoint of each step (Fig A.4a). However, in reality, the geometry should fully enclose the STL, because the steps correspond to voxels located entirely within the segmented geometry in Amira. Therefore, the Offset tool is used to fully enclose the geometry by moving the surface outward (Fig A.4b). A small set of faces at an inlet or outlet is selected, and the selection is then inverted to select the rest of the geometry. (If an entire geometry is selected, the **Offset** tool creates an inner and outer surface, rather than shifting the faces.) Because the height of the voxels is 0.5 mm, an offset of 0.25 mm encloses the original surface.

In some instances, Meshmixer's smoothing algorithm can remove relevant aneurysm features. Further mesh manipulation is achieved using the **Inflate**, **Move**, and **RobustSmooth** sculpting brushes, being careful to constantly compare the smoothed geometry to the original STL. Once the geometry has been smoothed and matched to the original STL, the **Plane Cut** tool is used to manually cut the vessel ends perpendicular to their cross section to create the inlet and outlets, finalizing the geometry (Fig A.5). Each inlet and outlet is assigned to its own face group (**Ctrl + G**), made into a new object with the **Separate** function (**Y**), and

(a)

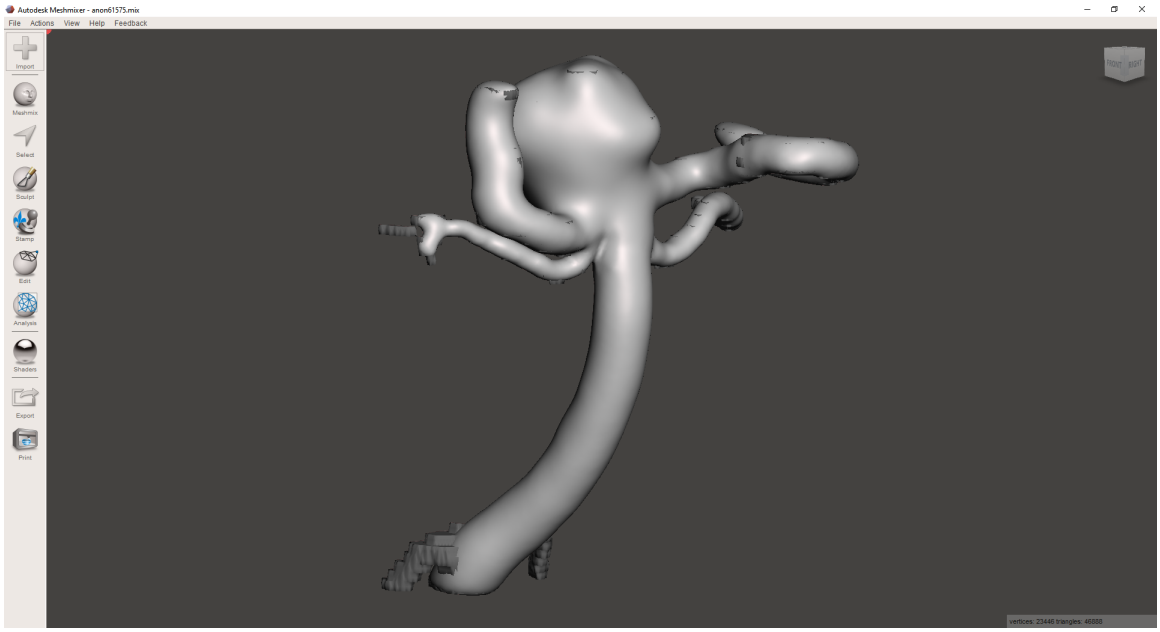

(b)

FIG A.4 The smoothing process in Meshmixer. (a) The initial smoothing step. Note how the light gray smoothed surface cuts through the step-like surface of the original STL. (b) The smoothed surface after offsetting the faces. The original STL is now essentially fully enclosed, and the smoothed surface closely follows it.

exported to an STL (**Export**) in the ASCII format. The remaining vessel wall is also exported as an STL. These STLs must be copied or moved to a folder named `constant/triSurface` within the main simulation case directory to allow OpenFOAM to locate them. See Appendix B for the detailed directory tree used in OpenFOAM simulations.

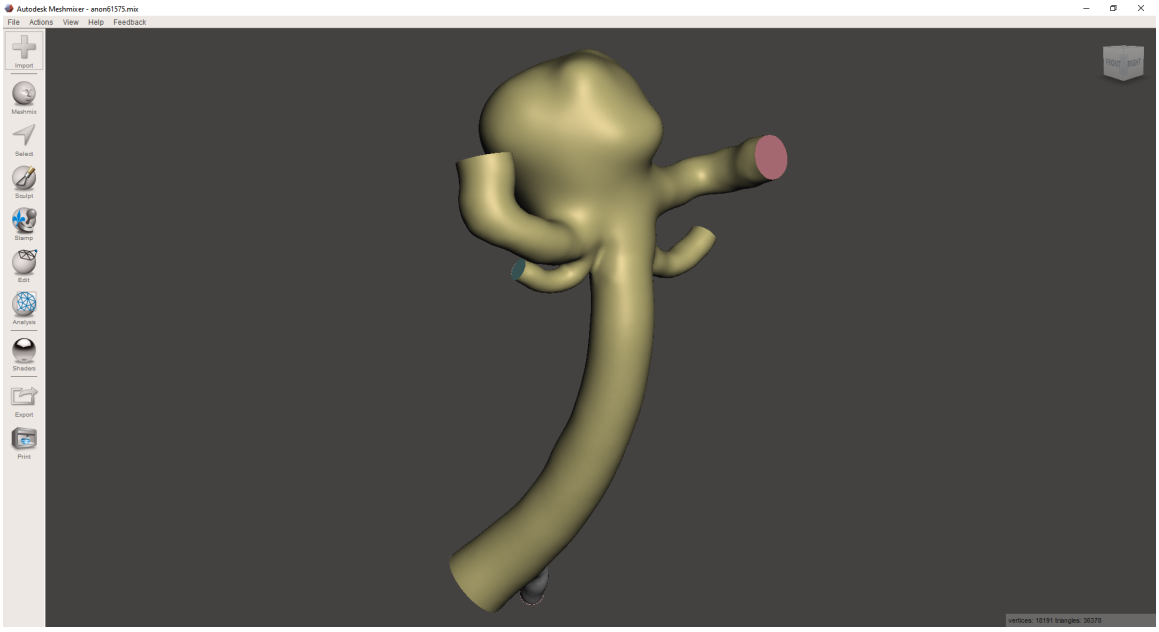

FIG A.5 The finalized geometry in Meshmixer.

Meanwhile, the SMP*f* device is generated by first reconstructing a healthy vessel by removing the aneurysm using Meshmixer's sculpting tools. The reconstructed vessel is then subtracted from the original vessel by selecting both geometries and choosing **Edit > Boolean Difference**, leaving only the aneurysm space—in other words, the SMP*f*. This process has been shown previously in Fig 4.1.

A.3 Mesh Generation in OpenFOAM

The final steps in the simulation process are performed using OpenFOAM-v2012 (ESI Group, Paris, France) and its various utilities, which are run in a Linux command prompt. Ubuntu 20.04 for Windows (Canonical Ltd, London, United Kingdom) was used in this thesis research. It is important that OpenFOAM-v2012, not OpenFOAM 8 (developed by The OpenFOAM Foundation), is used if these steps are being exactly followed. Although the overlap is significant, small discrepancies between the versions may cause the simulations to fail. However, either software will work with minor alterations.

Multiple input files must be prepared to mesh the geometry and run the simulation, and Appendix B is dedicated to the description of these files. Select files will be mentioned

here, but it is important to note that all the files included in Appendix B are necessary. It is typical to copy an existing OpenFOAM tutorial case for the correct solver to the desired location to ensure file existence and organization.

The first step in beginning the simulation process is to ensure that Linux is running the OpenFOAM environment. For this thesis, an alias called `of2012` was created to enable access to OpenFOAM by simply typing

```
1 of2012
```

in the Linux commandline.

Next, one must navigate to the case directory:

```
2 cd [caseDirectory]
```

Here, `[caseDirectory]`, including the square brackets, is a placeholder for the folder path which must either have no spaces or be enclosed in double quotes. This square bracket convention will be used throughout these appendices when discussing Linux commands to denote file or path names that vary according to the user, but these brackets are not included when typing in the Linux prompt.

The individual STLs are next merged into one master STL file. It is easiest to do so from the directory in which they are located, the `constant/triSurface` folder:

```
3 cd constant/triSurface
```

As an example, suppose four STLs named `[inlet]`, `[wall]`, and `[outlet1]`, and `[outlet2]` are to be combined into the geometry `[volume]`. The files are concatenated by

```
4 cat [inlet].stl [wall].stl [outlet*].stl > [volume].stl
```

The name of `[volume].stl` must match the name of the geometry given in the meshing dictionary, `meshDict` (Section B.3). Moreover, note the use of `*` notation above for file names differing by a character.

One may ask why the original solid geometry was separated in Meshmixer only to be reconstituted in OpenFOAM. The reason is that each face group is now identified by its name within the master STL file, allowing OpenFOAM's meshing utility to automatically assign the correct faces to so-called "patches," which are the geometric entities defining the boundaries (inlets, outlets, and walls) in OpenFOAM.

The geometry is scaled from mm to m to ensure the simulation is run in consistent units:

```
5 surfaceTransformPoints -scale '(0.001 0.001 0.001)' [volume].stl [volume].stl
```

In the current configuration, the file is simply overwritten, but the second filename in the command can differ from the first if both copies are desired. The STLs can also be exported from Meshmixer in meters, rendering the previous step unnecessary. However, changing

the units in Meshmixer can lead to issues when manipulating the geometry, such as when remeshing, so doing so is not recommended.

The geometry has now been prepared for meshing. It is necessary to return to the main directory by twice entering a change-of-directory command, one for each level traveled.

```
6 cd ../..
```

The cfMesh utility is used to mesh the geometry. It requires the prior creation of a `meshDict` file and is called by the command

```
7 cartesianMesh > [meshLog]
```

Note that the `meshLog` file, which instructs OpenFOAM to write the meshing steps to a text file instead of the commandline, is optional. It is broadly recommended that any process is written to a logfile.

The mesh should next be checked against quality criteria using

```
8 checkMesh > [checkLog]
```

which gives mesh statistics, such as the number of hexahedra, the minimum and maximum cell volumes, and, most crucially, the mesh nonorthogonality. Cells with a nonorthogonality greater than 70 °C will cause simulation failure, often manifested as oscillatory behavior in the velocity field after a few hundred time steps; they must be strictly avoided. If it does arise, the issue can often be fixed by slightly altering the base cell size.

Visually checking the mesh is also recommended. The meshed geometry can be accessed by typing the command

```
9 touch [sim].foam
```

This creates a FOAM file in the main directory that allows ParaView to display results. The same file will be opened to view the fields following simulation completion, but at this point in the process, only the geometry is displayed. The mesh interior is viewed by applying the **Extract Cells By Region** filter in ParaView and changing the representation to "Surface With Edges" (Fig A.6).

Next, for simulations incorporating the SMP*f* device, a set of cells containing porous material must be specified via

```
10 topoSet > [topoLog]
```

which, like `cartesianMesh`, requires a dictionary, `topoSetDict`. Even for simulations without the SMP*f*, it is helpful to generate this set of cells, since it represents all the cells within the aneurysm space.

The simulation could now be run, but it is advisable to carry out simulations in parallel for large cases. The final step is thus to decompose the mesh domain.

```
11 decomposePar > [deLog]
```

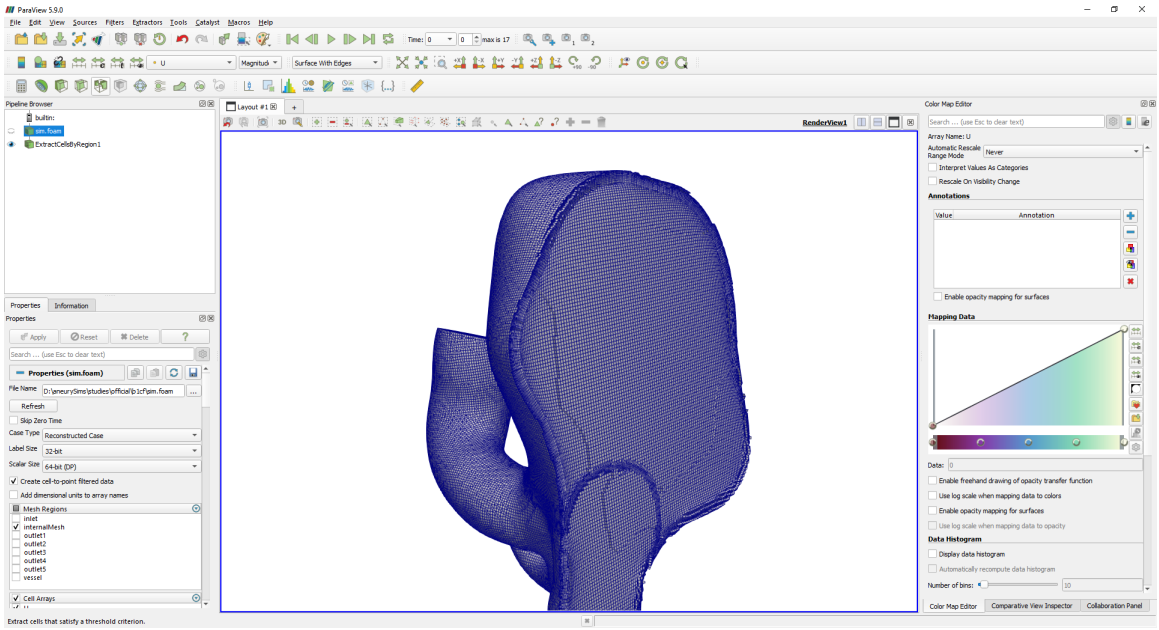

FIG A.6 Performing a visual mesh check in Paraview. The interior of the mesh should be a regular grid of rectangular prisms.

A.4 Simulations in OpenFOAM

Once the setup is complete, the simulation is carried out by calling the appropriate solver, or application, e.g. **simpleFoam** for steady-state flow:

```
12 simpleFoam > [log] &
```

For parallel simulations, the command is

```
13 mpirun -np [N] simpleFoam -parallel > [log] &
```

where `[N]` is the number of processors specified in `decomposeParDict`. The `-parallel` flag is critical; if forgotten, the computer will run `[N]` copies of the same simulation simultaneously. Meanwhile, the ampersand, `&`, moves the current task to the background so the terminal can be accessed while the simulation runs. Keeping the terminal open is recommended for any process that will take some time to complete. In fact, doing so is necessary to plot the residuals:

```
14 gnuplot "[resPlot]" &
```

Here, `[resPlot]` is a script file, outlined in Section B.4, that extracts values from the simulation log and gives real-time plotting instructions to a separate open-source software, gnuplot (Fig A.7). An X server is required for viewing on Windows.

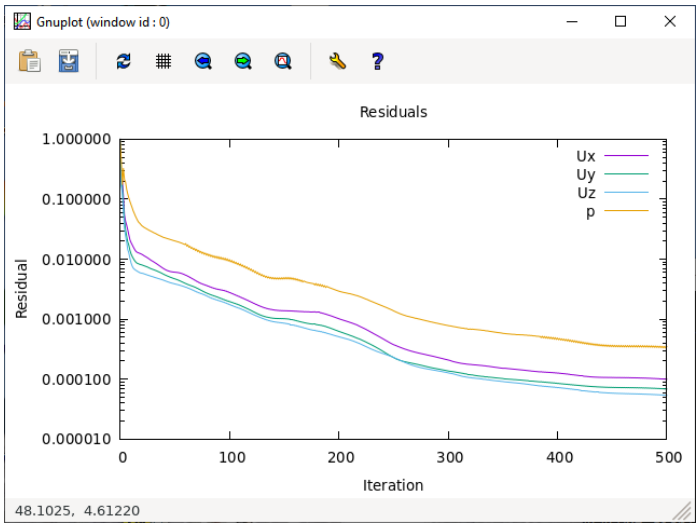

FIG A.7 Plotting residuals in gnuplot for a steady-state case. A convergent case will smoothly trend downward for all fields.

A.5 Post-Processing in OpenFOAM, Paraview, and MATLAB

Once the simulation has finished running, the case must first be reconstructed from the smaller decomposed domains to allow Paraview to read the files.

```
15 reconstructPar > [reLog]
```

The WSS can now be calculated using

```
16 simpleFoam -postProcess -func wallShearStress > [wssLog]
```

Note that `simpleFoam` is replaced by the application used for the particular simulation (see Appendix B for the applications utilized in this thesis). Meanwhile, the fields only inside the SMP*f* device or aneurysm space can be written to a smaller VTM file (.vtm) with

```
17 foamToVTK -cellZone [porousCells] > [vtkLog]
```

Here, `[porousCells]` is the name of the `cellZone` defined in `topoSetDict`.

The results can now be accessed in Paraview by opening the FOAM file to see the entire domain (Fig A.8a), or by opening the VTM file for the `cellZone` (Fig A.8b). Any fields included in the simulation can be displayed at any time point for which files were written, allowing screenshots to be taken. Filters such as the **Stream Tracer** filter can be applied for different visualizations, and other post-processing can be performed. For instance, the temperature profile for transient heat transfer cases can be calculated in Paraview using the **Plot Data Over Time** filter.

Paraview is exceptional at visualization, but lacks some post-processing capabilities. Because of this, it is often beneficial to output the data into a CSV file (.csv) that can be read by Excel or MATLAB. It is typically useful to know the cell volumes when the data

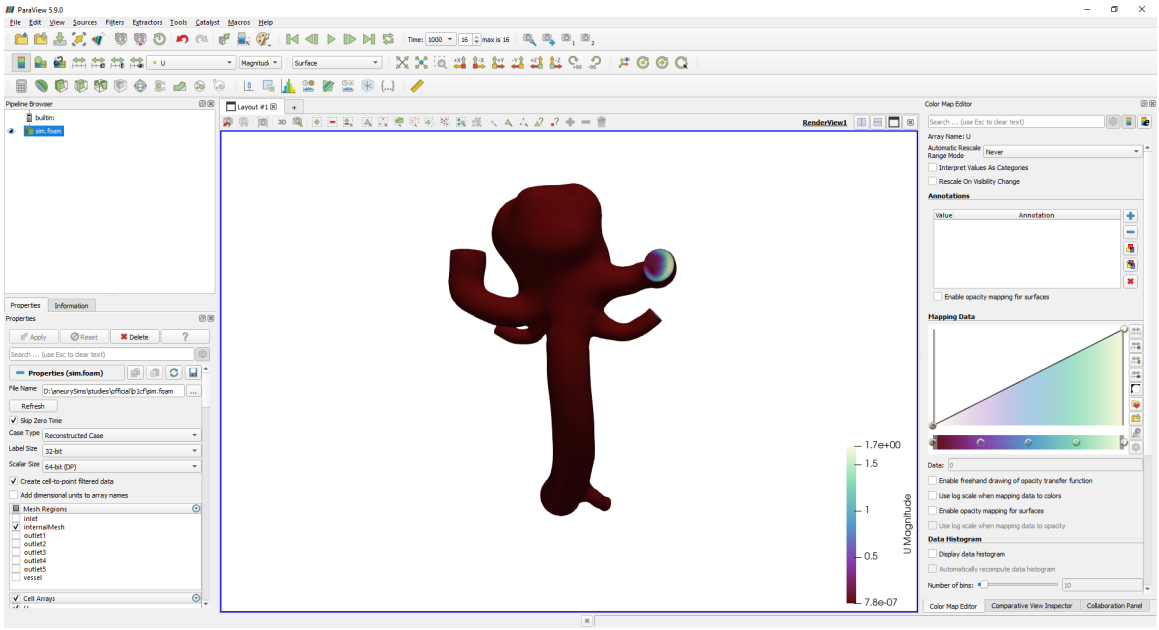

(a)

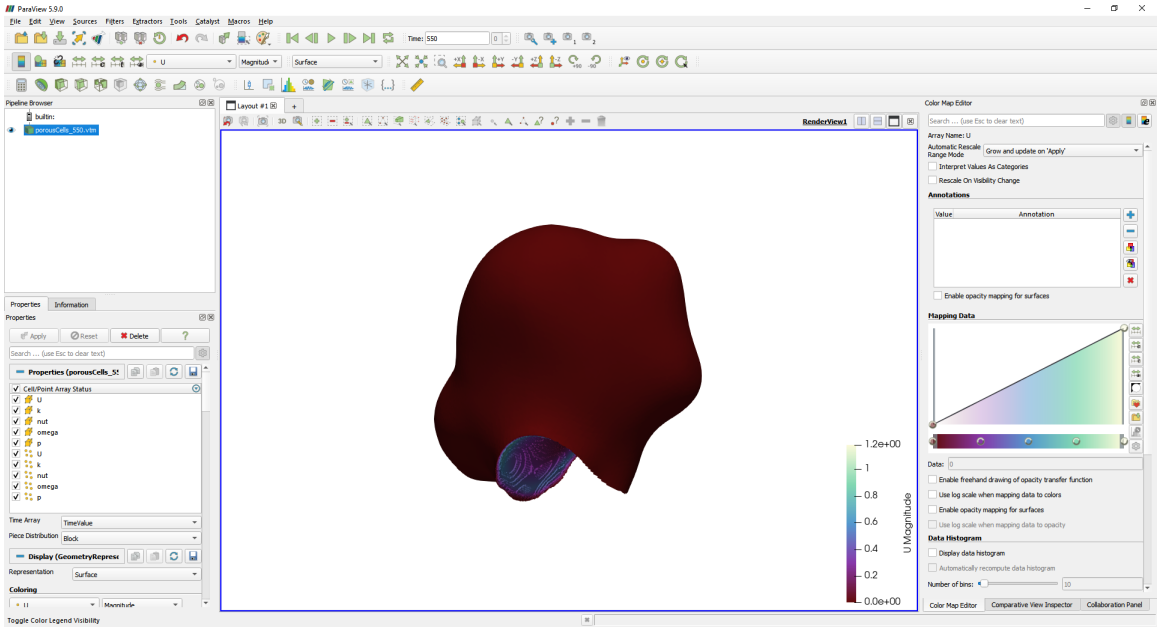

(b)

FIG A.8 Visualizing fields in Paraview. (a) Velocity throughout the entire computational domain at time step 1000, accessed by opening the FOAM file. (b) Velocity throughout only the aneurysm space at time step 550, accessed by opening the VTK file for that time point.

is output, so the first step is to apply the **Cell Size** filter with only the "Compute Volume" checkbox ticked. Next, the **Integrate Variables** filter is applied to create a spreadsheet view. In the spreadsheet view, the Showing field is changed to "CellSize1" and the Attribute field is changed to "Cell Data." These steps display all the data at each cell's centroid, including the velocity, temperature, and cell volume, in row/column format. The data can now be exported to a CSV file by clicking the **Export Spreadsheet** icon (a folder with an arrow entering it) at the far right of the spreadsheet view.

Outputting the data in this way allows it to be manipulated by MATLAB, opening up many powerful avenues for post-processing. For instance, in this thesis, aneurysmal velocity metrics were calculated in MATLAB. The script given below finds the maximum and average velocities in the aneurysm dome for a CSV file included in the folder `[resultsDirectory]`. Briefly, it reads in the file and selects the columns corresponding to the velocity magnitude and cell volume for each cell, putting these lists (or vectors) into a struct. It then calculates the average velocity in the domain as

$$u_{\text{avg}} = \frac{\sum_{i=1}^{n} |u|_i V_i}{\sum_{i=1}^{n} V_i} \tag{A.1}$$

where i is the number of an individual cell, n is the total number of cells, $|u|_i$ is the velocity magnitude for the ith cell, and V_i is the volume of the ith cell. The script also weights each cell's velocity magnitude according to its volume, allowing a histogram that representing the velocity distribution throughout the spatial domain to be calculated.

```
folid = 'resultsDirectory\';
fid = dir(folid);
fid(1:2,:)=[];

tab = readtable(strcat(folid,fid.name));
tab(~ismember(tab.BlockName,'internal'),:) = [];
sim.U = table2array(tab(:,7));
sim.vol = abs(table2array(tab(:,8)));
sim.Uavg = sim.U'*sim.vol/sum(sim.vol);
sim.volmin = min(sim.vol);
sim.numvolnorm = round(sim.vol/sim.volmin);
sim.Umin = min(sim.U);
sim.Umax = max(sim.U);
sim.count = numel(sim.U);

nbins = round(sqrt(min(vertcat(sim.count))));
bins = linspace(min(vertcat(sim.Umin)),max(vertcat(sim.Umax)),nbins);

sim.Uinterp = interp1(bins,bins,sim.U,'nearest');
for j = 1:numel(bins)
    idx = (sim.Uinterp==bins(j));
    sim.binheight(j) = sum(sim.numvolnorm(idx));
end
```

B OPENFOAM INPUT FILES

OpenFOAM simulations utilize extensionless text files to store data, initial and boundary conditions, the mesh, and solver settings. In OpenFOAM-v2012, these files must be organized into the directory tree given in Fig B.1, shown on the next page.

The `0` folder houses the boundary and initial conditions for the simulation—that is, the initialized fields for any relevant scalar or vector quantities, such as the pressure or velocity throughout the domain. Meanwhile, the model geometry and material constants are stored in `constant`, and solver settings are kept in `system`.

The particular files necessary for a simulation depend on the problem and solver type. Three different solvers (or applications) are used in this thesis: **simpleFoam** for the steady-state untreated and treated cases, **buoyantBoussinesqSimpleFoam** for steady-state heat transfer, and **buoyantBoussinesqPimpleFoam** for transient heat transfer. It is common practice to simply create a copy of an OpenFOAM tutorial case for the correct solver, which ensures all the files exist and are in the proper location. The default files can then be edited in a text editor (word processors may introduce formatting that will corrupt the files and so should be avoided).

This appendix includes the input files for a representative transient heat transfer case (in particular, the 40 °C case outlined in Section 5.3) and gives a brief commentary on relevant details. In-depth descriptions of anything contained in the files can be found on the OpenFOAM website[140] or in a plethora of forums. Be careful to note that OpenFOAM-v2012 is the software used in this thesis. Although the overlap is significant, there are small discrepancies between this version and OpenFOAM 8, the toolbox developed by The OpenFOAM Foundation, that will likely cause simulations to fail.

Each file is given its own subheading in the following sections. The files are shown in their entirety except for the default OpenFOAM header and sections breaks, which are removed from all files after the first one to save space. They are written in C++.

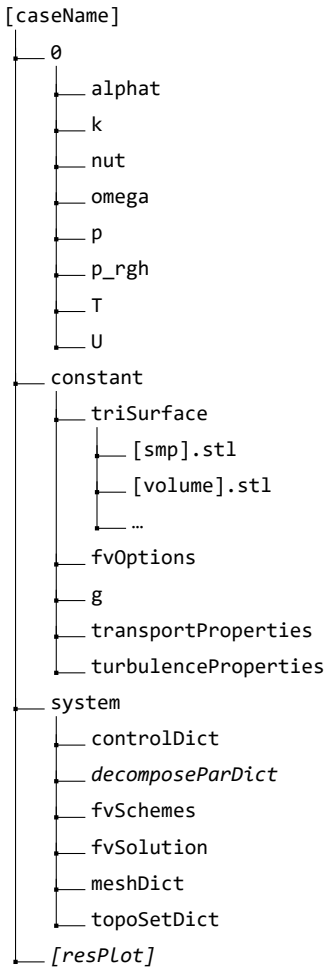

FIG B.1 Initial OpenFOAM case directory. Italicized files are not strictly required to run the simulations, but are highly recommended. Names in square brackets are placeholders, i.e. these folders or files can be renamed.

B.1 Initial & Boundary Conditions (0 Subdirectory)

Each file in the `0` subdirectory initializes a field throughout the entire computational domain and also provides boundary conditions at the surfaces. In OpenFOAM, each boundary surface is assigned to its own group of faces, referred to as a "patch." For asymmetrical, 3D geometries, the two primary patch types are "patch" (used for boundaries through which fluid flows, e.g. inlets and outlets) and "wall" (used for solid boundaries, e.g. the vessel wall). The representative case given in this appendix consists of 4 patches: patch `inlet`, wall `vessel`, patch `outlet1`, and patch `outlet2`.

Unlike many other CFD codes, OpenFOAM forces the use of consistent units (the SI system is the default), and one of the first entries in each field is a dimension line:

```
dimensions [0 2 -2 0 0 0 0];
```

These entries correspond to the seven base units in the SI system. Their order in OpenFOAM is (1) mass, (2) length, (3) time, (4) temperature, (5) quantity, (6) current, and (7) luminous intensity. Boundary conditions must be properly defined in terms of these units or the simulation results will not be sensible.

alphat

Simulation Type Heat transfer.

Description Turbulent thermal diffusivity. Default values can be used for all entries.

```
/*--------------------------------*- C++ -*----------------------------------*\
| =========                 |                                                 |
| \\      /  F ield         | OpenFOAM: The Open Source CFD Toolbox           |
|  \\    /   O peration     | Version:  v2012                                 |
|   \\  /    A nd           | Website:  www.openfoam.com                      |
|    \\/     M anipulation  |                                                 |
\*---------------------------------------------------------------------------*/
FoamFile
{
    version     2.0;
    format      ascii;
    class       volScalarField;
    location    "0";
    object      alphat;
}
// * * * * * * * * * * * * * * * * * * * * * * * * * * * * * * * * * * * * //

dimensions      [0 2 -1 0 0 0 0];

internalField   uniform 0;

boundaryField
{
    inlet
```

```
    {
      type            calculated;
      value           $internalField;
    }

    vessel
    {
      type            alphatJayatillekeWallFunction;
      Prt             0.85;
      value           $internalField;
    }

    "outlet.*"
    {
      type            calculated;
      value           $internalField;
    }
}

// ************************************************************************* //
```

k

Simulation Type All.

Description Turbulent kinetic energy. The inlet value is calculated using Eqn 3.2 and is also assigned to the `internalField`, since initializing the domain to 0 could lead to errors for this particular field.

```
FoamFile
{
    version     2.0;
    format      ascii;
    class       volScalarField;
    location    "0";
    object      k;
}

dimensions      [0 2 -2 0 0 0 0];

internalField   uniform 6.29e-4;

boundaryField
{
    inlet
    {
      type            fixedValue;
      value           $internalField;
    }

    vessel
    {
      type            kLowReWallFunction;
```

```
      value           $internalField;
    }

    "outlet.*"
    {
      type            inletOutlet;
      inletValue      $internalField;
      value           $internalField;
    }
}
```

nut

Simulation Type All.

Description Turbulent kinematic viscosity. Default values can be used for all entries.

```
FoamFile
{
    version     2.0;
    format      ascii;
    class       volScalarField;
    location    "0";
    object      nut;
}

dimensions      [0 2 -1 0 0 0 0];

internalField   uniform 0;

boundaryField
{
    inlet
    {
      type            calculated;
      value           uniform 0;
    }

    vessel
    {
      type            nutUSpaldingWallFunction;
      value           uniform 0;
    }

    "outlet.*"
    {
      type            calculated;
      value           uniform 0;
    }
}
```

omega

Simulation Type All.

Description Turbulent dissipation rate. The inlet value is calculated using Eqn 3.3.

```
FoamFile
{
    version     2.0;
    format      ascii;
    class       volScalarField;
    location    "0";
    object      omega;
}

dimensions      [0 0 -1 0 0 0 0];

internalField   uniform 126;

boundaryField
{
    inlet
    {
      type            fixedValue;
      value           $internalField;
    }

    vessel
    {
      type            omegaWallFunction;
      value           $internalField;
    }

    "outlet.*"
    {
      type            inletOutlet;
      inletValue      $internalField;
      value           $internalField;
    }
}
```

p

Simulation Type All.

Description Pressure. As described in Section 3.3, one outlet is set to 0.

```
FoamFile
{
    version     2.0;
    format      ascii;
    class       volScalarField;
    location    "0";
    object      p;
}
```

```
9
10 dimensions      [0 2 -2 0 0 0 0];
11
12 internalField   uniform 0;
13
14 boundaryField
15 {
16     inlet
17     {
18       type            outletInlet;
19       outletValue     $internalField;
20       value           $internalField;
21     }
22
23     vessel
24     {
25       type            zeroGradient;
26     }
27
28     outlet1
29     {
30       type            inletOutlet;
31       inletValue      $internalField;
32       value           $internalField;
33     }
34
35     outlet2
36     {
37       type            fixedValue;
38       value           uniform 0;
39     }
40 }
```

p_rgh

Simulation Type Heat transfer.

Description Pressure with the hydrostatic pressure contribution removed. Required for applications where buoyancy or compressibility are considered, and used in place of the usual pressure file in such cases. The setup is identical to that of the usual pressure file, except `zeroGradient` is replaced with `fixedFluxPressure`, which corrects for body forces.

```
1 FoamFile
2 {
3     version     2.0;
4     format      ascii;
5     class       volScalarField;
6     location    "0";
7     object      p_rgh;
8 }
9
10 dimensions      [0 2 -2 0 0 0 0];
11
```

```
internalField   uniform 0;

boundaryField
{
    inlet
    {
      type            outletInlet;
      outletValue     $internalField;
      value           $internalField;
    }

    vessel
    {
      type            fixedFluxPressure;
    }

    outlet1
    {
      type            inletOutlet;
      inletValue      $internalField;
      value           $internalField;
    }

    outlet2
    {
      type            fixedValue;
      value           uniform 0;
    }
}
```

T

Simulation Type Heat transfer.

Description Temperature. Note that the units are K, not °C.

```
FoamFile
{
    version     2.0;
    format      ascii;
    class       volScalarField;
    location    "0";
    object      T;
}

dimensions      [0 0 0 1 0 0 0];

internalField   uniform 310;

boundaryField
{
    inlet
    {
      type            fixedValue;
```

```
      value           $internalField;
    }

    vessel
    {
       type           zeroGradient;
    }

    "outlet.*"
    {
      type            inletOutlet;
      value           $internalField;
      inletValue      $internalField;
    }
}
```

U

Simulation Type All.

Description Velocity. Note that the `volumetricFlowRate` conditions do not prescribe a velocity profile, but scale the calculated velocity magnitudes to provide the desired volumetric flow rate through the patch.

```
FoamFile
{
    version     2.0;
    format      ascii;
    class       volVectorField;
    location    "0";
    object      U;
}

dimensions      [0 1 -1 0 0 0 0];

internalField   uniform (0 0 0);

boundaryField
{
    inlet
    {
      type               flowRateInletVelocity;
      volumetricFlowRate  1.66e-6;
      value              $internalField;
    }

    vessel
    {
        type             noSlip;
        valu             $internalField;
    }

    outlet1
```

```
    {
      type                flowRateOutletVelocity;
      volumetricFlowRate  8.56e-7;
      value               $internalField;
    }

    outlet2
    {
      type                inletOutlet;
      inletValue          $internalField;
      value               $internalField;
    }
}
```

B.2 Mesh & Material Properties (Constant Subdirectory)

The `constant` subdirectory contains the files that determine the physical properties of the simulation: the fluid and porous media parameters, body forces, STL files defining the geometry, and, after mesh generation, the mesh itself. (It is stored as a series of text files specifying face locations, cell numbers, boundaries, etc. in the newly created `polyMesh` subdirectory inside `constant`.)

fvOptions

Simulation Type Porous flow and heat transfer.

Description Provides the Darcy–Forchheimer coefficients and anisotropic orientation to the porous region, as well as a time-varying heat source to the device for heat transfer simulations.

```
FoamFile
{
    version     2.0;
    format      ascii;
    class       dictionary;
    location    "constant";
    object      fvOptions;
}

porosity
{
    type            explicitPorositySource;

    explicitPorositySourceCoeffs
    {
      type            DarcyForchheimer;
      selectionMode   cellZone;
      cellZone        porousCells;

```

```
      D 1.75e8;
      F 1.45e4;

      d   ($D $D $D);
      f   ($F $F $F);

      coordinateSystem
      {
          type    cartesian;
          origin  (0 0 0);
          coordinateRotation
          {
              type    axesRotation;
              e1      (1 0 0);
              e2      (0 1 0);
          }
      }
    }
}

temp
{
    type            scalarFixedValueConstraint;

    timeStart       0;
    duration        3;
    selectionMode   cellZone;
    cellZone        porousCells;

    fieldValues
    {
      T 313;
    }
}
```

g

Simulation Type Heat transfer.

Description Includes the gravity/body force field in terms of the world coordinates. Although the file is required, the gravity field can be set to zero for the studies in this thesis, since buoyancy effects are minimal.

```
FoamFile
{
    version     2.0;
    format      ascii;
    class       uniformDimensionedVectorField;
    location    "constant";
    object      g;
}

dimensions      [0 1 -2 0 0 0 0];
```

```
11
12 value           (0 0 0);
```

transportProperties

Simulation Type All.

Description Gives fluid properties. Only the kinematic viscosity is required for simple flow simulations, while the others are necessary for solving the heat equation.

```
1  FoamFile
2  {
3      version     2.0;
4      format      ascii;
5      class       dictionary;
6      object      transportProperties;
7  }
8
9  transportModel Newtonian;
10
11 nu              3.5e-06;
12 beta            2e-04;
13 TRef            293;
14 Pr              25.4;
15 Prt             0.85;
```

turbulenceProperties

Simulation Type All.

Description Specifies the turbulence model used in the simulation.

```
1  FoamFile
2  {
3      version     2.0;
4      format      ascii;
5      class       dictionary;
6      location    "constant";
7      object      turbulenceProperties;
8  }
9
10 simulationType RAS;
11
12 RAS
13 {
14     RASModel        kOmegaSST;
15     turbulence      on;
16     printCoeffs     on;
17 }
```

B.3 Solver & Utility Dictionaries (System Subdirectory)

Finally, the files in the `system` subdirectory provide the instructions necessary for OpenFOAM to build and solve the case. The dictionaries involved with building the case—creating the mesh, assigning cells to the porous region, and decomposing the mesh for parallel processing—do not typically require alteration between the different applications, since these processes are the same whether the simulation is steady-state or pulsatile, for instance. That is not true for the `controlDict`, `fvSchemes`, and `fvSolution` dictionaries. In general, these dictionaries should be taken from a tutorial case for the correct application (**simpleFoam**, **buoyantBoussinesqSimpleFoam**, or **buoyantBoussinesqPimpleFoam**) and used with minimal changes.

controlDict

Simulation Type All.

Description Specifies general simulation controls, such as simulation time and write properties. The `application`, `endTime`, `deltaT`, and `writeInterval` will vary between different cases.

```
FoamFile
{
    version     2.0;
    format      ascii;
    class       dictionary;
    location    "system";
    object      controlDict;
}

application     buoyantBoussinesqPimpleFoam;

startFrom       startTime;
startTime       0;
stopAt          endTime;
endTime         5;
deltaT          .001;

writeControl    timeStep;
writeInterval   100;
purgeWrite      0;
writeFormat     ascii;
writePrecision  6;
writeCompression off;

timeFormat      general;
timePrecision   6;

runTimeModifiable true;
```

decomposeParDict

Simulation Type All.

Description Decomposes the mesh into separate regions for parallel processing.

```
FoamFile
{
    version     2.0;
    format      ascii;
    class       dictionary;
    location    "system";
    object      decomposeParDict;
}

numberOfSubdomains 6;

method              scotch;

scotchCoeffs
{
  processorWeights (1 1 1 1 1 1);
}
```

fvSchemes

Simulation Type All.

Description Provides the numerical schemes for terms such as the gradient and Laplacian. The default values for a particular application should be used unless the user is experienced.

```
FoamFile
{
    version     2.0;
    format      ascii;
    class       dictionary;
    location    "system";
    object      fvSchemes;
}

ddtSchemes
{
    default         Euler;
}

gradSchemes
{
    default         Gauss linear;
}

divSchemes
{
    default                         bounded Gauss linearUpwind grad;
```

```
    div((nuEff*dev2(T(grad(U))))) Gauss linear;
}

laplacianSchemes
{
    default         Gauss linear corrected;
}

interpolationSchemes
{
    default         linear;
}

snGradSchemes
{
    default         corrected;
}

wallDist
{
    method meshWave;
    correctWalls true;
}
```

fvSolution

Simulation Type All.

Description Defines numerical solvers and tolerances. The default values for a particular application should be used for the `solvers` entries, although it may be necessary to include a missing field, e.g. to exchange `epsilon` for `omega`. The `residualControl`, which will stop the solution if the residuals fall below a certain value, can be safely altered. Changing the `relaxationFactors` can lead to faster convergence but can also cause solution divergence, so caution should be exercised with these entries.

```
FoamFile
{
    version     2.0;
    format      ascii;
    class       dictionary;
    location    "system";
    object      fvSolution;
}

solvers
{
    "(p|p_rgh)"
    {
        solver          GAMG;
        tolerance       1e-12;
        relTol          0.1;
        smoother        GaussSeidel;
```

```
    }

    "(p|p_rgh)Final"
    {
        $p;
        relTol          0;
    }

    "(U|T|k|omega|R)"
    {
        solver          PBiCGStab;
        preconditioner  DILU;
        tolerance       1e-12;
        relTol          0.1;
    }

    "(U|T|k|omega|R)Final"
    {
        $U;
        relTol          0;
    }
}

PIMPLE
{
    nNonOrthogonalCorrectors 0;
    nCorrectors              1;
    nOuterCorrectors         50;
    residualControl
    {
      U
      {
        tolerance  1e-5;
        relTol     0;
      }
      p
      {
        tolerance  5e-4;
        relTol     0;
      }
    }

    pRefCell       0;
    pRefValue      0;
}

relaxationFactors
{
    fields
    {
      p_rgh        0.5;
      p            0.5;
    }
    equations
```

```
    {
        ".*"        0.7;
    }
}
```

meshDict

Simulation Type All.

Description Provides meshing instructions to the cfMesh utility. Meshing is simple from a user standpoint, but requires the proper setup to work. For this case, the entire computational domain must be enclosed within an STL file named `volume` that is located in the `constant/triSurface` subdirectory and uses m as the length unit. Moreover, this STL file should be composed of 4 concatenated STL files named `inlet`, `vessel`, `outlet1`, and `outlet2`. The names of these individual solids can be edited within the concatenated file in a text editor if needed.

```
FoamFile
{
    version   2.0;
    format    ascii;
    class     dictionary;
    location  "system";
    object    meshDict;
}

surfaceFile "constant/triSurface/volume.stl";
maxCellSize 2e-4;

boundaryLayers
{
    patchBoundaryLayers
    {
        "vessel"
        {
            nLayers             4;
            thicknessRatio      1.1;
            allowDiscontinuity  1;
        }
    }
}

renameBoundary
{
    defaultName vessel;
    defaultType wall;

    newPatchNames
    {
        "inlet"
        {
```

```
            type    patch;
            newName inlet;
        }

        "outlet1"
        {
            type    patch;
            newName outlet1;
        }

        "outlet2"
        {
            type    patch;
            newName outlet2;
        }
    }
}
```

topoSetDict

Simulation Type Porous flow.

Description Assigns all cells contained within a region, e.g. the volume bounded by the SMP*f* device, to a `cellZone`, allowing the porous material to be modeled within the computational domain. The name of the `cellZone`, `porousCells` in this case, is referenced by other files.

```
FoamFile
{
    version     2.0;
    format      ascii;
    class       dictionary;
    object      topoSetDict;
}

actions
(
  {
  name    porousCellsSet;
  type    cellSet;
  action   new;
  source   surfaceToCell;
  sourceInfo
  {
      file "constant/triSurface/smp.stl";
      outsidePoints         ((-0.011037 -0.004037 0.014037));
      includeCut            true;
      includeInside         true;
      includeOutside        false;
      nearDistance          -1;
      curvature             -100;
      useSurfaceOrientation false;
  }
```

```
 }

 {
  name    porousCells;
  type    cellZoneSet;
  action  new;
  source  setToCellZone;
  sourceInfo
  {
   set    porousCellsSet;
  }
 }
);
```

B.4 Residual Plotting

Monitoring the residual values during a simulation is vital for ensuring its convergence. There are multiple ways to plot field residuals in OpenFOAM. One simple method is given here.

[resPlot]

Simulation Type All.

Description Gives instructions to gnuplot, an open-source plotting software. The file assumes the simulation results are sent to a logfile titled `log`, leveraging the standard OpenFOAM log format to rip out field residual data as described in Section A.4.

```
set logscale y
set title "Residuals"
set ylabel 'Residual'
set xlabel 'Iteration'
plot "< cat log | grep 'Solving for Ux' | cut -d' ' -f9 | tr -d ',' title 'Ux' with lines
    ,\
"< cat log | grep 'Solving for Uy' | cut -d' ' -f9 | tr -d ',' title 'Uy' with lines,\
"< cat log | grep 'Solving for Uz' | cut -d' ' -f9 | tr -d ',' title 'Uz' with lines,\
"< cat log | grep 'Solving for T' | cut -d' ' -f9 | tr -d ',' title 'T' with lines,\
"< cat log | grep 'Solving for p_rgh' | cut -d' ' -f9 | tr -d ',' title 'p_{rgh}' with
    lines
pause 1
reread
```

REFERENCES

[1] G. Yong-Zhong, H. August, and M. van Alphen, "Pathogenesis and histopathology of saccular aneurysms: review of the literature," *Neurological Research*, vol. 12, no. 4, pp. 249–55, 1990 (cit. on p. 3).

[2] D. O. Wiebers and International Study of Unruptured Intracranial Aneurysms Investigators, "Unruptured intracranial aneurysms: natural history, clinical outcome, and risks of surgical and endovascular treatment," *Lancet*, vol. 362, pp. 103–10, 2003 (cit. on pp. 4, 9, 10).

[3] M. H. M. Vlak, A. Algra, R. Brandenburg, and G. J. E. Rinkel, "Prevalence of unruptured intracranial aneurysms, with emphasis on sex, age, comorbidity, country, and time period: a systematic review and meta-analysis," *Lancet Neurology*, vol. 10, pp. 626–36, 2011 (cit. on pp. 4–6).

[4] J. Zhao, H. Lin, R. Summers, M. Yang, B. G. Cousins, *et al.*, "Current treatment strategies for intracranial aneurysms: an overview," *Angiology*, vol. 69, no. 1, pp. 17–30, 2018 (cit. on p. 4).

[5] NIH, *Saccular and fusiform aneurysms*, `https://openi.nlm.nih.gov/imgs/512/267/3563954/PMC3563954_40258_2012_5_Fig1_HTML.png`, adapted (cit. on p. 4).

[6] L. Zarrinkoob, K. Ambarki, A. Wåhlin, R. Birgander, A. Eklund, *et al.*, "Blood flow distribution in cerebral arteries," *Journal of Cerebral Blood Flow and Metabolism*, vol. 35, pp. 648–54, 2015 (cit. on p. 4).

[7] MedlinePlus, *Circle of Willis*, `https://medlineplus.gov/ency/images/ency/fullsize/18009.jpg`, adapted (cit. on p. 5).

[8] M. W. Vernooij, M. A. Ikram, H. L. Tanghe, A. J. Vincent, A. Hofman, *et al.*, "Incidental findings on brain MRI in the general population," *New England Journal of Medicine*, vol. 357, pp. 1821–28, 2007 (cit. on p. 4).

[9] R. Al-Shahi, P. M. White, R. J. Davenport, and K. W. Lindsay, "Subarachnoid haemorrhage," *British Medical Journal*, vol. 333, pp. 235–40, 2006 (cit. on pp. 5, 9).

[10] A. A. le Roux and M. C. Wallace, "Outcome and cost of subarachnoid hemorrhage," *Neurosurgery Clinics of North America*, vol. 21, no. 2, pp. 235–46, 2010 (cit. on p. 5).

[11] A. Hijdra, R. Braakman, J. van Gijn, M. Vermeulen, and H. van Crevel, "Aneurysmal subarachnoid hemorrhage: complications and outcome in a hospital population," *Stroke*, vol. 18, pp. 1061–67, 1987 (cit. on p. 5).

[12] J. van Gijn, R. S. Kerr, and G. J. Rinkel, "Subarachnoid haemorrhage," *Lancet*, vol. 369, pp. 306–18, 2007 (cit. on p. 5).

[13] F. Linn, G. Rinkel, A. Algra, and J. van Gijn, "Incidence of subarachnoid hemorrhage–role of region, year, and rate of computed tomography: a meta-analysis," *Stroke*, vol. 27, no. 4, pp. 625–29, 1996 (cit. on p. 5).

[14] T. Krings, S. Geibprasert, and K. G. terBrugge, "Pathomechanisms and treatment of pediatric aneurysms," *Child's Nervous System*, vol. 26, pp. 1309–18, 2010 (cit. on p. 5).

[15] N. Etminan and G. J. Rinkel, "Unruptured intracranial aneurysms: development, rupture, and preventative management," *Nature Reviews Neurology*, vol. 12, pp. 699–713, 2016 (cit. on pp. 6, 7).

[16] M. H. Vlak, G. J. Rinkel, P. Greebe, and A. Algra, "Independent risk factors for intracranial aneurysms and their joint effect: a case-control study," *Stroke*, vol. 44, no. 4, pp. 984–87, 2013 (cit. on p. 6).

[17] B. Weir, C. Amidei, G. Kongable, J. M. Findlay, N. F. Kassell, *et al.*, "The aspect ratio (dome/ neck) of ruptured and unruptured aneurysms," *Journal of Neurosurgery*, vol. 99, pp. 447–51, 2003 (cit. on p. 6).

[18] H. Meng, V. M. Tutino, J. Xiang, and A. Siddiqui, "High WSS or low WSS? Complex interactions of hemodynamics with intracranial aneurysm initiation, growth, and rupture: toward a unifying hypothesis," *American Journal of Neuroradiology*, vol. 35, no. 7, pp. 1254–62, 2014 (cit. on pp. 6, 7).

[19] H. M. Finlay, P. Whittaker, and P. B. Canham, "Collagen organization in the branching region of human brain arteries," *Stroke*, vol. 29, pp. 1595–1601, 1998 (cit. on p. 6).

[20] E. Metaxa, M. Tremmel, S. K. Natarajan, J. Xiang, R. A. Paluch, *et al.*, "Characterization of critical hemodynamics contributing to aneurysmal remodeling at the basilar terminus in a rabbit model," *Stroke*, vol. 41, no. 8, pp. 1774–82, 2010 (cit. on p. 6).

[21] N. Chalouhi, B. L. Hoh, and D. Hasan, "Review of cerebral aneurysm formation, growth, and rupture," *Stroke*, vol. 44, pp. 3613–22, 2013 (cit. on p. 6).

[22] J. Cebral, F. Detmer, B. Chung, J. Choque-Velasquez, B. Rezai, *et al.*, "Local hemodynamic conditions associated with focal changes in the intracranial aneurysm wall," *American Journal of Neuroradiology*, vol. 40, no. 3, pp. 510–16, 2019 (cit. on p. 7).

[23] UCAS Japan Investigators, "The natural course of unruptured cerebral aneurysms in a Japanese cohort," *New England Journal of Medicine*, vol. 366, pp. 2474–82, 2012 (cit. on p. 7).

[24] J. P. Greving, M. J. H. Wermer, R. D. Brown, Jr., A. Morita, S. Juvela, *et al.*, "Development of the PHASES score for prediction of risk of rupture of intracranial aneurysms: a pooled analysis of six prospective cohort studies," *Lancet Neurology*, vol. 13, pp. 59–66, 2014 (cit. on p. 7).

[25] G. J. Rinkel, M. Djibuti, A. Algra, and J. van Gijn, "Prevalence and risk of rupture of intracranial aneurysms: systematic review," *Stroke*, vol. 29, pp. 251–56, 1988 (cit. on p. 7).

[26] W. Brinjikji, Y. Zhu, G. Lanzino, H. Cloft, M. Murad, *et al.*, "Risk factors for growth of intracranial aneurysms: a systematic review and meta-analysis," *American Journal of Neuroradiology*, vol. 37, pp. 615–20, 2016 (cit. on pp. 7, 11).

[27] N. N. Stojanović, A. Kostić, R. Mitić, L. Berilažić, and M. Radisavljević, "Association between Circle of Willis configuration and rupture of cerebral aneurysms," *Medicina*, vol. 55, 2019 (cit. on p. 7).

[28] N. K. de Rooij, B. K. Velthuis, A. Algra, and G. J. E. Rinkel, "Configuration of the circle of Willis, direction of flow, and shape of the aneurysm as risk factors for rupture of intracranial aneurysms," *Journal of Neurology*, vol. 256, 2009 (cit. on p. 7).

[29] T. Satoh, M. Omi, C. Ohsako, A. Katsumata, Y. Yoshimoto, *et al.*, "Influence of perianeurysmal environment on the deformation and bleb formation of the unruptured cerebral aneurysm: assessment with fusion imaging of 3D MR cisternography and 3D MR angiography," *American Journal of Neuroradiology*, vol. 26, no. 8, pp. 2010–18, 2005 (cit. on p. 7).

[30] M. Waqas, F. Chin, H. Rajabzadeh-Oghaz, A. D. Gong, H. H. Rai, *et al.*, "Size of ruptured intracranial aneurysms: a systematic review and meta-analysis," *Acta Neurochirurgica*, vol. 162, pp. 1353–62, 2020 (cit. on p. 7).

[31] M. Rahman, J. Smietana, E. Hauck, B. Hoh, N. Hopkins, *et al.*, "Size ratio correlates with intracranial aneurysm rupture status: a prospective study," *Stroke*, vol. 41, pp. 916–20, 2010 (cit. on p. 7).

[32] R. Astley, "The hemodynamic environment of aortic and cerebral aneurysms: a review," *Cardion and Encephalon*, vol. 1, no. 1, pp. 3–35, 1987 (cit. on p. 8).

[33] T. D. Payner, I. Melamed, S. Ansari, T. J. Leipzig, J. A. Scott, *et al.*, "Trends over time in the management of 2253 patients with cerebral aneurysms: a single practice experience," *Surgical Neurology International*, vol. 2, 2011 (cit. on pp. 8, 10).

[34] L. T. Lai and A. H. O'Neill, "History, evolution, and continuing innovations of intracranial aneurysm surgery," *World Neurosurgery*, vol. 102, pp. 673–81, 2017 (cit. on p. 8).

[35] Mayfield Brain and Spine, *Aneurysm clipping*, `https://dbmmu5j6lxew.cloudfront.net/pe-aneurclipping-figure1.jpg`, adapted (cit. on p. 8).

[36] International Subarachnoid Aneurysm Trial Collaborative Group, "International Subarachnoid Aneurysm Trial (ISAT) of neurosurgical clipping versus endovascular coiling in 2143 patients with ruptured intracranial aneurysms: a randomised trial," *Lancet*, vol. 360, pp. 1267–74, 2002 (cit. on pp. 9, 10).

[37] A. Rodriguez-Hernandez, M. E. Sughrue, S. Akhavan, J. Habdank-Kolaczkowski, and M. T. Lawton, "Current management of middle cerebral artery aneurysms: surgical results with a 'clip first' policy," *Neurosurgery*, vol. 72, no. 3, pp. 415–27, 2013 (cit. on p. 9).

[38] G. K. Wong, H.-B. Tan, M. C. Kwan, R. Y. Ng, S. C. Yu, *et al.*, "Evolution of intracranial aneurysm treatment: from Hunterian ligation to the flow diverter," *Surgical Practice*, vol. 15, pp. 16–20, 2011 (cit. on pp. 9, 11).

[39] G. Guglielmi, F. Viñuela, I. Sepetka, and V. Macellari, "Electrothrombosis of saccular aneurysms via endovascular approach," *Journal of Neurosurgery*, vol. 75, no. 1, pp. 1–7, 1991 (cit. on pp. 9, 10).

[40] Mayfield Brain and Spine, *Aneurysm embolization*, `https://dbmmu5j6lxew.cloudfront.net/pe-aneurcoiling-fig4.jpg` and `https://dbmmu5j6lxew.cloudfront.net/pe-aneurcoiling-fig5.jpg`, adapted (cit. on p. 9).

[41] A. Sadato, M. Hayakawa, K. Adachi, I. Nakahara, and Y. Hirose, "Large residual volume, not low packing density, is the most influential risk factor for recanalization after coil embolization of cerebral aneurysms," *PLoS One*, vol. 11, no. 5, e0155062-1–8, 2016 (cit. on pp. 10, 43, 47).

[42] H. Yuan, W. Yong-Jie, Z. Deng, Q. Wu, and J.-M. Zhang, "Stent-assisted coiling versus coiling in treatment of intracranial aneurysm: a systematic review and meta-analysis," *PLoS One*, vol. 9, no. 1, e82311, 2014 (cit. on p. 10).

[43] J. S. McDonald, R. J. McDonald, J. Fan, D. F. Kallmes, G. Lanzino, *et al.*, "Comparative effectiveness of unruptured cerebral aneurysm therapies: Propensity score analysis of clipping versus coiling," *Stroke*, vol. 44, pp. 988–94, 2013 (cit. on p. 10).

[44] W.-Q. Xin, Q.-Q. Xin, and X.-Y. Yang, "Meta-analysis of clipping versus coiling for the treatment of unruptured middle cerebral artery aneurysms: direct comparison of procedure-related complications," *Neuropsychiatric Disease and Treatment*, vol. 15, pp. 3387–95, 2019 (cit. on p. 10).

[45] R. J. Komotar, J. Mocco, and R. A. Solomon, "Guidelines for the surgical treatment of unruptured intracranial aneurysms: the first annual J. Lawrence Pool Memorial Research Symposium—controversies in the management of cerebral aneurysms," *Neurosurgery*, vol. 62, no. 1, pp. 183–94, 2008 (cit. on p. 10).

[46] W. J. van Rooij and M. Sluzewski, "Endovascular treatment of large and giant aneurysms," *American Journal of Neuroradiology*, vol. 30, no. 1, pp. 12–18, 2009 (cit. on p. 10).

[47] J. Raymond, F. Guilbert, A. Weill, S. A. Georganos, L. Juravsky, *et al.*, "Long-term angiographic recurrences after selective endovascular treatment of aneurysms with detachable coils," *Stroke*, vol. 34, pp. 1398–1403, 2003 (cit. on p. 10).

[48] S.-N. H. Khan, C. Nichols, J. J. DePowell, T. A. Abruzzo, and A. J. Ringer, "Comparison of coil types in aneurysm recurrence," *Clinical Neurology and Neurosurgery*, vol. 114, pp. 12–16, 2012 (cit. on p. 11).

[49] D. Kallmes, R. Hanel, D. Lopes, E. Boccardi, A. Bonafé, *et al.*, "International retrospective study of the Pipeline Embolization Device: A multicenter aneurysm treatment study," *American Journal of Neuroradiology*, vol. 36, pp. 108–15, 2015 (cit. on p. 11).

[50] Y. Wang, C. Yuan, S. Shen, L. Xu, and H. Duan, "Whether intracranial aneurysm could be well treated by flow diversion: a comprehensive meta-analysis of large-sample studies including anterior and posterior circulation," *BioMed Research International*, p. 6 637 780, 2021 (cit. on p. 11).

[51] W. Brinjikji, M. H. Murad, G. L. MPH, H. J. Cloft, and D. F. Kallmes, "Endovascular treatment of intracranial aneurysms with flow diverters," *Stroke*, vol. 44, no. 2, pp. 442–47, 2013 (cit. on p. 11).

[52] M. A. Silva, A. P. See, P. Khandelwal, A. Mahapatra, K. U. Frerichs, *et al.*, "Comparison of flow diversion with clipping and coiling for the treatment of paraclinoid aneurysms in 115 patients," *Journal of Neurosurgery*, vol. 130, pp. 1505–12, 2019 (cit. on p. 11).

[53] Mayfield Brain and Spine, *Flow diversion*, `https://mayfieldclinic.com/images/flow_diverter.jpg`, adapted (cit. on p. 11).

[54] A. Metcalfe, A. C. Desfaits, I. Salazkin, L. Yahia, W. M. Sokolowski, *et al.*, "Cold hibernated elastic memory foams for endovascular interventions," *Biomaterials*, vol. 24, pp. 491–97, 2003 (cit. on p. 11).

[55] J. Hu, "Introduction," in *Shape Memory Polymers and Textiles*. Woodhead Publishing, 2007, ch. 1, pp. 1–27 (cit. on p. 12).

[56] J. N. Rodriguez, F. J. Clubb, T. S. Wilson, M. W. Miller, T. W. Fossum, *et al.*, "In vivo response to an implanted shape memory polyurethane foam in a porcine aneurysm model," *Journal of Biomedical Materials Research*, vol. 102, no. 5, pp. 1231–42, 2014 (cit. on pp. 13, 14).

[57] J. Horn, W. Hwang, S. L. Jessen, B. K. Keller, M. W. Miller, *et al.*, "Comparison of shape memory polymer foam versus bare metal coil treatments in an porcine sidewall aneurysm model," *Journal of Biomedical Materials Research Part B*, vol. 105, no. 7, pp. 1892–1905, 2017 (cit. on pp. 13, 14, 44, 45).

[58] J. Wang, J. Luo, R. Kunkel, M. Saha, B. N. Bohnstedt, *et al.*, "Development of shape memory polymer nanocomposite foam for treatment of intracranial aneurysms," *Materials Letters*, vol. 250, pp. 38–41, 2019 (cit. on p. 13).

[59] P. Singhal, J. N. Rodriguez, W. Small, S. Eagleston, J. V. de Water, *et al.*, "Ultra low density and highly crosslinked biocompatible shape memory polyurethane foams," *Journal of Polymer Science Part B: Polymer Physics*, vol. 50, no. 10, pp. 724–37, 2012 (cit. on p. 13).

[60] A. J. Boyle, T. L. Landsman, M. A. Wierzbicki, L. D. Nash, W. Hwang, *et al.*, "In vitro and in vivo evaluation of a shape memory polymer foam-over-wire embolization device delivered in saccular aneurysm models," *Journal of Biomedical Materials Research Part B: Applied Biomaterials*, vol. 104, no. 7, pp. 1407–15, 2016 (cit. on p. 13).

[61] W. Hwang, B. L. Volk, F. Akberali, P. Singhal, J. C. Criscione, *et al.*, "Estimation of aneurysm wall stresses created by treatment with a shape memory polymer foam device," *Biomechanics and Modeling in Mechanobiology*, vol. 11, pp. 715–29, 2012 (cit. on pp. 13, 58).

[62] K. R. Jones, "On the differential form of Darcy's law," *Journal of Geophysical Research*, vol. 67, no. 2, pp. 731–32, 1962 (cit. on p. 16).

[63] A. D. Muschenborn, J. M. Ortega, J. M. Szafron, D. J. Szafron, and D. J. Maitland, "Porous media properties of reticulated shape memory polymer foams and mock embolic coils for aneurysm treatment," *BioMedical Engineering OnLine*, vol. 12, pp. 103-1–13, 2013 (cit. on pp. 16, 24, 37–40, 43, 58).

[64] C. F. Gonzalez, Y. I. Cho, H. V. Ortega, and J. Moret, "Intracranial aneurysms: Flow analysis of their origin and progression," *American Journal of Neurology*, vol. 13, no. 1, pp. 181–88, 1992 (cit. on p. 17).

[65] A. M. Robertson and P. N. Watton, "Computational fluid dynamics in aneurysm research: Critical reflections, future directions," *American Journal of Neurology*, vol. 33, no. 6, pp. 992–95, 2012 (cit. on p. 17).

[66] K. M. Saqr, S. Rashad, S. Tupin, K. Niizuma, T. Hassan, *et al.*, "What does computational fluid dynamics tell us about intracranial aneurysms? A meta-analysis and critical review," *Journal of Cerebral Blood Flow and Metabolism*, vol. 40, no. 5, pp. 1021–39, 2020 (cit. on pp. 17, 21).

[67] P. Berg, S. Saalfeld, S. Voß, O. Beuing, and G. Janiga, "A review on the reliability of hemodynamic modeling in intracranial aneurysms: why computational fluid dynamics alone cannot solve the equation," *Neurosurgical Focus*, vol. 47, no. 1, E15, 2019 (cit. on pp. 18–21, 25, 28).

[68] K. Valen-Sendstad, A. W. Bergersen, Y. Shimogonya, L. Goubergrits, J. Bruening, *et al.*, "Real-world variability in the prediction of intracranial aneurysm wall shear stress: the 2015 International Aneurysm CFD Challenge," *Cardiovascular Engineering and Technology*, vol. 9, pp. 544–64, 2018 (cit. on pp. 18, 19, 25, 26, 32).

[69] P. Berg, S. Voß, S. Saalfeld, G. Janiga, A. W. Bergersen, *et al.*, "Multiple Aneurysms AnaTomy CHallenge 2018 (MATCH)–phase I: segmentation," *Cardiovascular Engineering and Technology*, vol. 9, pp. 565–81, 2018 (cit. on pp. 18, 19).

[70] S. Voß, O. Beuing, G. Janiga, and P. Berg, "Multiple Aneurysms AnaTomy CHallenge 2018 (MATCH)–phase Ib: effect of morphology on hemodynamics," *PLoS ONE*, vol. 14, no. 5, e0216813, 2019 (cit. on p. 18).

[71] P. Berg, S. Voß, G. Janiga, S. Saalfeld, A. W. Bergersen, *et al.*, "Multiple Aneurysms AnaTomy CHallenge 2018 (MATCH)–phase II: rupture risk assessment," *International Journal of Computer Assisted Radiology and Surgery*, vol. 14, pp. 1795–1804, 2019 (cit. on pp. 18, 20, 22, 30).

[72] L. Goubergrits, F. Hellmeier, J. Bruening, A. Spuler, H.-C. Hege, *et al.*, "Multiple Aneurysms AnaTomy CHallenge 2018 (MATCH): Uncertainty quantification of geometric rupture risk parameters," *Biomedical Engineering OnLine*, pp. 18–35, 2019 (cit. on pp. 18, 19).

[73] S. Hodis, S. Kargar, D. Kallmes, and D. Dragomir-Daescu, "Artery length sensitivity in patient-specific cerebral aneurysm simulations," *American Journal of Radiology*, vol. 36, pp. 737–43, 2015 (cit. on pp. 19, 26).

[74] V. Pereira, O. Brina, A. M. Gonzales, A. Narata, P. Bijlenga, *et al.*, "Evaluation of the influence of inlet boundary conditions on computational fluid dynamics for intracranial aneurysms: a virtual experiment," *Journal of Biomechanics*, vol. 46, pp. 1531–39, 2013 (cit. on p. 19).

[75] Y. Hua, J. H. Oh, and Y. B. Kim, "Influence of parent artery segmentation and boundary conditions on hemodynamic characteristics of intracranial aneurysms," *Yonsei Medical Journal*, vol. 56, no. 5, pp. 1328–37, 2015 (cit. on pp. 19, 22, 26).

[76] S. Hodis, S. Uthamaraj, A. L. Smith, K. D. Dennis, D. F. Kallmes, *et al.*, "Grid convergence errors in hemodynamic solution of patient-specific cerebral aneurysms," *Journal of Biomechanics*, vol. 45, pp. 2907–13, 2012 (cit. on pp. 20, 30).

[77] A. Aranda and A. Valencia, "Study on the relationship between wall shear stress and aspect ratio of cerebral aneurysms with different pressure differences using CFD simulations," *Journal of Mechanics in Medicine and Biology*, vol. 18, no. 5, pp. 1850055-1–16, 2018 (cit. on pp. 20, 30).

[78] A. Marzo, P. Singh, P. Reymond, N. Stergiopulos, U. Patel, *et al.*, "Influence of inlet boundary conditions on the local haemodynamics of intracranial aneurysms," *Computer Methods in Biomechanics and Biomedical Engineering*, vol. 12, no. 4, pp. 431–44, 2009 (cit. on pp. 20, 22, 26, 30).

[79] K. Valen-Sendstad and D. Steinman, "Mind the gap: impact of computational fluid dynamics solution strategy on prediction of intracranial aneurysm hemodynamics and rupture status indicators," *American Journal of Neuroradiology*, vol. 35, pp. 536–43, 2014 (cit. on p. 20).

[80] G. G. Ferguson, "Physical factors in the initiation, growth, and rupture of human intracranial saccular aneurysms," *Journal of Neurosurgery*, vol. 37, no. 6, pp. 666–77, 1972 (cit. on p. 20).

[81] J. Ortega, D. Maitland, T. Wilson, W. Tsai, Ǒ. Savaş, *et al.*, "Vascular dynamics of a shape memory polymer foam aneurysm treatment technique," *Annals of Biomedical Engineering*, vol. 35, no. 11, pp. 1870–84, 2007 (cit. on pp. 20, 36, 50).

[82] A. J. Geers, I. Larrabide, H. G. Morales, and A. F. Frangi, "Approximating hemodynamics of cerebral aneurysms with steady flow simulations," *Journal of Biomechanics*, vol. 47, pp. 178–85, 2014 (cit. on pp. 21, 28, 32).

[83] J. Xiang, M. Tremmel, J. Kolega, E. I. Levy, S. K. Natarajan, *et al.*, "Newtonian viscosity model could overestimate wall shear stress in intracranial aneurysm domes and underestimate rupture risk," *Journal of NeuroInterventional Surgery*, vol. 4, pp. 351–57, 2012 (cit. on p. 21).

[84] A. El Gibaly, O. A. El-Bassiouny, O. Diaa, A. I. Shehata, T. Hassan, *et al.*, "Effects of non-Newtonian viscosity on the hemodynamics of cerebral aneurysms," *Applied Mechanics and Materials*, vol. 819, pp. 366–70, 2016 (cit. on p. 21).

[85] H. G. Morales, I. Larrabide, A. J. Geers, M. L. Aguilar, and A. F. Frangi, "Newtonian and non-Newtonian blood flow in coiled cerebral aneurysms," *Journal of Biomechanics*, vol. 46, pp. 2158–64, 2013 (cit. on p. 21).

[86] M. O. Khan, D. A. Steinman, and K. Valen-Sendstad, "Non-Newtonian versus numerical rheology: practical impact of shear-thinning on the prediction of stable and unstable flows in intracranial aneurysms," *International Journal for Numerical Methods in Biomedical Engineering*, vol. 33, e2836, 2017 (cit. on p. 21).

[87] K. Valen-Sendstad, M. Piccinelli, R. Krishnankuttyrema, and D. A. Steinman, "Estimation of inlet flow rates for image-based aneurysm CFD models: where and how to begin?" *Annals of Biomedical Engineering*, vol. 43, no. 6, pp. 1422–31, 2015 (cit. on pp. 21, 28, 29).

[88] S. Saalfeld, S. Voß, O. Beuing, B. Preim, and P. Berg, "Flow-splitting-based computation of outlet boundary conditions for improved cerebrovascular simulation in multiple intracranial aneurysms," *International Journal of Computer Assisted Radiology and Surgery*, vol. 14, pp. 1805–13, 2019 (cit. on p. 22).

[89] C. Chnafa, P. Bouillot, O. Brina, M. Najafi, B. M. A. Delattre, *et al.*, "Errors in power-law estimations of inflow rates for intracranial aneurysm CFD," *Journal of Biomechanics*, vol. 80, pp. 159–65, 2018 (cit. on pp. 22, 35).

[90] J. Xiang, A. H. Siddiqui, and H. Meng, "The effect of inlet waveforms on computational hemodynamics of patient-specific intracranial aneurysms," *Journal of Biomechanics*, vol. 47, no. 16, pp. 3882–90, 2014 (cit. on p. 22).

[91] I. C. Campbell, J. Ries, S. S. Dhawan, A. A. Quyyumi, W. R. Taylor, *et al.*, "Effect of inlet velocity profiles on patient-specific computational fluid dynamics simulations of the carotid bifurcation," *Journal of Biomechanical Engineering*, vol. 134, no. 5, pp. 051001-1–8, 2012 (cit. on p. 22).

[92] J. Y. Moon, D. C. Suh, Y. S. Lee, Y. W. Kim, and J. S. Lee, "Considerations of blood properties, outlet boundary conditions and energy loss approaches in computational fluid dynamics modeling," *Neurointervention*, vol. 9, pp. 1–8, 2014 (cit. on p. 22).

[93] C. Chnafa, O. Brina, V. M. Pereira, and D. A. Steinman, "Better than nothing: a rational approach for minimizing the impact of outflow strategy on cerebrovascular simulations," *American Journal of Neuroradiology*, vol. 39, pp. 337–43, 2018 (cit. on pp. 22, 29).

[94] S. Ramalho, A. Moura, A. M. Gambaruto, and A. Sequeira, "Sensitivity to outflow boundary conditions and level of geometry description for a cerebral aneurysm," *International Journal for Numerical Methods in Biomedical Engineering*, vol. 28, pp. 697–713, 2012 (cit. on p. 22).

[95] M. Raschi, F. Mut, G. Byrne, C. M. Putnam, S. Tateshima, *et al.*, "CFD and PIV analysis of hemodynamics in a growing intracranial aneurysm," *International Journal for Numerical Methods in Biomedical Engineering*, vol. 28, pp. 214–28, 2012 (cit. on p. 23).

[96] N. H. Mokhtar, A. Abasa, R. M. N. A. Hamid, and S. L. Teong, "Effect of different stent configurations using Lattice Boltzmann method and particles image velocimetry on artery bifurcation aneurysm problem," *Journal of Theoretical Biology*, vol. 433, pp. 73–84, 2017 (cit. on p. 23).

[97] S. Tupin, K. M. Saqr, and M. Ohta, "Effects of wall compliance on multiharmonic pulsatile flow in idealized cerebral aneurysm models: comparative PIV experiments," *Experiments in Fluids*, vol. 61, no. 164, pp. 1–11, 2020 (cit. on p. 23).

[98] H. Ni, *Schematic diagram of PIV system*, `https://www.researchgate.net/figure/The-schematic-diagram-of-the-PIV-system_fig7_282400960`, 2015 (cit. on p. 23).

[99] K. Bai and J. Katz, "On the refractive index of sodium iodide solutions for index matching in PIV," *Experiments in Fluids*, vol. 55, 2014 (cit. on p. 23).

[100] A. V. Kamenskiy, Y. A. Dzenis, J. N. MacTaggart, A. S. Desyatova, and I. I. Pipinos, "In vivo three-dimensional blood velocity profile shapes in the human common, internal, and external carotid arteries," *Journal of Vascular Surgery*, vol. 54, pp. 1011–20, 2011 (cit. on p. 26).

[101] K. R. Moyle, L. Antiga, and D. A. Steinman, "Inlet conditions for image-based CFD models of the carotid bifurcation: is it reasonable to assume fully developed flow?" *Journal of Biomechanical Engineering*, vol. 128, pp. 371–79, 2006 (cit. on p. 26).

[102] P. Hasgall, F. Di Gennarro, C. Baumgartner, E. Neufeld, B. Lloyd, *et al.*, *IT'IS Database for thermal and electromagnetic parameters of biological tissues*, version 4, 2018 (cit. on pp. 28, 50).

[103] D. Li and A. M. Robertson, "A structural multi-mechanism constitutive equation for cerebral arterial tissue ," *International Journal of Solids and Structures*, vol. 46, pp. 2920–28, 2009 (cit. on p. 28).

[104] P. Tricerri, L. Dedè, S. Deparis, A. Quarteroni, A. M. Robertson, *et al.*, "Fluid-structure interaction simulations of cerebral arteries modeled by isotropic and anisotropic constitutive laws," *Computational Mechanics*, vol. 55, no. 3, pp. 479–98, 2015 (cit. on p. 28).

[105] M. N. Gwilliam, N. Hoggard, D. Capener, P. Singh, A. Marzo, *et al.*, "MR derived volumetric flow rate waveforms at locations within the common carotid, internal carotid, and basilar arteries," *Journal of Cerebral Blood Flow and Metabolism*, vol. 29, pp. 1975–82, 2009 (cit. on pp. 28, 32, 33, 50).

[106] L. Xu, F. Liang, B. Zhao, J. Wan, and H. Liu, "Influence of aging-induced flow waveform variation on hemodynamics in aneurysms present at the internal carotid artery: a computational model-based study," *Computers in Biology and Medicine*, vol. 101, pp. 51–60, 2018 (cit. on p. 28).

[107] J. Krejza, M. Arkuszewski, S. E. Kasner, J. Weigele, A. Ustymowicz, *et al.*, "Carotid artery diameter in men and women and the relation to body and neck size," *Stroke*, vol. 37, no. 4, pp. 1103–05, 2006 (cit. on p. 28).

[108] J. Mocco, J. Huston, K. M. Fargen, J. Torner, and R. D. Brown, Jr., "An angiographic atlas of intracranial arterial diameters associated with cerebral aneurysms," *Journal of NeuroInterventional Surgery*, vol. 6, pp. 533–35, 2014 (cit. on p. 29).

[109] T. Ingebrigtsen, M. K. Morgan, K. Faulder, L. Ingebrigtsen, T. Sparr, *et al.*, "Bifurcation geometry and the presence of cerebral artery aneurysms," *Journal of Neurosurgery*, vol. 101, no. 1, pp. 108–13, 2004 (cit. on p. 29).

[110] C. Chnafa, P. Bouillot, O. Brina, B. M. A. Delattre, M. I. Vargas, *et al.*, "Vessel calibre and flow splitting relationships at the internal carotid artery terminal bifurcation," *Physiological Measurement*, vol. 38, pp. 2044–57, 2017 (cit. on p. 29).

[111] M. I. Baharoglu, A. Lauric, C. Wu, J. Hippelheuser, and A. M. Malek, "Deviation from optimal vascular caliber control at middle cerebral artery bifurcations harboring aneurysms," *Journal of Biomechanics*, vol. 47, no. 13, pp. 3318–24, 2014 (cit. on p. 29).

[112] K. M. Saqr, S. Tupin, S. Rashad, T. Endo, K. Niizuma, *et al.*, "Physiologic blood fow is turbulent," *Scientific Reports*, vol. 10, p. 15 492, 2020 (cit. on p. 29).

[113] K. Valen-Sendstad, K.-A. Mardal, M. Mortensen, B. A. P. Reif, and H. P. Langtangen, "Direct numerical simulation of transitional flow in a patient-specific intracranial aneurysm," *Journal of Biomechanics*, vol. 44, no. 16, pp. 2826–32, 2011 (cit. on p. 29).

[114] F. R. Menter, "Two-equation eddy-viscosity turbulence models for engineering applications," *AIAA Journal*, vol. 32, no. 8, pp. 1598–1605, 1994 (cit. on p. 29).

[115] J. Banks and N. W. Bressloff, "Turbulence modeling in three-dimensional stenosed arterial bifurcations," *Journal of Biomechanical Engineering*, vol. 129, no. 1, pp. 40–50, 2007 (cit. on p. 29).

[116] N. Dazeo, J. Dottori, G. Boroni, A. P. Narata, and I. Larrabide, "Stenting as porous media in anatomically accurate geometries: a comparison of models and spatial heterogeneity," *Journal of Biomechanics*, vol. 110, p. 109 945, 2020 (cit. on p. 36).

[117] M. R. Levitt, M. C. Barbour, S. R. du Roscoat, C. Geindreau, V. K. Chivukula, *et al.*, "Computational fluid dynamics of cerebral aneurysm coiling using high-resolution and high-energy synchrotron X-ray microtomography: comparison with the homogeneous porous medium approach," *Journal of NeuroInterventional Surgery*, vol. 9, p. 00, 2017 (cit. on p. 36).

[118] J. M. Ortega, J. Hartman, J. N. Rodriguez, and D. J. Maitland, "Virtual treatment of basilar aneurysms using shape memory polymer foam," *Annals of Biomedical Engineering*, vol. 41, no. 4, pp. 725–43, 2013 (cit. on pp. 36–38, 40, 48).

[119] D. J. Maitland, W. Small IV, J. M. Ortega, P. R. Buckley, J. Rodriguez, *et al.*, "Prototype laser-activated shape memory polymer foam device for embolic treatment of aneurysms," *Journal of Biomedical Optics*, vol. 12, no. 3, pp. 030504-1–3, 2007 (cit. on p. 37).

[120] J. N. Rodriguez, M. W. Miller, A. Boyle, J. Horn, C.-K. Yang, *et al.*, "Reticulation of low density shape memory polymer foam with an in vivo demonstration of vascular occlusion," *Journal of the Mechanical Behavior of Biomedical Materials*, vol. 40, pp. 102–14, 2014 (cit. on p. 38).

[121] H. E. Hafsteinsson, "Porous media in OpenFOAM," Chalmers Tekniska Högskola AB, Göteborg, Sweden, Tech. Rep., 2009 (cit. on p. 38).

[122] R. Ouared, I. Larrabide, O. Brina, P. Bouillot, G. Erceg, *et al.*, "Computational fluid dynamics analysis of flow reduction induced by flow-diverting stents in intracranial aneurysms: a patient-unspecific hemodynamics change perspective," *Journal of NeuroInterventional Surgery*, vol. 8, pp. 1288–93, 2016 (cit. on p. 47).

[123] O. Brina, P. Bouillot, P. Reymond, A. Luthman, C. Santarosa, *et al.*, "How flow reduction influences the intracranial aneurysm occlusion: a prospective 4D phase-contrast MRI study," *American Journal of Neuroradiology*, vol. 40, pp. 2117–23, 2019 (cit. on p. 47).

[124] F. Mut, M. Raschi, E. Scrivano, C. Bleise, J. Chudyk, *et al.*, "Association between hemodynamic conditions and occlusion times after flow diversion in cerebral aneurysms," *Journal of NeuroInterventional Surgery*, vol. 7, pp. 286–90, 2015 (cit. on p. 47).

[125] M. K. Kole, D. M. Pelz, P. Kalapos, D. H. Lee, I. B. Gulka, *et al.*, "Endovascular coil embolization of intracranial aneurysms: important factors related to rates and outcomes of incomplete occlusion," *Journal of Neurosurgery*, vol. 102, no. 4, pp. 607–15, 2005 (cit. on p. 47).

[126] C. J. Griessenauer, N. Adeeb, P. M. Foreman, R. Gupta, A. S. Patel, *et al.*, "Impact of coil packing density and coiling technique on occlusion rates for aneurysms treated with stent-assisted coil embolization," *World Neurosurgery*, vol. 94, pp. 157–66, 2016 (cit. on p. 47).

[127] S. Ishihara, M. E. Mawad, K. Ogata, C. Suzuki, N. Tsuzuki, *et al.*, "Histopathologic findings in human cerebral aneurysms embolized with platinum coils: report of two cases and review of the literature," *American Journal of Neuroradiology*, vol. 23, pp. 970–74, 2002 (cit. on p. 47).

[128] J. D. Horn, D. J. Maitland, J. Hartman, and J. M. Ortega, "Computational study of clot formation in aneurysms treated with shape memory polymer foam," *Medical Engineering and Physics*, vol. 75, pp. 65–71, 2019 (cit. on pp. 48, 59).

[129] L. Goubergrits, J. Schaller, U. Kertzscher, T. Woelken, M. Ringelstein, *et al.*, "Hemodynamic impact of cerebral aneurysm endovascular treatment devices: coils and flow diverters," *Expert Review of Medical Devices*, vol. 11, no. 4, pp. 361–73, 2014 (cit. on p. 48).

[130] H. Wang, B. Wang, K. Normoyle, K. Jackson, K. Spitler, *et al.*, "Brain temperature and its fundamental properties: a review for clinical neuroscientists," *Frontiers in Neuroscience*, vol. 8, p. 307, 2014 (cit. on p. 49).

[131] N. Matsumi, K. Matsumoto, N. Mishima, E. Moriyama, T. Furuta, *et al.*, "Thermal damage threshold of brain tissue—histological study of heated normal monkey brains," *Neurologia medico-chirurgica*, vol. 34, no. 4, pp. 209–15, 1994 (cit. on pp. 49, 56).

[132] S. A. Pineda-Castillo, J. Luo, H. Lee, B. N. Bohnstedt, Y. Liu, *et al.*, "Effects of carbon nanotube infiltration on a shape memory polymer-based device for brain aneurysm therapeutics: design and characterization of a Joule-heating triggering mechanism," *Advanced Engineering Materials*, vol. 23, no. 6, p. 2 100 322, 2021 (cit. on pp. 49, 55, 56).

[133] S. A. Sapareto and W. C. Dewey, "Thermal dose determination in cancer therapy," *International Journal of Radiation Oncology*Biology*Physics*, vol. 10, no. 6, pp. 787–800, 1984 (cit. on p. 55).

[134] G. C. van Rhoon, T. Samaras, P. S. Yarmolenko, M. W. Dewhirst, and E. N. amd Niels Kuster, "CEM43°C thermal dose thresholds: a potential guide for magnetic resonance radiofrequency exposure levels?," vol. 23, pp. 2215–27, 2013 (cit. on p. 56).

[135] P. S. Yarmolenko, E. J. Moon, C. Landon, A. Manzoor, D. W. Hochman, *et al.*, "Thresholds for thermal damage to normal tissues: an update," *International Journal of Hyperthermia*, vol. 27, no. 4, pp. 320–43, 2011 (cit. on p. 56).

[136] T. Lu, Z. Chen, H. J. Qi, and T. J. Wang, "A micro-structure based constitutive model for anisotropic stress-strain behaviors of artery tissues," *International Journal of Solids and Structures*, vol. 139–140, pp. 55–64, 2011 (cit. on p. 59).

[137] P. H. Geoghegan, N. A. Buchmann, J. Soria, and M. C. Jermy, "Time-resolved PIV measurements of the flow field in a stenosed, compliant arterial model," *Experiments in Fluids*, vol. 54, 2013 (cit. on p. 59).

[138] *Thermo Scientific Amira software 6 user's guide*, Thermo Fisher Scientific, 2018 (cit. on p. 60).

[139] Autodesk, *MM manual*, `http://help.autodesk.com/view/MSHMXR/2019/ENU/` (cit. on p. 60).

[140] ESI Group, *OpenFOAM user guide*, `https://www.openfoam.com/documentation/user-guide/` (cit. on pp. 60, 72).

[141] Kitware Inc, *ParaView user's guide*, `https://docs.paraview.org/en/latest/UsersGuide/index.html` (cit. on p. 60).

[142] The MathWorks Inc, *Documentation*, `https://www.mathworks.com/help/matlab/` (cit. on p. 60).

[143] A. M. Gambaruto, J. Janela, A. Moura, and A. Sequeira, "Sensitivity of hemodynamics in a patient specific cerebral aneurysm to vascular geometry and blood rheology," *Mathematical Biosciences and Engineering*, vol. 8, no. 2, pp. 409–23, 2011 (cit. on p. 63).